A Study on the Effect of Grain Boundary Elements on Polycrystalline Superalloys

Paraskevas Kontis



Department of Materials

University of Oxford

A Study on the Effect of Grain Boundary Elements on Polycrystalline Superalloys

by

Paraskevas Kontis

A thesis submitted to

The University of Oxford

for the degree of

Doctor of Philosophy

Department of Materials

St Anne's College

The University of Oxford

Hilary Term 2016

Abstract

Polycrystalline nickel-based superalloys substantially derive their mechanical properties from the strength of their grain boundaries. Carbon and boron are the main grain boundary strengthening elements and they play a critical role on the performance of superalloys. However, how these grain boundary elements enhance the mechanical properties of polycrystalline superalloys is not well understood. This thesis presents information about the impact of carbon and boron additions on the mechanical properties of two superalloys suitable for land-based gas turbine applications. New findings with high scientific and industrial relevance that will improve our understanding about the grain boundary elements during the design of new superalloys are presented. High-resolution characterisation methods were used to study the effect of boron on the grain boundary character of a new polycrystalline superalloy. Boron was found to alter substantially the grain boundary character by controlling phase precipitation. Different boron contents were also studied and correlated with the mechanical properties; creep performance was found to vary with boron content. In addition, *in-situ* studies at elevated temperatures were used to rationalise the effect of boron on improving the mechanical properties of superalloys. The main deformation mechanisms taking place were identified and presented. Finally, the effect of carbides on crack initiation and propagation under complex stress and temperature cycles was studied in detail for a conventional cast superalloy. Carbides were found to have a detrimental effect by serving as crack initiation sites on superalloys for power generation applications. In overall, the findings suggest that boron rather than carbon is the crucial grain boundary strengthener for superalloys used in industrial gas turbines.

Dedicated to my parents,

Theodoros and Katerina

Preface

The work reported in this thesis was carried out by the author in the Department of Materials, University of Oxford, under the supervision of Professor Roger C. Reed. No part of this thesis has been previously submitted for a degree at this or any other university. Parts of this thesis have appeared in the following publications:

Publications with peer review process:

- **P. Kontis**, H.A.M. Yusof, S. Pedrazzini, M. Danaie, K.L. Moore, P.A.J. Bagot, M.P. Moody, C.R.M. Grovenor and R.C. Reed, On the Effect of Boron on Grain Boundary Character in a New Polycrystalline Superalloy, *Acta Materialia* 103 (2016) 688-699.
- **P. Kontis**, E. Alabort, D. Barba, D.M. Collins, A.J. Wilkinson and R.C. Reed, On the Role of Boron on Improving Ductility in a New Polycrystalline Superalloy, *Acta Materialia* 124 (2017) 489-500.
- **P. Kontis**, S. Pedrazzini, Y. Gong, P.A.J. Bagot, M.P. Moody and R.C. Reed, The Effect of Boron on Oxide Scale Formation in a New Polycrystalline Superalloy, *Scripta Materialia* 127 (2017) 156-159.

Conference proceedings:

- **P. Kontis**, D.M. Collins, S. Johansson, A.J. Wilkinson, J.J. Moverare and R.C. Reed, Crack Initiation and Propagation during Thermal–Mechanical Fatigue of IN792: Effects of Dwell Time, *Superalloys 2016: Proceedings of the 13th Intenational Symposium of Superalloys*, 763-772.
- **P. Kontis**, H.A.M. Yusof, K.L. Moore, C.R.M. Grovenor and R.C. Reed, On the Effect of Boron on the Mechanical Properties of a New Polycrystalline Superalloy, *2nd European Symposium on Superalloys and their Applications*, 12 -16 May 2014, Giens, France.
- J.J. Moverare, **P. Kontis**, S. Johansson and R.C. Reed, Thermomechanical Fatigue Crack Growth in a Cast Polycrystalline Superalloy, *2nd European Symposium on Superalloys and their Applications*, 12 - 16 May 2014, Giens, France.

Acknowledgements

I would like to express my special appreciation and thanks to my supervisor *Professor Roger C. Reed*, you have been a tremendous mentor for me. I would like to thank you for encouraging my research and for being restless in motivating me to achieve always the best possible results.

I am also grateful to Siemens Industrial Turbomachinery AB in Sweden for sponsoring this work. The invaluable advice and support of Fredrik Karlsson, Helena Oskarsson, Leif Berglin, Magnus Hasselqvist, David Gustaffson, and Frans Palmert is acknowledged. Thank you for your incredible hospitality during our project meetings in Finspäng. I extend my sincere gratitude to Professor Johan Moverare from the University of Linköping in Sweden (previously in Siemens Industrial Turbomachinery AB) for performing TMF tests and providing invaluable knowledge in the area of mechanical testing of superalloys. I would like also to thank Geoff Marchant for conducting creep tests in Siemens, Lincoln (UK).

I am immensely grateful to the atom probe group, particularly to Dr Paul Bagot and Professor Michael Moody for allowing me access to the atom probe facility in Oxford and advising with data interpretation. Dr Mohsen Danaie from the atom probe group is also thanked for his help with the TEM analysis. Further I would like to give special thanks to Dr David Collins and Professor Angus Wilkinson for performing the EBSD strain mapping analysis. Hanis Yusof, Dr Katie Moore and Professor Chris Grovenor are thanked for conducting NanoSIMS analysis. I would like also to thank Dr Neil Young, Gabriella Chapman and Dr Gareth Hughes for their help with my electron microscopy queries.

I would like to give special thanks to my officemates Dr Enrique Alabort, Dr David Crudden, Daniel Barba, Yilun Gong, Dr Fauzan Adziman and many others within Professor Reed's research group. Your support and help has been of great

importance to me. I am greatly indebted to Dr Stella Pedrazzini for proofreading this thesis, waking up very early on a few Sunday mornings to help me with the APT tests and immensely supporting me in everything I have done.

Finally, I would like to give huge thanks to my parents, Katerina Papagiani and Theodoros Kontis, and my sister, Maria Konti. Their love and encouragement meant the world to me.

Abbreviations

IGT	Industrial Gas Turbine
TCP	Topologically Closed-Packed
VIM	Vacuum Induction Melting
CC	Conventional Casting
DS	Directional Solidified
SC	Single Crystal
HIP	Hot Isostatic Pressing
ICP-OES	Inductively Coupled Plasma- Optical Emission Spectometry
TMF	Thermal-Mechanical Fatigue
SEM	Scanning Electron Microscopy
EDX	Energy Dispersive X-Ray
FIB	Focused Ion Beam
EBSD	Electron Backscattered Diffraction
TEM	Transmission Electron Microscopy
SIMS	Secondary Ion Mass Spectrometry
APT	Atom Probe Tomography
LCF	Low Cycle Fatigue
ETMT	Electro-Thermal Mechanical Testing
LVDT	Linear Variable Differential Transducer
IP-TMF	In-Phase Thermal-Mechanical Fatigue
OP-TMF	Out-of-Phase Thermal-Mechanical Fatigue

List of Figures

1.1 Gas entry temperatures for turbines, showing the delay of 15 years between aero and industrial gas turbine technologies. Dashed lines are showing the predictions of the turbine entry temperature [2, 5]. . . 3

1.2 Basic features of the SGT-750 industrial gas turbine. (Courtesy of Siemens). 4

2.1 Elements important in the constitution of nickel-based superalloys and their position in the periodic table [6]. 9

2.2 Arrangements of Ni and Al atoms in the ordered Ni_3Al phase [4]. . . 11

2.3 Schematic diagram illustrating the development, from (a) to (f), of strain-induced, facetted γ' morphologies during heat treatment: left, projection along $\langle 111 \rangle$ and right, projection along $\langle 001 \rangle$ [13]. 12

2.4 Schematic illustrations of the MC-type carbide morphology at different carbide growth rates. The carbide growth rate increases gradually from A to J [23]. 15

2.5 Backscattered electron images of degenerated MC carbides under the different exposure conditions: a) 800 °C/1000 h, b) 850 °C/5000 h and c) 900 °C/10000 h [33]. 18

2.6 The (001) plane of FCC structure: a) interstitial-free and b) with carbon atoms in the interstitial sites [38]. 20

2.7 Agglomeration of γ' and $M_{23}C_6$ particles and crack initiation at grain boundaries: a) initial microstructure, b) agglomeration of γ' and $M_{23}C_6$ along the grain boundaries, c) formation of γ' denuded zones and d) crack initiation at γ' denuded zones at grain boundaries transverse to load axis [7]. 22

2.8 Schematic illustration of a double-chamber vacuum induction melting furnace [51]. 26

2.9 Schematic illustrations of the various steps of investment casting process [52]. 27

2.10 Assembled wax pattern for the casting of a single tapered rod bar: a) before any slurry is applied b) after cobalt aluminate and stucco are applied. Note the characteristic blue colour caused by the cobalt aluminate. 28

2.11 The macrostructure of the superalloy René 77 from the cross section of castings in ceramic moulds with: a) no cobalt aluminate and b) modified with 5 % mass of $CoAl_2O_4$ [53]. 29

2.12 Level of microporosity before and after HIP from samples of various grain sizes of MAR-247 [57]. 30

2.13 Creep fracture modes: a) a wedge crack formed at the triple junctions and b) a wedge crack as an accumulation of spherical cavities [62]. . . 32

2.14 Cavitation (r-type) or voids at a transverse grain boundary [62]. . . . 32

2.15 Schematic illustrations of various cavity nucleation mechanisms: a) sliding leading to cavitation from ledges and triple points, b) cavity nucleation from vacancy condensation at high-stress region, c) cavity formation at the head of a dislocation pile-up and d) the formation of a cavity from a particle-obstacle in conjunction with the previous mechanisms [62]. 34

2.16 Cavity growth from diffusion across the cavity surface and through the grain boundaries [62]. 36

2.17 Schematic illustration of the model for coupled diffusive cavity growth with creep plasticity [85]. 38

3.1 Geometry of the moulds used to cast STAL15-CC. 41

3.2 Secondary SEM images showing the stages of the lift-out process and APT sample preparation: a) W protective layer is deposited on area of interest, b) side trenches milled at an angle 30 ° from normal to the surface, c) transfer of bar to supportive Si flat posts, d) welding of bar Si flat post and cut of slice from the bar, e) first annular milling and f) second annular milling. 47

4.1 Backscattered SEM images of fully heat microstructures of: a) boron-free, b) low boron, c) medium boron and d) high boron alloys alongside corresponding descriptive schematic illustrations. 54

4.2 TEM micrograph of fully heat treated microstructure from a grain boundary region of high boron alloy showing an intergranular MC carbide. 55

4.3 TEM micrograph of fully heat treated microstructure from a grain boundary region of the medium boron alloy. Representative M_5B_3 borides along the grain boundary and grain boundary γ' are illustrated. The grain boundary direction is denoted by the red arrow. . . 56

4.4 TEM micrograph of fully heat treated microstructure of the high boron alloy. Representative $M_{23}C_6$ carbides and tertiary γ' in the γ matrix are illustrated. 57

4.5 Selected grain boundary regions of fully heat treated microstructures of: a) boron free, b) low boron, c) medium boron and d) high boron alloys for atom probe tomography. 58

4.6 SEM micrograph of atom probe tip obtained from fully heat treated grain boundary of the boron free alloy alongside atom probe reconstruction. 60

4.7 SEM micrograph of atom probe tip obtained from fully heat treated grain boundary of the high boron alloy alongside atom probe reconstruction. 61

4.8 SEM micrographs of atom probe tips obtained from fully heat treated grain boundaries of: a) low boron and b) medium boron alloys alongside atom probe reconstructions. 63

4.9 Concentration profiles analysis across grain boundary interfaces collected from atom probe tomography: a) concentration of C, Cr and Co at $\gamma/M_{23}C_6$ interface from the boron free alloy (data in Figure 4.6), b) and c) concentration of B, C, Al, Ta and Cr at MC/γ' and MC/γ interface from the high boron alloy (data in Figure 4.7), d) concentration of B, C, Al and Co at γ'/M_5B_3 interface from the low boron alloy (data in Figure 4.8(a)), e) concentration of B, C, Al and Co at γ'/M_5B_3 interface from the medium boron alloy (data in Figure 4.8(b)) and f) concentration of B, C, Cr and Co at γ/M_5B_3 interface from the medium boron alloy (data in Figure 4.8(b)). Error less than 0.05 at.%. 64

4.10 NanoSIMS images showing partitioning of C and B at intra- and intergranular carbides and intergranular borides in fully heat treated microstructures of: a) low boron b) medium boron and c) high boron alloys. Red boxes indicate the location of subsequent SEM imaging and red lines indicate the position and direction of the line scans. . . 66

4.11 Line-scans across the grain boundaries as labelled in the NanoSIMS maps (see Figure 4.10), confirming the precipitation of Cr-rich borides. 67

4.12 Backscattered SEM images from areas investigated by NanoSIMS. Images correspond to the red boxes in Figure 4.10. 68

4.13 Concentration profiles analysis across the $\gamma/M_{23}C_6$ interface from the boron-free alloy collected by atom probe tomography (see Figure 4.6). Dashed ellipses indicate the carbon and boron enrichment. Error less than 0.05 at.%. 70

4.14 Calculated thickness of borides as function of average grain size and boron content. 71

4.15 A summary of superalloys plotted in a boron *vs.* chromium graph indicating for each alloy whether the boron is in the form of solid solution (denoted by solid-filled squares) or solid solution and borides (denoted by empty squares). 72

4.16 Creep strain *vs.* time curve for the investigated alloys. 74

4.17 Fracture surfaces of creep specimens tested at 750 °C/455 MPa: a) intergranular failure of boron free alloy and b) mixed inter- and transgranular failure of medium boron alloy. 75

4.18 Backscattered SEM images of the creep specimens tested at 750 °C/455 MPa showing secondary cracks in: a) boron free and b) medium boron alloys. Dark areas at the grain boundaries indicated by arrows correspond to cracks in the medium boron alloy; the rest dark areas correspond to intergranular borides. Stress axis along perpendicular axis. 76

4.19 DICTRA calculations of boron and carbon tracer diffusivity in γ phase, based on the mobility database MOBNI3. 78

5.1 Detailed experimental set-up for performing tensile tests using the ETMT device in this study. 85

5.2 Detailed experimental set-up used for the *in-situ* tensile tests in this study. 87

5.3 Grain boundary region from the boron-free alloy: a) backscattered SEM image after full heat treatment and b) HR-EBSD strain maps alongside inverse pole figure (IPF) map of the investigated area as denoted by the red box. The red line corresponds to line-scans shown in Figure 5.11. The X's indicate the reference points for the strain map analysis. 90

5.4 Grain boundary region from the boron-containing alloy: a) backscattered SEM image after full heat treatment and b) HR-EBSD strain maps alongside inverse pole figure (IPF) map of the investigated area as denoted by the red box. The red line corresponds to line-scans shown in Figure 5.11. The X's indicate the reference points for the strain map analysis. 91

5.5 Engineering strain *vs.* engineering stress curves at 750 °C and strain rates 2x10^{-3} s^{-1} and 2x10^{-5} s^{-1} for both boron-free and boron-containing alloys collected using the ETMT device. 93

5.6 Fracture surfaces of ETMT specimens from: a) boron-free and b) boron-containing alloys tested at 750 °C and strain rate 2x10^{-5} s^{-1}. Topography measurements performed using an Alicona microscope. . 95

5.7 Grain boundary region from the boron-free alloy: a) backscattered SEM image after $\sim$0.5 % deformation at 750 °C and strain rate 2x10^{-5} s^{-1} and b) HR-EBSD strain maps and GND density map of the investigated area as denoted by the red box after deformation with the scale bar in $\log_{10}$ scale of dislocation lines m^{-2}. Note the load direction is along the x axis. The white arrows indicate voids. 97

5.8 Grain boundary region from the boron-containing alloy: a) backscattered SEM image after $\sim$0.5 % deformation at 750 °C and strain rate 2x10^{-5} s^{-1} and b) HR-EBSD strain maps and GND density map of the investigated area as denoted by the red box after deformation with the scale bar in $\log_{10}$ scale of dislocation lines m^{-2}. Note the load direction is along the x axis. The white arrows indicate voids. . . 98

5.9 Sequential SEM images of a fully heat treated grain boundary region of the boron-free alloy tested in tension to failure: a) prior to deformation, b) after yield point, c) $\sim 3\,\%$ strain and d) after failure. Tensile axis in perpendicular direction. 100

5.10 Sequential SEM images of a fully heat treated grain boundary region of the boron-containing alloy tested in tension to failure: a) prior to deformation, b) after yield point, c) $\sim 3\,\%$ strain strain and d) after failure. Tensile axis in perpendicular direction. 101

5.11 Lattice strain line-scans across the grains as denoted by the red lines in Figures 5.3(b) and 5.4(b) for the boron-free and boron-containing, respectively. 104

5.12 SEM image of FIB-section of a serrated grain boundary tested at 750 °C and strain rate 2x10^{-5} s^{-1}. The arrows indicate voids at interfaces perpendicular to tensile axis. Continuous crack path is not observed. 106

5.13 Secondary SEM images showing: a) surface eruptions due to the oxidation of Ta-rich MC carbides as indicated by the arrows and b) FIB-section of oxidised MC carbide from the boron-containing alloy exposed at 750 °C for 50 hours, showing pores related with the oxidised MC carbide. 109

5.14 SEM figures of FIB-sections from grain boundary regions of: a) boron-free and b) boron-containing alloys exposed at 750 °C for 50 hours, alongside corresponding descriptive schematic illustrations. 110

6.1 Schematic graphs of stress *vs.* strain during: a) In-Phase (IP) TMF and b) Out-of-Phase (OP) TMF [156]. 116

6.2 Geometry of single edge notched (SEN) type specimen. 117

6.3 Crack length *vs.* number of cycles measurements for all the investigated TMF conditions for the IN792 alloy. 119

6.4 Crack growth rate *vs.* crack length graph for all the investigated TMF conditions. 120

6.5 Crack growth rate as a function of the maximum stress intensity factor for all the investigated TMF conditions. 121

6.6 Minimum and maximum force *vs.* crack length graph for all the investigated TMF conditions. 122

6.7 Backscattered SEM images of the crack initiation sites of: a) IP–5 minutes dwell, b) OP–5 minutes dwell, c) IP–360 minutes dwell and d) OP–360 minutes dwell specimens. Load axis is in horizontal direction. Red box denotes the area scanned for EDX mapping (see Figure 6.10). Arrows indicate voids around MC carbides. 124

6.8 Backscattered SEM image of cracked MC carbide at the vicinity of main crack tip of IP-test with 6 hours dwell and corresponding geometrically necessary dislocations (GND) density map with the scale bar in $\log_{10}$ scale of dislocation lines m^{-2}. Load axis in the horizontal direction. The arrow indicates void at MC carbide ahead of the crack tip. 126

6.9 Backscattered SEM image of cracked MC carbide from the IP-test with 5 minutes dwell, with corresponding lattice rotation maps (rotations in radians) and geometrically necessary dislocations (GND) density map with the scale bar in $\log_{10}$ scale of dislocation lines m^{-2}. The in-plane rotation ω_{12} and the out-of-plane rotations ω_{13} and ω_{23}, rotating about the 2 and 1 axis respectively are shown. 128

6.10 EDX chemical mapping of the crack initiation area as denoted by the red box in Figure 6.7(d). The crack propagates in the perpendicular direction and the red arrow indicates the oxidised (Ta,Ti)C carbide and the white dashed line shows the position of the carbide at the C map. 129

6.11 Backscattered SEM images showing the crack tips in: a) IP–5 minutes dwell, b) OP–5 minutes dwell, c) IP–360 minutes dwell and d) OP–360 minutes dwell specimens alongside corresponding EBSD inverse pole figures. Red boxes denote the scanned by EBSD areas and load axis is in horizontal direction. 131

6.12 Backscattered SEM image of fully heat treated IN792 showing intergranular MC carbides and corresponding EBSD strain maps. The strain ϵ_{11} along the horizontal axis x, the in-plane shear strain ϵ_{12} and the strain ϵ_{22} along the vertical axis y are shown. 133

6.13 a) Backscattered SEM image of the secondary crack tip of the IP–360 minutes dwell time specimen and b) EDX analysis of the intergranular oxidised MC carbide. The red box denotes the analysed by EDX area. 137

6.14 Crack tip from the OP with 360 minutes dwell time specimen, alongside corresponding inverse pole map (as denoted by the red box) showing the recrystallisation enhanced by oxidation. 139

7.1 Medium boron STAL15-CC alloy exposed isothermally at 900 °C for 9000 hours: a) backscattered SEM micrograph of the oxide scale and b) corresponding schematic representation of the oxide scale. The red boxes denote the areas of point EDX analysis (see data in Figure 7.2) 147

7.2 a) Point EDX analysis corresponding to the oxide areas denoted by the red boxes in Figure 7.1 and b) detail of the part of the EDX spectrum as denoted by the red dashed box. 148

7.3 Atom probe reconstruction from the boron-rich oxide of the medium boron STAL15-CC alloy exposed isothermally at 900 °C for 9000 hours. Grain boundaries are shown in Si. 149

List of Tables

1.1 Applications of superalloys in the US in 1980 [3]. 2

2.1 Summary of chemical compositions of various nickel-based superalloys (at.%) [4]. 9

2.2 The effect of alloying elements on microporosity in nickel-based superalloys [35]. 19

3.1 Summary of chemical compositions of the different STAL15-CC variants investigated (at.%). 40

4.1 Summary of published studies of boron-containing superalloys, in which boron is claimed to be present either (i) in elemental form at grain boundaries, or (ii) as a boride. 52

4.2 Chemical composition of carbides and borides as measured by atom probe tomography (at.%). 59

5.1 Summary of serrated grain boundaries and corresponding misorientation, serration amplitude and wavelength measurements for the boron-containing alloy. 103

6.1 IP and OP-TMF tests conducted in this study for the investigation of the effect of dwell-time during TMF. 118
6.2 Summary of crack initiation sites for all the investigated conditions. . 123
6.3 Cycles to crack initiation for all the investigated conditions. 130
6.4 Summary of crack propagation mode and parameters controlling crack propagation for all the investigated conditions. 135

7.1 Summary of suggested exposure temperatures and times for the microstructural evolution investigations for the three boron variants of STAL15-CC. 146
7.2 Proposed testing conditions for the evaluation of the effect of boron on creep performance of STAL15-CC. 150

Contents

Abstract **iii**

Acknowledgements **vi**

Abbreviations **viii**

List of Figures **ix**

List of Tables **ix**

Table of Contents **x**

1 Introduction **1**

1.1 Superalloys for Industrial Gas Turbines 1

1.2 Aim of Research 4

1.3 Structure of Thesis 6

2 Literature Review **8**

2.1 Nickel-Based Superalloys 8

2.1.1 Physical Metallurgy of Superalloys 8

2.2 Grain Boundary Strengtheners 13
2.2.1 Carbon 13
2.2.2 Boron 20
2.3 Processing of Superalloys 25
2.3.1 Investment Casting 25
2.3.2 The Effect of Cobalt Aluminate on Grain Size 28
2.3.3 Hot Isostatic Pressing (HIP) - Microporosity 30
2.4 Grain Boundary Fracture 31
2.4.1 Cavity Nucleation 33
2.4.2 Cavity Growth 36

3 Microstructural Characterisation Procedures 39
3.1 Introduction 39
3.2 Materials 39
3.3 Characterisation Methods 42
3.3.1 Scanning Electron Microscopy (SEM) – Energy Dispersive X-Ray (EDX) 42
3.3.2 Electron Backscattered Diffraction (EBSD) 43
3.3.3 Transmission Electron Microscopy (TEM) 44
3.3.4 Secondary Ion Mass Spectrometry (NanoSIMS) 44
3.3.5 Atom Probe Tomography (APT) 45

4 The Effect of Boron on Grain Boundary Character in a New Polycrystalline Superalloy 48
4.1 Introduction 48
4.2 Background 49
4.3 Experimental Procedures 53

4.4 Results . . . 53
4.4.1 Observations on Grain Boundary Morphology by Electron Microscopy . . . 53
4.4.2 Analysis by Atom Probe Tomography . . . 58
4.4.3 NanoSIMS Analysis . . . 65
4.5 Discussion . . . 69
4.5.1 Grain Boundary Character . . . 69
4.5.2 On the Importance of Grain Boundary Character on Creep Response . . . 73
4.5.3 Grain Boundary Chemistry . . . 77
4.6 Summary and Conclusions . . . 79

5 The Role of Boron on Improving Ductility in a New Polycrystalline Superalloy 81

5.1 Introduction . . . 81
5.2 Background . . . 82
5.3 Experimental Procedures . . . 84
5.3.1 High-Temperature Tensile Tests . . . 85
5.3.2 High-Resolution EBSD Strain Mapping . . . 88
5.4 Results . . . 89
5.4.1 Grain Boundary Serration . . . 89
5.4.2 Tensile Performance at 750 °C . . . 93
5.4.3 *In-situ* Observations . . . 95
5.5 Discussion . . . 102
5.5.1 The Ductilising Effect of Boron . . . 102
5.5.2 Crack Initiation and Propagation . . . 105
5.5.3 The Importance of Boron as Grain Boundary Element . . . 107

5.6 Summary and Conclusions 111

6 The Effect of MC Carbides on Thermal–Mechanical Fatigue of a Polycrystalline Superalloy 113

6.1 Introduction 113

6.2 Background 114

6.3 Experimental Procedures 117

6.4 Results 119

6.4.1 Crack Growth Rates 119

6.4.2 Crack Initiation 123

6.4.3 Crack Propagation 130

6.5 Discussion 132

6.5.1 MC Carbides – Crack Initiation Sites 132

6.5.2 The Effect of Dwell Time on Crack Propagation 135

6.6 Summary and Conclusions 140

7 Conclusions and Future Work 141

7.1 Conclusions 141

7.2 Future Work 145

7.2.1 Microstructural Stability of STAL15-CC 145

7.2.2 High-Temperature Mechanical Testing 150

7.2.3 The Effect of Carbon on Grain Boundaries 152

Bibliography 154

Chapter 1

Introduction

1.1 Superalloys for Industrial Gas Turbines

In the second and third decades of the 20th century different types of steel were utilized effectively as high temperature materials in gas turbines. However, the imperative need for gas turbines to operate at higher temperatures and reduce CO_2 emissions led to the design and development of a new group of materials for high performance applications at high temperatures: the nickel-based superalloys [1, 2].

Nickel-based superalloys were historically developed for aeroengines, where resistance to creep and fatigue was needed. A survey in 1980 in the US shown that 73 % of superalloys were used for aerospace applications, whereas only 10 % of superalloys were utilised in power generation applications as shown in Table 1.1 [3]. As a consequence a delay in passing the knowledge and technology behind superalloys from the jet engines to superalloys for industrial gas turbines (IGTs) for power

generation occured [1].

Table 1.1: Applications of superalloys in the US in 1980 [3].

Application	**Percent of total use, %**
Aerospace–gas turbines	73
Aerospace–airframes	8
Power generation–gas turbines	10
Power generation–nuclear	2
Power generation–fossil	1
Chemical processing industries	6
Miscellaneous (transportation, marine, etc.)	1

The development of superalloys has been mainly driven by the need of higher operating temperatures. In Figure 1.1 the demands in gas entry temperatures for IGTs and aero gas turbines between 1940 and 1980 is shown. It is apparent that the interest in developing advanced superalloys for IGTs happened at least 15 years later compared to that of aero gas turbines [2].

In addition, the environmental properties of nickel-based superalloys used in aeroengines are not adequate for IGTs applications. This is mainly due to the differences in operating times and fuels usage. For instance, higher quality of fossil fuel is used for jet engines, but fuels with $<$10000 ppmw sulphur are used in IGTs [4]. Thus, designing superalloys suitable to meet the requirements for power generation applications is necessary.

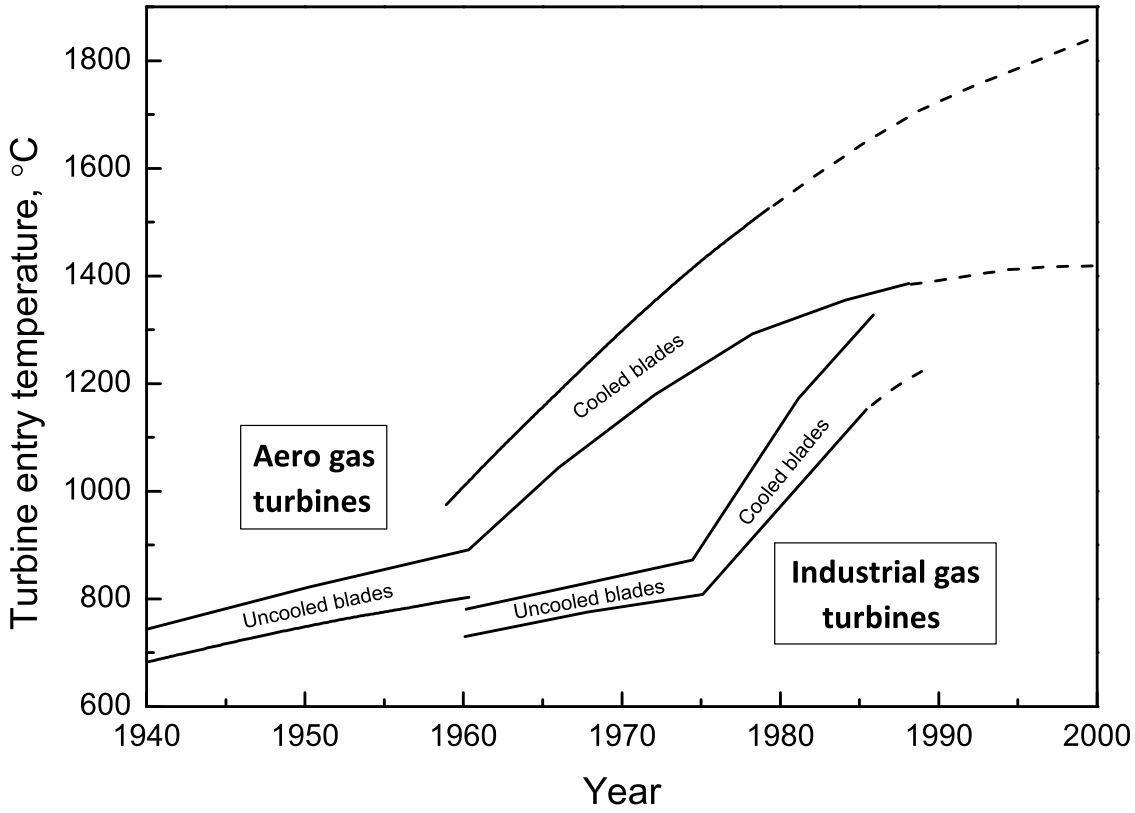


Figure 1.1: Gas entry temperatures for turbines, showing the delay of 15 years between aero and industrial gas turbine technologies. Dashed lines are showing the predictions of the turbine entry temperature [2, 5].

Figure 1.2 illustrates the main parts of a land-based gas turbine; the compressor, the shaft, the combustor and the engine can be seen. More specifically, the role of the compressor is to increase the pressure of the incoming air, through a system of blades and discs. The compressed air then is mixed with fuels and ignited in the combustion chamber. High-temperature gases are produced and expand through a turbine, which drives the compressor by a connected shaft. In general, the higher the operating temperatures the higher the efficiency of a gas turbine and the lower the CO_2 emission levels.

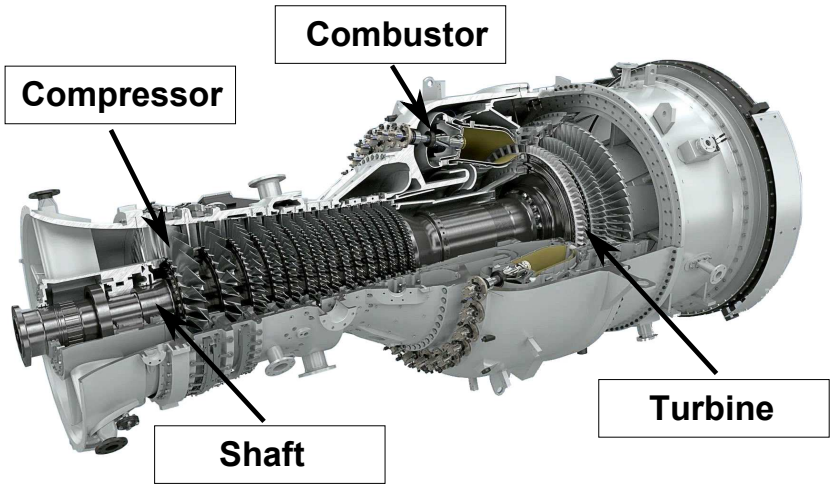


Figure 1.2: Basic features of the SGT-750 industrial gas turbine. (Courtesy of Siemens).

1.2 Aim of Research

Nickel-based superalloys have a pivotal role on the performance of industrial gas turbines. Over the last decades, the chemistry, the microstructure and the processing of superalloys have been dramatically improved. For instance, conventional casting has been replaced by directional casting and in many cases by single crystal superalloys [4]. The absence of grain boundaries resulted in enhanced creep and fatigue properties. However, polycrystalline superalloys are still utilized effectively as components on hot sections of IGTs, such as guide vanes, where single crystal alloys cannot be cast due to their complicated geometries, *i.e.* internal cooling system.

A large number of polycrystalline superalloys which are currently used in IGTs were developed nearly 40 years ago, such as IN738 and IN792, and they limit the maximum operating temperature of IGTs [6]. However, the increase in efficiency and the reduction of carbon emissions of the IGTs are growing in importance. These

requirements can only be addressed by designing new polycrystalline nickel-based superalloys which can withstand higher temperatures and exhibit mechanical properties superior to those currently used.

The mechanical properties of polycrystalline superalloys are mainly controlled by the fracture toughness and strength of their grain boundaries. Thus, during the design of new superalloys it is necessary to have a thorough understanding of the correlation between grain boundary elements, such as boron and carbon, and optimal grain boundary character. In addition, studies on the relationship between grain boundary character and mechanical properties, such as creep, at elevated temperatures are of utmost importance.

The beneficial effect of boron and carbon on the improvement of mechanical properties of superalloys has been well known for over 50 years [7,8]. However, until today how these grain boundary strengtheners enhance the mechanical properties is not well understood. Many scientific questions still remain open. For instance, how much boron is required to achieve the optimal creep performance? Does boron reside at grain boundaries as elemental segregation or as a second phase? Are the MC carbides beneficial or detrimental for the mechanical properties of polycrystalline superalloys?

The current study aims to provide new insights, answer the scientific questions identified above and extend our knowledge around the grain boundary elements and their effect on superalloys. For that purpose, a prototype composition of a new polycrystalline nickel-based superalloy with different boron contents and a conventionally cast superalloy for industrial gas turbines are studied.

The improvement of the detection limits of light elements, such as boron and carbon, in various characterisation methods over the last decades allows in depth

studies of the grain boundary chemistry. Systematic characterisation analyses of grain boundaries conducted in this study provide new information about the grain boundary character of superalloys for IGTs. In addition, through *in-situ* investigations the relationship between the optimal grain boundary character and mechanical properties was studied, elucidating the deformation mechanisms taking place during deformation at elevated temperatures. Finally, novel crack growth measurements were conducted under thermal–mechanical conditions and were correlated with microstructural features, such as carbides. The controversial character of carbides and their effect on superalloys was evaluated.

1.3 Structure of Thesis

Chapter 2 begins with an overview of the physical metallurgy of nickel-based superalloys. The importance of carbon and boron as grain boundary strengtheners in superalloys is considered. In addition, the processing of superalloys for the production of polycrystalline superalloys for IGTs is outlined. Finally the grain boundary fracture mechanisms are reviewed; the cavity nucleation and growth mechanisms are highlighted.

In Chapter 3 the details about the processing of the superalloys used in this study are given. A new polycrystalline superalloy suitable for novel guide vanes, called STAL15-CC, and the well-known IN792 were used. In addition, the methods utilised for the microstructural characterisation of these alloys are described in detail.

In Chapter 4 the effect of boron on the grain boundary character of STAL15-CC alloy is investigated. A boron-free and three boron variants are produced. Detailed high-resolution characterisation of the grain boundaries of all STAL15-CC variants is conducted. The microstructural characterisation of grain boundaries in heat-

treated condition allowed a thorough understanding of how boron controls the grain boundary character of this new polycrystalline superalloy. The optimal boron content to achieve the best creep performance in terms of creep rupture time is also evaluated. Thus, conclusions are drawn for the correlation between grain boundary character and creep behaviour.

In Chapter 5 a mechanism through which boron improves the mechanical properties at elevated temperatures is proposed. For that purpose a boron-free and a boron-containing variant of STAL15-CC are tested in tension. *In-situ* investigations are carried out at elevated temperatures providing insights of the fracture mechanism and crack propagation along the grain boundaries. High-resolution strain mapping analyses support the *in-situ* observations. The importance of boron as the primary grain boundary strengthener is elucidated.

In Chapter 6 the effect of carbides on the thermal–mechanical fatigue performance of IN792 is studied. Crack growth measurements were performed under different conditions and dwell times. Crack growth rates were correlated with microstructural observations providing insights into the crack initiation sites and crack propagation character. The presence of carbides in the microstructure of IN792 is evaluated and conclusions are drown regarding the controversial effect of carbon in superalloys.

Finally, in Chapter 7 a summary of the key conclusions from this research study is given. Suggestions for future work necessary to improve our understanding about the grain boundary elements and their effect on superalloys are made.

Chapter 2

Literature Review

2.1 Nickel-Based Superalloys

2.1.1 Physical Metallurgy of Superalloys

The compositions of some common nickel-based superalloys are given in Table 2.1. It is apparent that superalloys are complex materials, considering the number of the alloying elements, normally larger than ten, required to achieve their desired properties. This mixture of elements results in a microstructure consisting of a continuous austenitic gamma (γ) matrix decorated with gamma-prime (γ') precipitates. Often various types of carbides and borides precipitate along the grain boundaries as a result of the addition of grain boundary strengthening elements carbon (C) and boron (B).

Table 2.1: Summary of chemical compositions of various nickel-based superalloys (at.%) [4].

Alloy	B	C	Co	Cr	Mo	W	Al	Ta	Ti	Nb	Hf	Zr
IN738-LC	0.05	0.52	8.2	17.5	1.0	0.8	7.2	0.6	4.0	0.6	-	0.02
IN939	0.05	0.70	18.1	24.1	-	0.6	4.0	-	4.3	0.6	-	0.06
Mar-M247	0.08	0.80	10.1	9.2	0.4	3.3	12.2	1.0	1.3	-	0.5	0.02
Rene 80	0.08	0.80	8.8	15.5	2.4	1.3	6.4	-	5.6	-	0.3	0.01
Astroloy	0.16	0.28	16.2	16.2	3.1	-	8.3	-	5.5	2.1	-	-
GTD-111	0.07	0.48	9.3	15.6	0.9	1.2	6.4	1.0	6.0	-	-	0.01

Figure 2.1 illustrates the position of the different elements in the periodic table and the phase to which they partition. However, the amount of each element needs to be carefully selected in order to avoid the formation of undesirable topologically close-packed (TCP) phases. Further details for each phase are given in the subsequent sections.

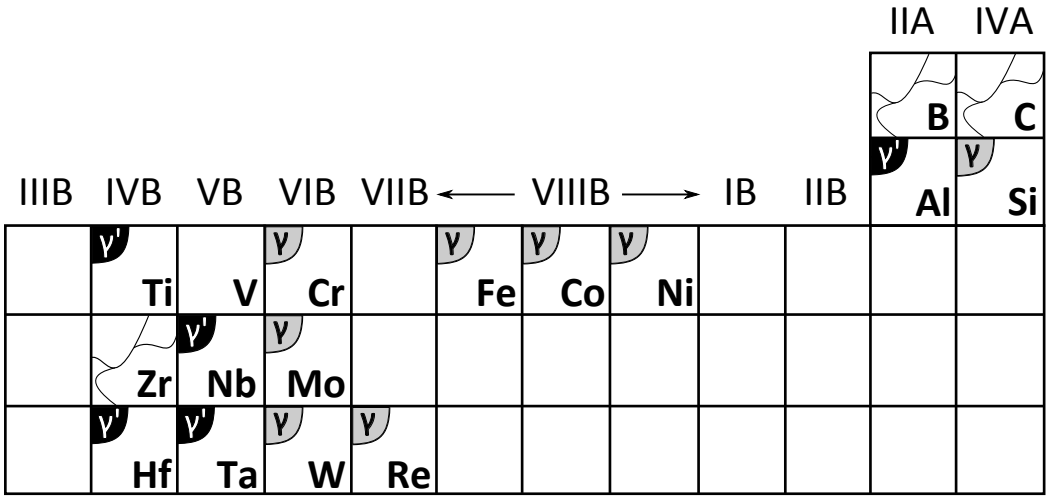


Figure 2.1: Elements important in the constitution of nickel-based superalloys and their position in the periodic table [6].

2.1.1.1 The γ matrix

The typical microstructure of a superalloy consists of a continuous austenitic γ matrix of the face centred cubic (FCC) structure in which the other phases reside. It can accommodate high concentrations of elements in solid-solution such as chromium (Cr), cobalt (Co), molybdenum (Mo) and tungsten (W). Their atomic radii are not very different from that of nickel and therefore they prefer to reside in this phase. Additions of Cr, Mo, W and Co can strengthen the γ matrix by inhibiting dislocation motion. In addition, such solid solution elements can lower the stacking-fault energy, particularly Co [9]. Lowering the stacking fault energy results in increased spacing between partial dislocations. Thus the movement of dislocations becomes more difficult and high temperature properties are improved [10].

2.1.1.2 The γ' phase

The γ', ordered Ni_3Al, precipitates are the important strengthening phase in many nickel superalloys. They exhibit a cubic, $L1_2$, crystal structure with Al atoms at the cube corners and Ni atoms at the centre of the faces, as illustrated in Figure 2.2. In addition, elements such as titanium (Ti), tantalum (Ta) and niobium (Nb) can substitute for Al sites [11].

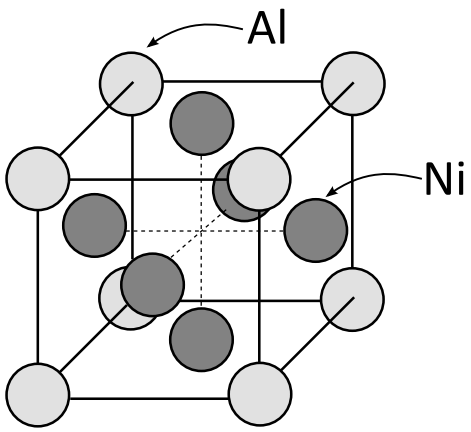


Figure 2.2: Arrangements of Ni and Al atoms in the ordered Ni_3Al phase [4].

The properties of superalloys depend substantially on the coherency of the γ/γ' interface. The compositions of the γ and γ' phases will alter the mismatch and consequently the morphology of the γ' particles. The lattice misfit between those two phases is defined according to

$$\delta = 2 \times \left[\frac{\alpha_{\gamma'} - \alpha_{\gamma}}{\alpha_{\gamma'} + \alpha_{\gamma}} \right] \tag{2.1}$$

where α_{γ} and $\alpha_{\gamma'}$ denote the lattice parameters for the the γ and γ' phase, respectively. The lattice parameter can be calculated based on the chemical composition as described by Vegard's Law [12]. In the case of small misfit (less than 0.5 %), the γ' particles exhibit a cuboidal morphology with sharp corners. As the magnitude of the lattice misfit increases, the precipitates become more spherical, due to loss of coherency [4]. Ricks *et al.* [13] observed the development of γ' particles in various superalloys during heat treatment. It was found that the morphological evolution of γ' particles occurs in the following sequence: spheres, cubes, arrays of cubes and finally solid-state dendrites, as illustrated in Figure 2.3. This evolution sequence was not observed to be affected by positive or negative misfitting. However, the magni-

tude of lattice misfit was found to affect the required size of the γ' particle before the transformation from spherical to cuboidal shaped to occur. It was suggested that in the case of small lattice misfit, the γ' particles need to grow to a larger size before the cuboidal form is occurred.

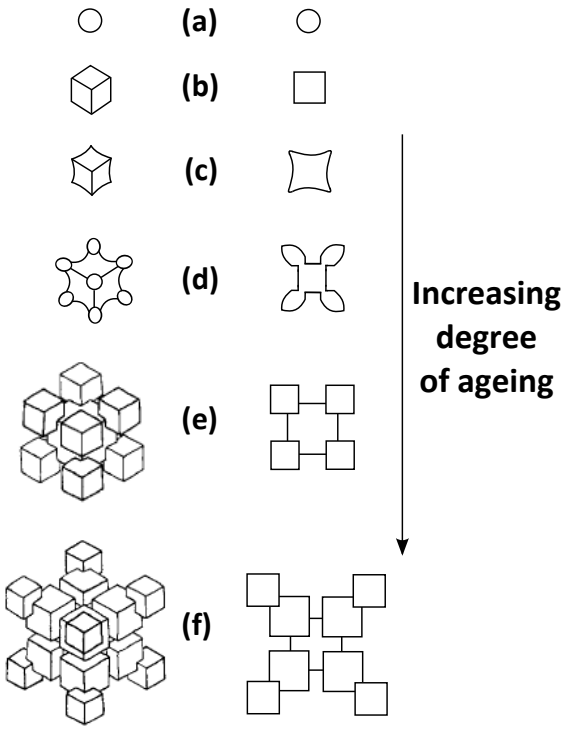


Figure 2.3: Schematic diagram illustrating the development, from (a) to (f), of strain-induced, facetted γ' morphologies during heat treatment: left, projection along $\langle 111 \rangle$ and right, projection along $\langle 001 \rangle$ [13].

2.1.1.3 Topologically close-packed (TCP) phases

During heat treatment processes or prolonged service hours, undesirable phases can form. Some of the most common phases include sigma (σ), mu (μ), eta (η) and Laves [14]. TCP phases are detrimental for the mechanical properties of superalloys. First, their formation is normally promoted by relatively high amounts of Cr, Mo, W or Re [15]. As a consequence solid solution elements are removed from the matrix

resulting in a decrease of creep resistance [16, 17]. Second, they often precipitate in the vicinity of grain boundaries and can exhibit a needle-shape morphology, which can serve as crack initiation sites and facilitate crack propagation [18, 19]. Thus, it is important that the composition of superalloys is carefully selected.

2.2 Grain Boundary Strengtheners

2.2.1 Carbon

The role of carbon in superalloys is complex. The different types of carbides have a controversial influence on the mechanical properties of superalloys. First, the chemical stability of the matrix can be influenced by the formation of carbides and the consumption of reacting elements [6]. Second, the morphology of carbides can influence the mechanical properties. For instance, needle-shape carbides can serve as crack initiation sites and accelerate crack propagation [20]. Today, the presence of carbon in a variety of superalloys is widely accepted to exert a beneficial effect on the high-temperature mechanical properties when carbon content is kept within the range of $\sim$0.02-0.09 wt.% C [21].

Carbon is therefore commonly mentioned as a grain boundary strengthener. This definition rationalises indirectly the higher content of carbon in polycrystalline superalloys in contrast to lower contents in single crystal superalloys, where grain boundaries are absent [4].

2.2.1.1 Types of carbides

The most common types of carbides which form in nickel-based superalloys are the MC, $M_{23}C_6$ and M_6C. The MC carbides are considered to be the most stable carbides found in nature: M stands for elements such as Ti, Ta, Hf or Nb. In addition, they precipitate at high temperatures directly from the liquid phase [4, 22] and serve as the main source of carbon for subsequent reactions during either protracted service exposure, or heat treatment processes [6]. MC carbides are also observed with different morphologies, for example as blocky particles, needles or as a continuous network of script carbides, mostly in the interdendritic regions, as illustrated schematically in Figure 2.4 [23]. The various morphologies are mainly driven by the carbide growth rate. For instance, relatively long solidification times facilitate the growth of octahedron-shaped MC carbides (Figure 2.4(a)), whereas fast cooling rates promote the formation of the detrimental script-type carbides (Figure 2.4(j)). Intermediate cooling rates can result in carbides where arms start to develop from the octahedral corners (Figure 2.4(e)).

As has been shown [22, 24], the morphology of MC carbides is determined not only by the carbide growth rate but also by the addition of different elements such as Hf [20, 25, 26]. In particular, it was observed that a relatively large lattice misfit at the MC/matrix interface implies the precipitation of blocky carbides, whereas a lower lattice misfit leads to script-type carbides. The increase of lattice misfit was accomplished via the addition of Hf in the composition of the alloy. Chen *et al.* [24] observed that different levels of Hf for the same alloy result in different MC morphologies. Calculations of the lattice misfit for different amounts of Hf have verified this previous observation [24].

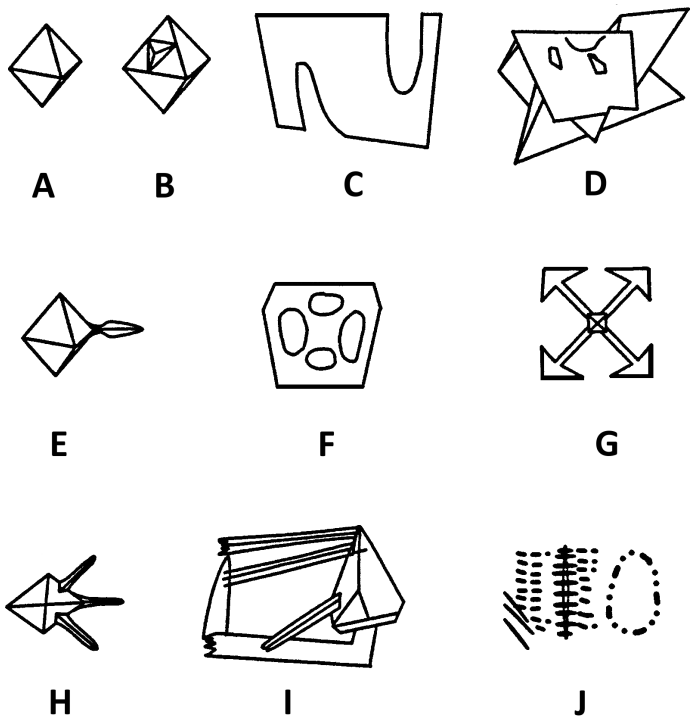


Figure 2.4: Schematic illustrations of the MC-type carbide morphology at different carbide growth rates. The carbide growth rate increases gradually from A to J [23].

The morphology of MC carbides is crucial for the mechanical properties of superalloys. The presence of script-like MC carbides in the interdendritic region affects adversely the creep properties of superalloys; crack initiation along the carbides is facilitated [21, 25]. On the other hand, script-type MC carbides located in either dendritic core or arms exert a strengthening effect [21]. The most preferred morphology is dispersed blocky discrete carbide particles along the grain boundaries. Thereby, grain boundary sliding is prohibited, leading to the improvement of creep properties [20].

The $M_{23}C_6$ carbides are the most abundant in nickel-based superalloys with high chromium content and they mainly precipitate at grain boundaries. Fine $M_{23}C_6$ carbide particles which are uniformly distributed prohibit grain boundary migration

during deformation improve strength, thus being advantageous to the mechanical properties of the alloy [27, 28]. Nonetheless, crack initiation and propagation can be accentuated either by the decohesion of $M_{23}C_6$ interface with matrix or by the fracture of these particles during low cycle fatigue [6, 28]. The decomposition of MC carbides results in carbon accumulation in the matrix. It serves as the substantial source of carbon for the $M_{23}C_6$ formation at lower temperatures (760-980 °C), during either heat treatment processes or prolonged service exposure [6]. It is worth mentioning the close relationship of the complex cubic structure of $M_{23}C_6$ carbide with the TCP σ phase, when carbon atoms are removed. The nucleation of σ phase on $M_{23}C_6$ carbides is attributed to their high coherency [15].

A complex cubic structure denotes the presence of M_6C type carbides which constitute the product of the following reaction MC+$\gamma \rightarrow M_6C+\gamma'$, when the presence of refractory metals such as molybdenum and/or tungsten content is more than 6 to 8 at.%. Furthermore, M_6C carbides are most stable above 1000 °C, a temperature slightly higher than for $M_{23}C_6$ carbides (950-1000 °C). Hence, M_6C are more preferable since their contribution to control of grain size and strengthening of grain boundaries is higher [6,29]. In addition, profuse precipitation of blocky M_6C carbides confers a beneficial effect on mechanical properties, particularly creep resistance. This is consistent among several studies [27, 29], which have shown the movement of dislocation is impeded, through tangling and pinning. Moreover, the interface of matrix with M_6C carbides is not susceptible to crack initiation and propagation. By contrast, needle-shape M_6C carbides, which are often found cracked during creep tests, are detrimental to creep properties due to their shape and brittleness.

2.2.1.2 Decomposition of MC carbides

Superalloys are designed to be utilised under high temperatures and stresses. During protracted periods of service exposure a range of microstructural changes are expected, for instance, coarsening of γ' phase, TCP phase formation and MC carbide decomposition. MC decomposition is a controversial subject. Some researchers suggest that a degradation of mechanical properties by the decomposition of MC carbide occurs [30]. By contrast, other researchers suggest that the products from the decomposition of MC carbides can improve grain boundary strengthening by impeding their migration [28].

The dominant carbide reactions in many superalloys are MC+$\gamma \rightarrow M_{23}C_6+\gamma'$ and MC+$\gamma \rightarrow M_6C+\gamma'$. These are cited in different studies and have been accepted by the research community [6, 28, 30]. The MC-type carbides are susceptible to decomposition with thermal exposure either into $M_{23}C_6$ or M_6C, dependent on the superalloy composition. In particular, the degeneration of MC is stimulated by the substitution of the main carbide forming elements such as Ti and Nb with Mo, Ni and Cr. As a consequence, a decrease in stability of MC occurs through the weakness of the interatomic bonds and MC carbides serve as source of carbon for the subsequent reactions. In case of high chromium content superalloys, chromium is depleted from the matrix and helps form $M_{23}C_6$ carbides, whereas in superalloys with adequate content of Mo and/or W the formation of M_6C type carbides is facilitated, at slightly higher temperatures than needed for $M_{23}C_6$ [6, 31].

Nonetheless, as superalloys have evolved to address issues such as longer service lifetimes and higher operating temperatures, novel reactions for the MC decomposition have been reported. According to the reviews in [31, 32], the hexagonal closed-packed Ni_3Ti (or Ni_3Ti,Ta) η phase occurs during the decomposition of MC

carbide via the reaction MC+$\gamma \rightarrow M_{23}C_6+\eta$. The degeneration of MC carbides implies the agglomeration in the vicinity of the decomposition zone of carbon, titanium and tantalum, because of the outward diffusion. At the same time, nickel, chromium and cobalt diffuse from the matrix. Therefore, it is likely that the local concentration of titanium and tantalum reach the stoichiometry of the η phase. The presence of this phase in the alloy is known to be deleterious to the mechanical properties [32].

The precipitation of a phase on the η layer, as a consequence of the formation of η phase has also been reported [33, 34]. The solubility of Mo and W is hindered through the existence of η phase and thereby the preferred conditions for the formation of the BCC α-(W, Mo) phase are locally created. Figure 2.5 illustrates the precipitation of η and α phases, during a range of thermal exposures.

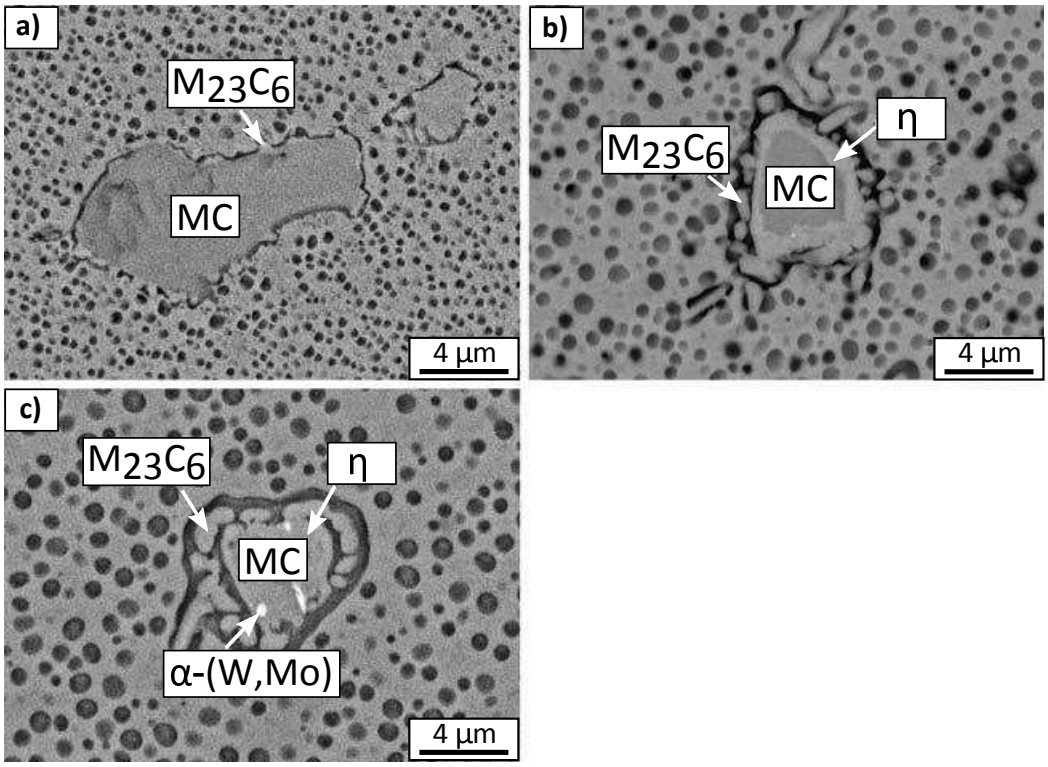


Figure 2.5: Backscattered electron images of degenerated MC carbides under the different exposure conditions: a) 800 °C/1000 h, b) 850 °C/5000 h and c) 900 °C/10000 h [33].

2.2.1.3 The effect of carbides on porosity

An improvement of the mechanical properties, such as creep resistance, of cast materials results by the reduction of microporosity. Vacuum technology led to the annihilation of porosity arising from gas evolution during the casting process. As a consequence, any microporosity present is mainly associated with solidification shrinkage [35, 36].

A range of factors influence the density, volume fraction and distribution of microporosity. For instance, the formation of microporosity depends on the chemical composition of the cast material. The most comprehensive studies on the effect of different elements on porosity in nickel-based superalloys have been conducted by Lecomte-Beckers, whose results are presented in Table 2.2 [35].

Table 2.2: The effect of alloying elements on microporosity in nickel-based superalloys [35].

Alloy	**Effect**
Al	Detrimental
Cr	Beneficial
Co	Detrimental
Ti	Detrimental and Beneficial
Mo	Detrimental and Beneficial
C	Detrimental and Beneficial

As it can be seen in Table 2.2, the effect of carbon has a controversial character on microporosity. More specifically, some researchers suggest that the MC carbides in the interdendritic regions resulting from the carbon additions in the superalloys increase microporosity. During solidification, they serve as obstacles and impede the natural flow of molten metal [37]. By contrast, microporosity affiliated with the final stages of solidification can be alleviated by the formation of MC-type carbides in

the interdendritic pools [20]. The latter can be attributed to the fact that lattice expansion both in MC phase and the matrix is caused by carbon atoms when they occupy the octahedral interstitial vacancies of the matrix lattice, as illustrated in Figure 2.6. Therefore, the formation of MC carbides implies that more interdendritic space is filled, in comparison to the same amount of γ/γ'.

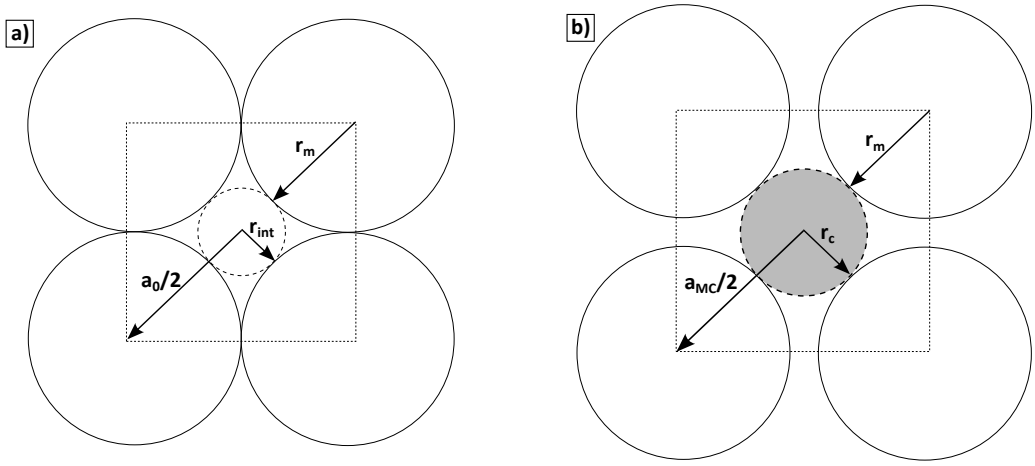


Figure 2.6: The (001) plane of FCC structure: a) interstitial-free and b) with carbon atoms in the interstitial sites [38].

2.2.2 Boron

Boron is thought of as a second main grain boundary strengthener for the polycrystalline and directionally solidified superalloys. Opinion has been divided over the effect of boron on the mechanical properties, but it is now widely accepted that boron exerts a beneficial effect, particularly on creep resistance of superalloys [39].

Boron segregates at the grain boundaries mainly due to its atomic size. In particular, smaller atoms segregate at grain boundaries where large vacancies exist; the number of vacancies is relatively higher at grain boundaries than that of grains. In addition, Speiser *et al.* [40] has shown that in the 55Ni-20Cr-15Co-4Mo-3Ti-3Al

alloy boron is 78 % larger than the available interstitial space and 26 % smaller than the substitutional space. As as a consequence, boron fits poorly both interstitially and as a solute, hence segregates to the grain boundaries.

For that reason, borides are found to reside primarily at grain boundaries. Borides are sometimes observed near solidification pores. This is explained by the fact that borides are formed during the last stage of solidification [41]. It is also suggested that borides are developed at the vicinity of the γ/γ' eutectic regions [42], as a result of simultaneous presence of Cr, Mo and B, which are strong boride formers, in the final residual liquid. Cr and Mo segregate into the residual liquid during the γ/γ' eutectic formation in nickel-based superalloys and B segregates strongly into the liquid phase, due to its low solubility in γ and γ'. Therefore boride formation is favourable in the vicinity of γ/γ' eutectic. The most common types of borides are M_3B_2 with a tetragonal crystal structure and M_5B_3 with a body-centred-tetragonal structure [43].

2.2.2.1 The effect of boron on carbides and γ' envelopes

As described in section 2.2.1.2, the decomposition of MC-type carbides results in the formation of the $M_{23}C_6$ carbides and γ' in superalloys with high Cr levels. The presence of this particular type of carbides is beneficial only when they are uniformly distributed along the grain boundaries [27]. During prolonged service exposures $M_{23}C_6$ carbides can agglomerate at grain boundaries forming a continuous film and serving as crack initiation sites, particularly at grain boundaries transverse to the applied stress [33].

Decker and Freeman [7] proposed that boron can retard the detrimental agglomeration of $M_{23}C_6$ along the grain boundaries. The stages of micro-crack forma-

tion caused by the precipitation of a continuous layer of $M_{23}C_6$ carbides along the grain boundaries are illustrated in Figure 2.7.

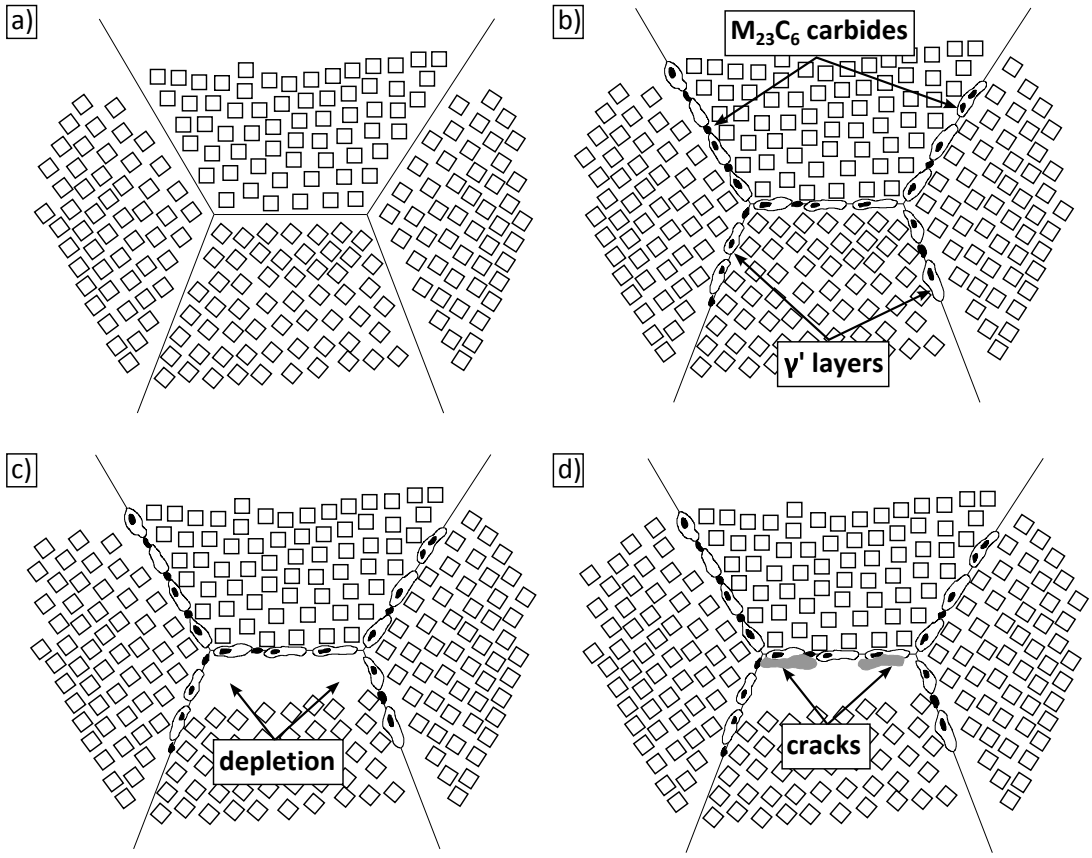


Figure 2.7: Agglomeration of γ' and $M_{23}C_6$ particles and crack initiation at grain boundaries: a) initial microstructure, b) agglomeration of γ' and $M_{23}C_6$ along the grain boundaries, c) formation of γ' denuded zones and d) crack initiation at γ' denuded zones at grain boundaries transverse to load axis [7].

In particular, in Figure 2.7(a) the initial microstructure is depicted, whereas Figure 2.7(b) corresponds to the stage of γ' and $M_{23}C_6$ agglomeration at the grain boundaries. The formation of the Cr-rich carbides drives the diffusion of chromium towards the grain boundaries. Thereby, a γ' depleted zone occurs next to grain boundaries which corresponds to the chromium depleted area; see Figure 2.7(c).

The depletion of chromium increases the solubility for nickel and aluminium and consequently results in γ' disappearing [7]. The γ' depleted zone combined with the continuous layers of $M_{23}C_6$ at the grain boundaries result eventually in formation of micro-cracks (Figure 2.7(d)).

However, superalloys with minor additions of boron are less subject to a rapid agglomeration of carbides at grain boundaries and consequently were less prone to intergranular cracking, particularly at grain boundaries transverse to the applied stress [7, 44, 45]. Their fracture resistance is therefore improved. This effect supports the theory that boron can serve as grain boundary stabilizer which can retard microstructural changes. However, superalloys containing excessive amounts of boron were found to be more susceptible to brittle fracture; their fracture resistance was similar to those containing no boron. This undesirable effect of boron was rationalised by its high affinity with elements such as molybdenum, titanium, chromium and niobium, which can cause the formation of borides. Borides could potentially serve as crack initiation sites [45].

The second product of the MC carbide decomposition can lead to the formation of γ' layers along the grain boundaries. Carbides are enveloped within these layers. This particular structure at grain boundaries was observed only in some alloys, which implies the composition of each alloy strongly affects the formation of the γ' envelopes. It is suggested that this complex structure at grain boundaries can improve the mechanical properties and fracture resistance [46].

More specifically, the hard grain boundary carbides enveloped within the ductile γ' envelopes retard the crack initiation and thereby improve the time to rupture and creep ductility at high temperatures [6]. In other studies it was found that γ' envelopes can form around the decomposed MC-type carbides without precipitation

of $M_{23}C_6$-type carbides, which was still found to impede crack propagation [46]. The presence of γ' envelopes at grain boundaries can indirectly control the precipitation of $M_{23}C_6$ carbides at grain boundaries by suppressing the diffusion of chromium. As a consequence these envelopes can impede the carbide agglomeration at grain boundaries and retard the onset of intergranular cracking [46].

The formation of the γ' envelopes is not completely understood. Some researchers have attempted to ascribe the formation of γ' envelopes to the precipitation of $M_{23}C_6$ carbides containing relatively high boron content [46, 47]. It has been shown in previous studies that boron can substitute for carbon during the formation of carbides, thereby forming $M_{23}(B,C)_6$ carbides [8, 48]. This observation can be rationalised by the relatively higher mobility of boron in the γ matrix than that of carbon. A higher amount of boron can diffuse from the γ matrix towards the growing $M_{23}C_6$ carbide, thereby resulting in high boron carbide [47].

The overall interfacial energy around a carbide includes the $\sigma_{M_{23}C_6/\gamma}$, $\sigma_{M_{23}C_6/\gamma'}$ and $\sigma_{\gamma/\gamma'}$. The presence of boron in $M_{23}C_6$ carbide can cause an increase in the lattice misfit of $M_{23}C_6/\gamma$ and $M_{23}C_6/\gamma'$ interfaces due its large atom size and thus the interfacial energy can increase [46]. Therefore, in order to compensate for the increase of the overall interfacial energy, the interface between the γ and γ' around the carbide needs to decrease in area. Boron can therefore indirectly facilitate the formation of γ' envelopes [46]. In terms of composition, the decomposition of the MC carbide can provide the γ' forming elements, such as Ta and Ti, around the decomposed region and consequently facilitating the formation γ' envelopes.

The mechanisms through which boron improves the mechanical properties and its importance on the performance of superalloys is reviewed in greater detail in Chapter 4; there the role of boron on the grain boundary character of a new poly-

crystalline superalloy is discussed.

2.3 Processing of Superalloys

The chemistry of superalloys is the controlling factor for processing route selection. For instance, powder metallurgy (P/M) is utilised for the production of alloys designed for disk applications. Powder metallurgy is selected over conventional ingot metallurgy to eliminate segregation during the production of superalloys. Nevertheless, in some cases where the content of elements such as Al, Ti and Nb is low, ingot metallurgy is preferred due to lower production costs when compared to powder metallurgy. In this study superalloys used for blades and guide vanes were studied, and were therefore produced by investment casting (the 'lost-wax'process) [49, 50].

2.3.1 Investment Casting

For investment casting, first a master melt is produced using a vacuum induction melting (VIM) furnace; a typical VIM furnace is illustrated in Figure 2.8. The first step of investment casting involves the production of a disposable pattern by injecting molten wax into a metallic die. Next, a ceramic shell is prepared by dipping the pattern into ceramic slurries consisting of binding agents and mixtures of zircon ($ZrSiO_4$), alumina (Al_2O_3) and silica (SiO_2). This step is followed by a step of stuccoing with larger particles of these same materials. The last two stages are performed from three to six times, depending on the required thickness. Finally, the wax is removed by steam and the pattern is baked in order for the ceramic layer obtain its strength. This produces a ceramic mould, which can receive molten superalloy metal. The steps of the investment casting are illustrated in Figure 2.9.

The metal can solidify under various conditions, for instance in a case where no specific heat control is applied, the process is called conventional casting (CC). Under other conditions directional solidified (DS) or single crystal (SC) products can be produced. In the case of conventional casting the grain size, which is vital for the required mechanical properties such as creep, is controlled by a range of parameters. One of these parameters is the addition of modifiers in the primary slurry for the production of the ceramic mould. Such modifiers include cobalt aluminate and serve as nucleation catalysts that reduce the grain size. The effect of cobalt aluminate on the grain size is discussed in subsequent section.

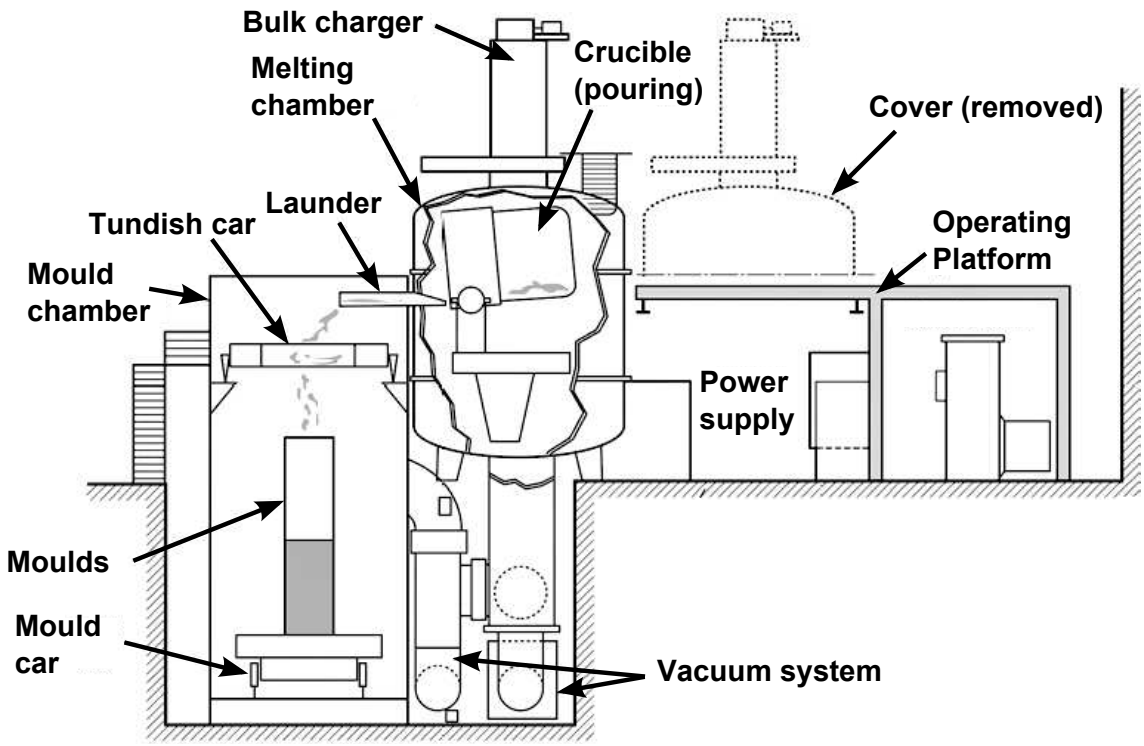


Figure 2.8: Schematic illustration of a double-chamber vacuum induction melting furnace [51].

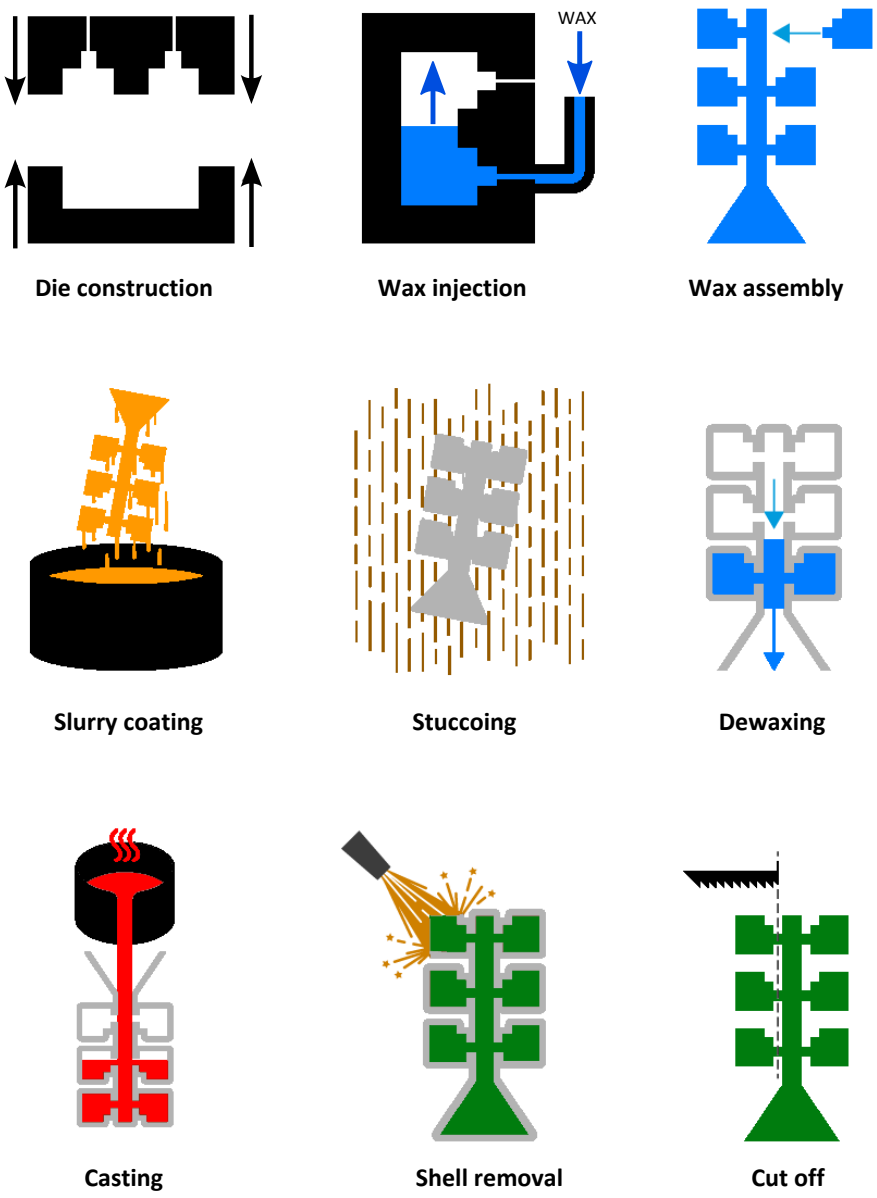


Figure 2.9: Schematic illustrations of the various steps of investment casting process [52].

2.3.2 The Effect of Cobalt Aluminate on Grain Size

According to the review in reference [53], a stable spinel, called cobalt aluminate ($CoAl_2O_4$) strongly influences nucleation in nickel superalloys during investment casting. Minor additions of cobalt aluminate in the primary slurry can dramatically change the grain size of the cast superalloy by increasing the number of grain nucleation sites [53]. The characteristic blue colour of cobalt aluminate after application on a wax pattern is illustrated in Figure 2.10.

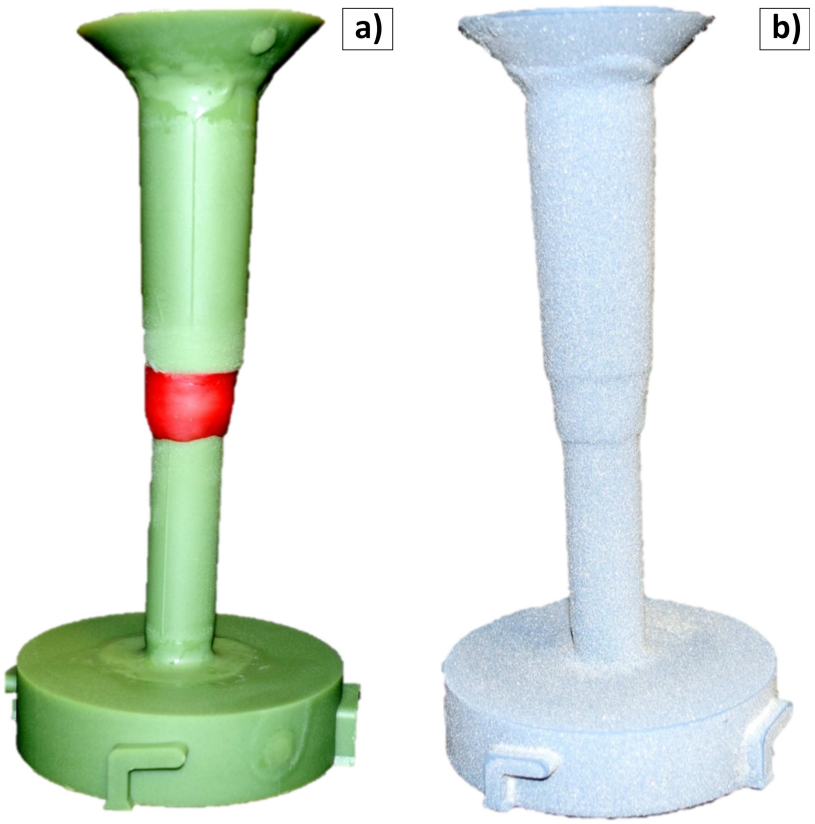


Figure 2.10: Assembled wax pattern for the casting of a single tapered rod bar: a) before any slurry is applied b) after cobalt aluminate and stucco are applied. Note the characteristic blue colour caused by the cobalt aluminate.

The large number of nucleation sites is a result of a reaction between cobalt aluminate with elements such as Al, Cr, etc. at high temperature in vacuum conditions. Cobalt from the cobalt aluminate addition is displaced by these elements and pure Co fine particles are produced [54]. Grain refinement is provided by nucleation and the extensive growth of crystals is impeded. However, greater grain refinement and improvement of mechanical properties cannot be achieved by further addition in the primary slurry of cobalt aluminate [53]. An example of the effect of cobalt aluminate on the grain size of René 77 is illustrated in Figure 2.11. It is shown that the addition of cobalt aluminate in the primary slurry results in a higher number of grains; thus the grain size is decreased.

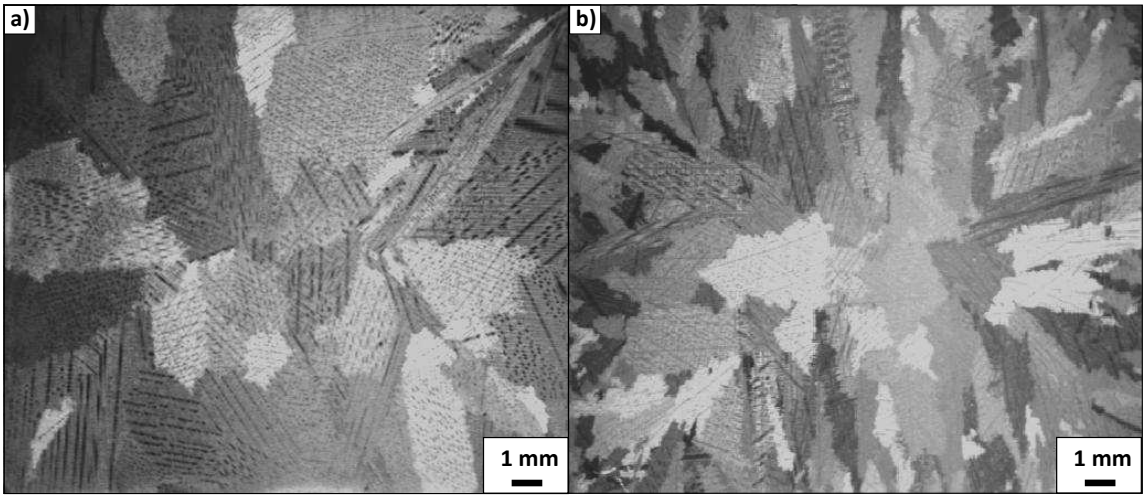


Figure 2.11: The macrostructure of the superalloy René 77 from the cross section of castings in ceramic moulds with: a) no cobalt aluminate and b) modified with 5 % mass of $CoAl_2O_4$ [53].

In the same study, an influence of cobalt aluminate on the shape and size of carbides was observed. In castings where cobalt aluminate was added in the primary slurry, carbides were found to be thinner than in unmodified castings and the creep

rupture times were improved [53]. Other studies have shown that the interdendritic segregation of elements such as Cr, Mo and Ti decreases with decreasing grain size [55, 56]. This observation implies that grain refinement resulting from the addition of cobalt aluminate in the primary slurry can control segregation of elements during solidification.

2.3.3 Hot Isostatic Pressing (HIP) - Microporosity

Microporosity is considered to be the main inevitable defect caused by solidification processing which adversely affects the mechanical properties. Microporosity can be partially diminished through the control of composition and the casting process, however this undesirable imperfection can only be removed by HIP. Figure 2.12 illustrates the porosity measured before and after HIP for the MAR-M247 superalloy. The reduction of porosity by HIP can be observed for various grain sizes [57].

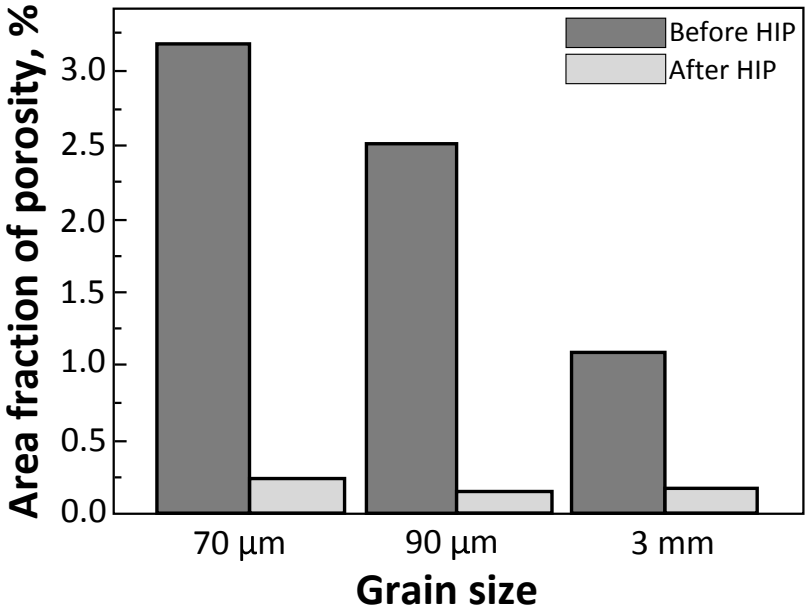


Figure 2.12: Level of microporosity before and after HIP from samples of various grain sizes of MAR-247 [57].

HIP effectively reduces the amount of microporosity in the interdendritic areas and at the grain boundaries, and it could cause the coarsening of γ' phase. Hot isostatic pressing is performed under hydrostatic pressure at high temperatures. The γ' phase can coarsen under those conditions so that the coherency with the matrix can be lost. Solution annealing and ageing treatment should be considered as the subsequent processes of HIP in order to utilize the beneficial character of HIP and obviate the undesirable degradation of mechanical properties. The solid solution temperature needs to be slightly higher than the HIP temperature, hence coarsened γ' particles are dissolved [58].

The total removal of porosity does not automatically imply enhancement of the mechanical properties, because the performed HIP properties may alter the microstructure of the cast superalloy [59]. HIP is not only utilized to improve the mechanical properties of equiaxed solidified investment cast components, but also to rejuvenate parts of hot sections, such as turbine blades, by removing creep porosity developed during service [60].

2.4 Grain Boundary Fracture

Creep resistance of components for high temperature applications is of considerable concern in engineering. Creep can lead to failure even when then applied stress is lower than the yield stress. The grain boundaries serve as the main void initiation sites and therefore their character plays a pivotal role on creep performance of superalloys. Two main types of fracture have been observed and related to grain boundary deterioration.

The first fracture mode resulting from accumulation of creep plasticity can occur by *w* or wedge-type cracking as illustrated in Figure 2.13. This mode is expected

to occur under high stresses (lower temperatures) and large grain sizes, particularly when grain boundary sliding is impeded [61].

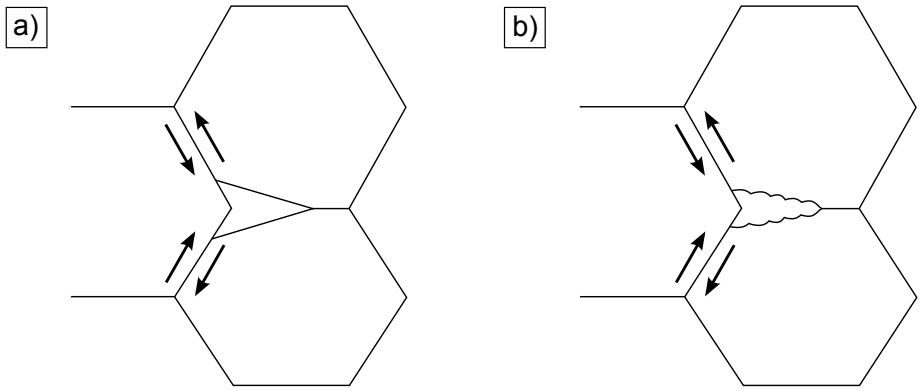


Figure 2.13: Creep fracture modes: a) a wedge crack formed at the triple junctions and b) a wedge crack as an accumulation of spherical cavities [62].

The second type of fracture is related to r-type irregularities or cavities forming at grain boundaries perpendicular to load axis as illustrated in Figure 2.14. The agglomeration of r-type voids can sometimes lead to formation of wedges as shown in Figure 2.13(b).

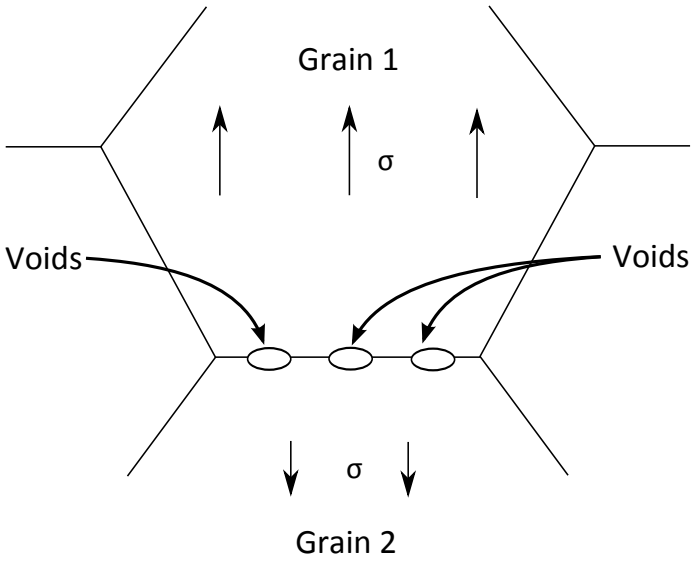


Figure 2.14: Cavitation (r-type) or voids at a transverse grain boundary [62].

The creep fracture in uniaxial tension under constant stress has been described by the Monkman-Grant relationship, in which the fracture depends on the steady-state creep rate $\dot{\epsilon}$ according to the following equation:

$$\dot{\epsilon}^{m''} t_f = k_{\mathrm{MG}} \tag{2.2}$$

where Monkman-Grant constant is denoted as k_{MG}, t_f is time to fracture and m'' is a constant typically about 1.0 [63]. Apart from the Monkman-Grant relationship, the Larson-Miller parameter is exploited for the prediction of rupture time of creep-deforming materials, described by $LM = T\left[\log t_r + C_{LM}\right]$ [64]. C_{LM} is suggested to be approximately 20, independent of the material and additionally it must be noted that this equation is not derived by Monkman-Grant relationship.

2.4.1 Cavity Nucleation

Several studies have shown that grain boundaries serve as the predominant sites for cavity nucleation. In particular, cavities are prone to appear at grain boundaries perpendicular to the tensile axis [65–68]. Different theories have been suggested regarding the nucleation of cavities, such as grain boundary sliding resulting to voids at a triple point of a grain boundary, vacancy condensation at grain boundaries regions of high-stress concentration and cavity formation at the head of dislocation pile-up at a grain boundary [62]. Schematic illustrations of these mechanisms are shown in Figure 2.15.

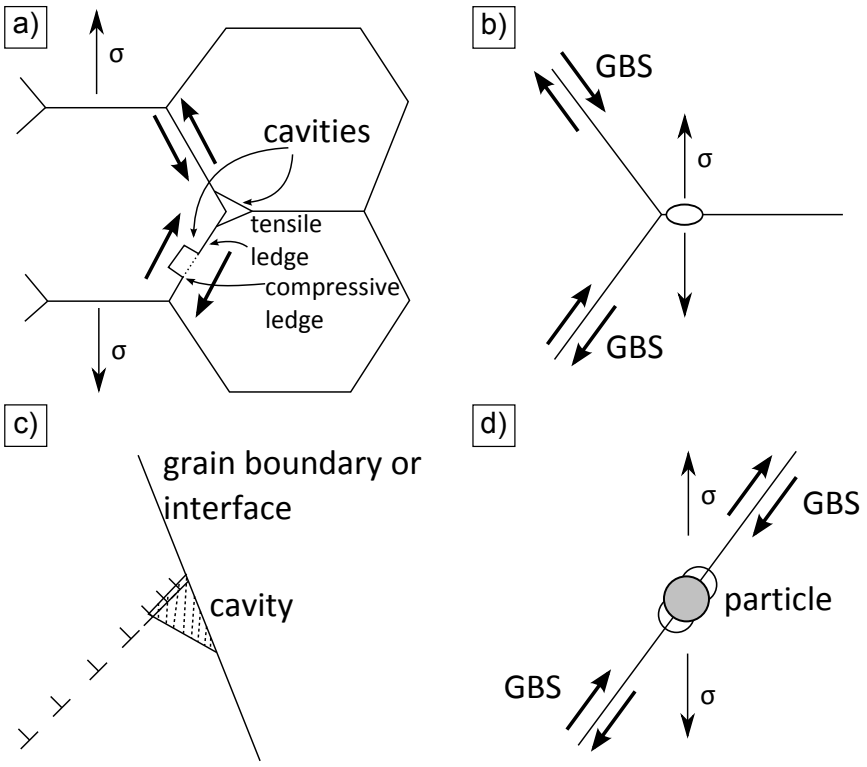


Figure 2.15: Schematic illustrations of various cavity nucleation mechanisms: a) sliding leading to cavitation from ledges and triple points, b) cavity nucleation from vacancy condensation at high-stress region, c) cavity formation at the head of a dislocation pile-up and d) the formation of a cavity from a particle-obstacle in conjunction with the previous mechanisms [62].

Cavity nucleation by vacancy accumulation was suggested by Raj and Ashby [69]. It was suggested that the aggregation of vacancies at grain boundaries, particularly at triple points, can lead to formation of voids, as illustrated in Figure 2.15(b). However, the hypothesis of vacancy accumulation as the root of cavity nucleation was however refuted by other researchers, who attributed the formation of cavities to the applied stress. Argon *et al.* [70] proposed that only large threshold stresses can promote vacancy accumulation and subsequently nucleate cavities. The stresses required were however orders of magnitude larger than the observed stresses leading to failure, implying that cavity nucleation by vacancy accumulation is unlikely to

occur.

Nevertheless, it has been widely accepted that vacancy accumulation can occur at grain boundaries perpendicular to the tensile axis, due to dislocation pile-ups against hard particles [71–73]. Similar cavity nucleation can occur within the grains around hard particles, however the cavity growth rate is slower due to lower diffusion rates in the bulk. Grain boundary sliding (GBS) was also reported to result in stress concentration at grain boundaries, however it remains unclear whether the stress levels are sufficient for cavity nucleation [74].

Moreover, cavity nucleation has been associated with plastic deformation, where the high dislocation activity was correlated with cavity formation [75, 76]. In addition, Kassner *et al.* [77] observed cavity formation due to plasticity rather than diffusion at creep tests performed on high-purity Ag at about 0.25 T_m. High-angle grain boundaries containing obstacles were the dominant sites of cavity nucleation. By contrast, cavities were not observed on high-angle boundaries free of obstacles. Thus, it was suggested that the presence of obstacles, such as hard particles, at the grain boundaries is required for cavity nucleation.

Finally, it is worth mentioning another location susceptible to stress concentration; existing cavities and voids in the microstructure. The presence of cavities or voids in the initial microstructure, has been shown to stimulate locally the nucleation rates of cavities [78].

2.4.2 Cavity Growth

2.4.2.1 Diffusion controlled

At elevated temperatures, cavity growth depends predominantly on diffusion along the grain boundaries, whereas at lower temperatures cavity growth occurs due to plasticity. Hull and Rimmer [79] were the first to develop a theory to explain the growth of an isolated cavity when controlled by diffusion under an applied external stress, σ. Figure 2.16 illustrates the proposed theory, where λ_s is the cavity spacing, δ is the grain boundary thickness and a is the cavity radius [62].

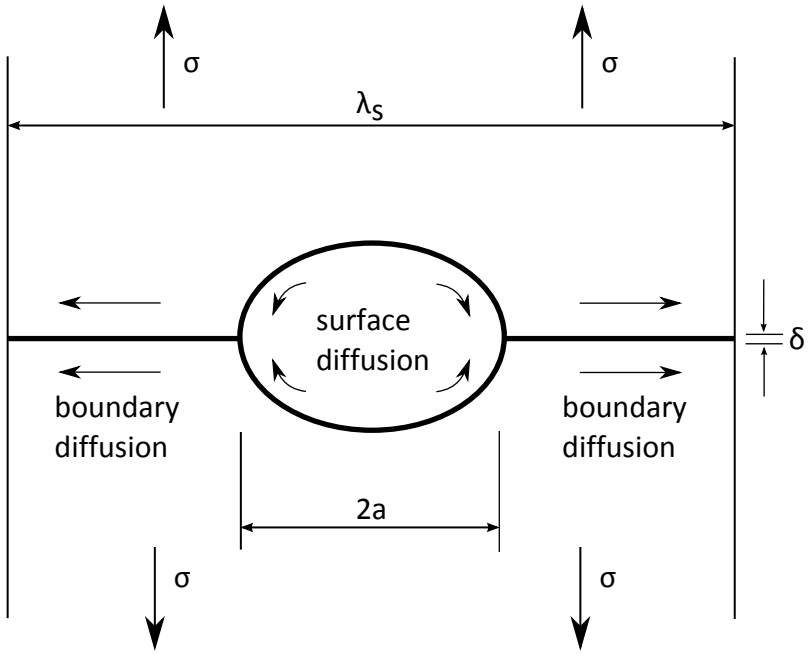


Figure 2.16: Cavity growth from diffusion across the cavity surface and through the grain boundaries [62].

Later, improved theories based on the Hull–Rimmer relationship were suggested by others researchers [69, 80, 81]. The main improvements take into account for instance the entire grain boundary as a vacancy source and non-spherical cavity

shape.

Chuang and Rice [82] and later Needleman and Rice [83] proposed that the cavity growth is controlled by surface rather than grain boundary diffusion. Their approach however lacked experimental evidence and most measurements are considered inconclusive. Furthermore, the suggested equation for the rate of cavity growth is not consistent with the Monkman-Grant relationship, where the cavity growth rate should be proportional to the stress to the fifth power rather than the third [62].

2.4.2.2 Coupled diffusion and plasticity controlled

A different approach was followed by other researchers regarding the cavity growth rate. Cocks and Ashby [84], Nix [85] and Needleman and Rice [83] suggested that cavity growth is affected by a phenomenon where diffusion and creep plasticity processes are coupled.

This coupled effect was expressed numerically firstly by Needleman and Rice [83], where a cavity growing substantially by grain boundary diffusion within a distance Λ, in a matrix which deforms by power law creep, was studied. Diffusion dominates the cavity growth within a distance Λ, whereas power law creep is predominant outside that region, as illustrated in Figure 2.17.

The presence of creep plasticity promotes the diffusive growth of cavities, since the length Λ over which grain boundary diffusion can dominate, is shortened. Very rapid growth of the cavity occurs at high stresses and strain rates because Λ decreases. In the case where Λ+a is less than the cavity spacing λ_s, diffusion-controlled growth does not exert any effect, whereas when Λ+a $\geq \lambda_s$, the cavity growth is substantially controlled by diffusion. In addition, it was suggested by Needleman and Rice that creep plasticity contributes to cavity only when $T > 0.5\,\mathrm{T}_m$ and

$\sigma/G > 10^{-3}$ for pure metals. On the other hand, Riedel [80] has stated that diffusion is the prevalent mechanism for cavity growth during the entire process of creep.

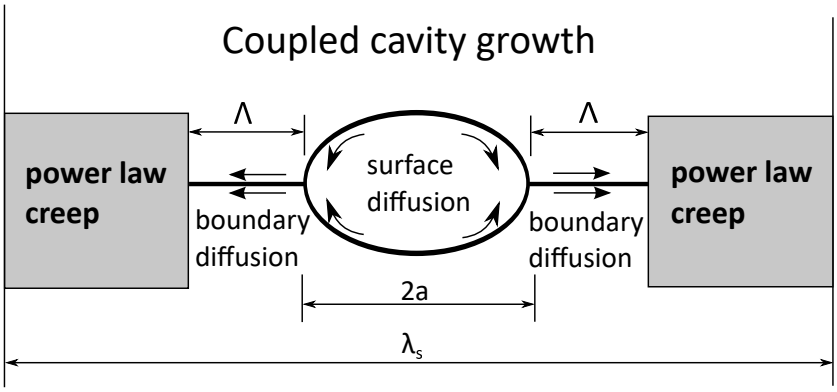


Figure 2.17: Schematic illustration of the model for coupled diffusive cavity growth with creep plasticity [85].

Chapter 3

Microstructural Characterisation Procedures

3.1 Introduction

This chapter describes the materials used in this research study and the processes followed for their production. In addition, the experimental methods utilised for the microstructural characterisation of these alloys are described in detail.

3.2 Materials

The effect of grain boundary elements on polycrystalline superalloys was the main focus of this study. Thus, two polycrystalline superalloys were used to investigate the effect of carbon and boron.

More specifically, in Chapters 4 and 5 particular attention was paid to study the effect of boron on a new polycrystalline superalloy called STAL15-CC. The chemical composition was chosen by Siemens Industrial Turbomachinery AB in Sweden by Dr Magnus Hasselqvist and it is a candidate polycrystalline superalloy for guide vanes and heat shields suitable for industrial gas turbines. Previously, the single crystal version of this composition was thoroughly studied [86].

The composition of the prototype nickel-based polycrystalline superalloy STAL15-CC investigated in this study is given in Table 3.1. The chemical analysis shown, was conducted in an independent laboratory where the carbon contents was measured using a LECO CS444 analyser and the other elements were measured by inductively coupled plasma - optical emission spectrometry (ICP-OES).

In order to investigate the effect of boron on the grain boundary character, test-bars were cast containing various amounts of boron. In particular, test-bars with no boron (boron free - BF), low boron (LB - 0.03 at.% B), medium boron (MB - 0.05 at.% B) and relatively high boron (HB - 0.08 at.% B) content were produced.

Table 3.1: Summary of chemical compositions of the different STAL15-CC variants investigated (at.%).

Alloy	**B**	**C**	**Co**	**Cr**	**Mo**	**W**	**Al**	**Ta**	**Hf**	**Si**
Boron Free	<0.005	0.44	5.50	16.45	0.61	1.26	10.00	2.41	0.02	0.08
Low Boron	0.03	0.47	5.60	16.43	0.58	1.27	10.11	2.41	0.02	0.06
Medium Boron	0.05	0.47	5.50	16.55	0.59	1.26	10.09	2.40	0.02	0.04
High Boron	0.08	0.53	5.53	16.64	0.60	1.21	10.01	2.43	0.02	0.08

Castings in the form of tapered rods were prepared at Doncasters Precision Castings Ltd., using casting stock melted by Ross & Catherall (Sheffield, United Kingdom). Conventional ceramic moulds were used, with additions of cobalt aluminate in the primary slurry in order to achieve the required grain size. The use of

cobalt aluminate as nucleation catalyst in nickel-based superalloys casting has been discussed in Chapter 2. The ceramic moulds were de-waxed in a steam furnace for 5 minutes and then sintered at 1000 °C for an hour, prior to casting. All the castings were performed under vacuum conditions, where the temperature of the moulds was approximately 1000 °C. Figure 3.1 illustrates the geometry of the mould.

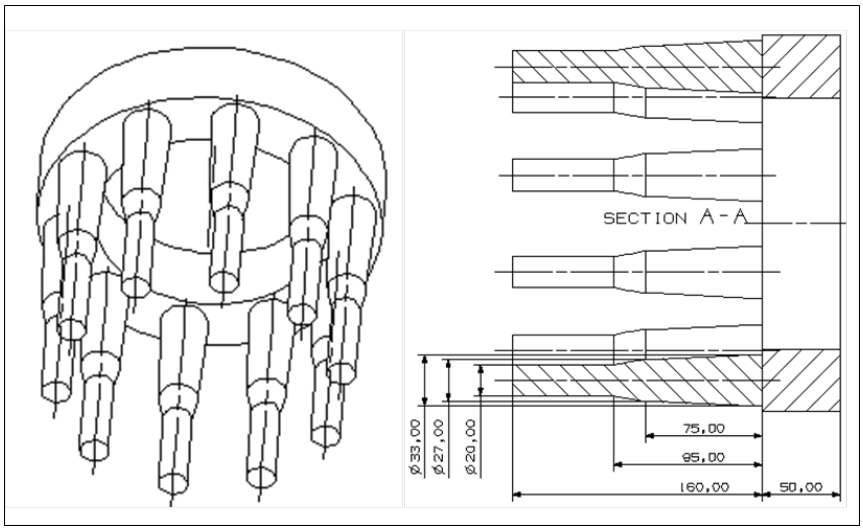


Figure 3.1: Geometry of the moulds used to cast STAL15-CC.

After conventional casting, a hot isostatic press was used to consolidate the as-cast bars, in order to eliminate microporosity and improve mechanical properties. The HIP process was performed at 1195 °C for 5 hours under 175 MPa pressure and it was conducted at the Department of Metallurgy and Materials, at the University of Birmingham. The process of HIP was followed by a stage of primary ageing at 1120 °C for 4 hours and a subsequent second stage of ageing at 845 °C for 24 hours, both followed by air-cooling. Thermodynamic calculations using Thermocalc coupled with the TTNI8 database indicated a γ' solvus temperature of 1148 °C and a solidus temperature of 1233 °C.

Finally, in Chapter 6 the polycrystalline IN792 nickel-based superalloy was used to investigate the effect of MC carbides on the thermal–mechanical fatigue (TMF) properties of superalloys. The chemical composition of the alloy IN792 investigated in this study has composition Ni–13.4Cr–8.5Co–1.1Mo–1.2W–7.3Al–4.7Ti–1.3Ta–0.4C–0.1B (at.%). The test material was delivered by Howmet as cast round bars with a diameter of 20 mm. After conventional casting the material was hot isostatically pressed at 1195 °C and 150 MPa for 2 hours followed by solution heat treatment at 1121 °C for 2 hours and then ageing at 850 °C for 24 hours.

3.3 Characterisation Methods

3.3.1 Scanning Electron Microscopy (SEM) – Energy Dispersive X-Ray (EDX)

SEM analysis of the cast nickel-based superalloys was performed using a field emission gun scanning electron microscope (FEG-SEM) JEOL 6500F. All the observations were made using the backscattered detector on flat polished specimens and working distance between 8-10 mm and a voltage of 10 kV. The specimens were mounted in conductive bakelite using a Kemet Metapress-A mounting press. They were mechanically ground up to 1200 grit paper and then polished with 9, 3 and 1 μm diamond suspension. The final step involved polishing with colloidal silica (0.04 μm). All samples were cleaned thoroughly in ultrasonic bath using acetone and ethanol.

The oxidised specimens investigated in Chapter 5 were directly mounted on a pin stub using silver epoxy. The oxide was observed using a dual column focused ion beam (FIB) microscope Zeiss NVision. First, a W-protective layer was deposited on the oxide and then trenches were made using the FIB. The oxide was imaged with

the specimen tilted at 54 °. That way, the specimen did not to be cold mounted and any potential damage of the scale from the polishing was minimised.

EDX spectroscopy analysis was also performed where necessary on polished specimens, using an Oxford Instruments EDX detector attached to a Zeiss Merlin FEG-SEM. The data was analysed using the Aztec software. The working distance was 8 mm and a voltage of 5 kV was used, in order to collect data from specimens containing oxides.

3.3.2 Electron Backscattered Diffraction (EBSD)

EBSD strain mapping analysis was performed on samples polished as mentioned above. The surface of the samples was plasma cleaned for 5 minutes prior to EBSD analysis. EBSD patterns were recorded using a 1000×1000 pixel, peltier cooled charge coupled device (CCD) camera at full resolution using a JEOL 6500F FEG-SEM, with intensities digitized using TSL/EDAX OIM DC 5.3 software for subsequent off-line batch-wise analysis. The scintillator screen was held at a capture angle of 70 ° to the sample surface. The SEM conditions used were 20 keV beam energy, and a beam current of ~ 14 nA, for which exposure time was about 0.5 s, gain usually -8.20 and black -7.50. All maps were obtained using a 50 nm step size and the reference pattern was collected from each individual grain; no theoretical pattern was used for the strain mapping analysis. For every analysis 20 regions of interest (ROI) were used and the elastic constant of nickel was used for the γ/γ' microstructure. The elastic constant of the MC carbides is not known therefore some of the strain map figures in Chapters 5 and 6 consist of blank regions. The same settings were used for all the performed strain maps and the inverse pole figure maps included in this study.

3.3.3 Transmission Electron Microscopy (TEM)

TEM analysis was performed using a JEOL 2000FX W-filament and a JEOL 2100 LaB_6 TEMs. Specimens from the grain boundary regions of fully heat treated bulk samples were prepared by liftout using a FIB microscope (FEI FIB 200 and Zeiss NVision FIB). First, the bulk samples were polished as described above and then in order to reveal the grain boundary particles, the samples were etched using the Kalling's No. 2 solution (5 gr $CuCl_2$, 100 ml HCl, 100 ml Ethanol). The FIB was used to mill trenches and lift the specimens using a micromanipulator onto Cu half grids. The specimens were then thinned using very low currents (100 pA) to minimise Ga contamination. The final thickness of the specimens was measured in the FIB to be ~ 80 nm.

Micrographs were obtained using bright-field imaging. Diffraction patterns (DP) were collected, however very often the particles present in the microstructure were too small to use the smallest selected area aperture. Therefore, convergent beam diffraction had to be performed using the smallest spot sizes, which, when converged, allowed diffraction patterns to be taken from microstructural features as small as ~ 40 nm. The aim was to produce images of the microstructures and diffraction patterns to confirm their crystallography. DPs were indexed using the JEMS software.

3.3.4 Secondary Ion Mass Spectrometry (NanoSIMS)

NanoSIMS analysis was performed using the CAMECA NanoSIMS 50 instrument for the three boron-containing STAL15-CC alloys. Samples from fully heat treated bars were cut having a geometry of $7\,\text{mm} \times 7\,\text{mm} \times 4\,\text{mm}$ thickness and they were

carefully polished as described earlier. Prior to analysis the specimens were cleaned in ultrasonic bath using ethanol. In addition, indents were made on the surface of the samples using a macro-hardness instrument. The indents were used as fiducial marks in order to be able to identify the grain boundaries during the analysis. Therefore prior to NanoSIMS analysis pictures of the surface of the samples were taken using an optical microscope.

A 16 keV Cs^+ primary ion beam was used to sputter ions from the sample surface with a beam current of 1.6-1.9 pA. Prior to each measurement, the surface was cleaned with a high-current (6-10 nA) primary ion beam to implant Cs and achieve a high ion yield. The instrument was aligned to detect the ion species $^{12}C^-$, $^{11}B^{12}C^-$, $^{11}B^{16}O_2^-$ and $^{52}Cr^{16}O^-$, with particular care taken to avoid isobaric interferences by turning on boron and chromium standards. The $^{11}B^{16}O_2^-$ signal was chosen in preference to the $^{11}B^-$ and $^{11}B^{16}O^-$signals because it gives the highest signal intensity [87, 88]. Image processing was carried out using ImageJ software (U.S. National Institutes of Health, Bethesda, MD) using the OpenMIMS plugin (National Resource for Imaging Mass Spectometry, Harvard University, Cambridge, MA).

3.3.5 Atom Probe Tomography (APT)

Atom probe tomography was performed on grain boundary particles using the Cameca LEAP 3000X HR instrument operating in laser mode with pulse rate at 200 kHz, pulse energy 0.4 nJ and temperature 50 K. Site-specific specimens were prepared from samples which were polished and etched in order to reveal the grain boundary particles. In addition, APT analysis of oxides was performed using the Cameca LEAP 5000 XR instrument operating in laser mode with pulse rate at 100 kHz, pulse

energy 50 pJ and temperature 50 K.

The stages for the lift-out process were same as described in Reference [89]. In particular, Figure 3.2 illustrates the main stages followed for the preparation of APT samples for this study. The first stage includes the deposition of a W protective layer along the grain boundary (Figure 3.2(a)) in order to avoid any Ga contamination. Then, side trenches were milled at an angle 30 ° from normal to the surface. With the help of an *in-situ* micro-manipulator, a thin cantilever of material is extracted from the bulk sample. The manipulator is welded on the material using W (Figure 3.2(b)). Once that stage is successfully completed, then the manipulator is used to transfer the bar across to the support system, which constitutes from Cameca Si flat posts as illustrated in Figure 3.2(c). The bar is welded on the posts with W and and small slices were cut using the FIB (Figure 3.2(d)). Finally, two stages of annular milling were performed in order to produce an APT tip with a diameter smaller than 100 nm, as illustrated in Figures 3.2(e) and 3.2(f). For the second annular milling, low-kV was used in order to reduce Ga implantation. Finally, a low voltage cleaning stage was performed if the W protective layer was not removed after the second annular milling.

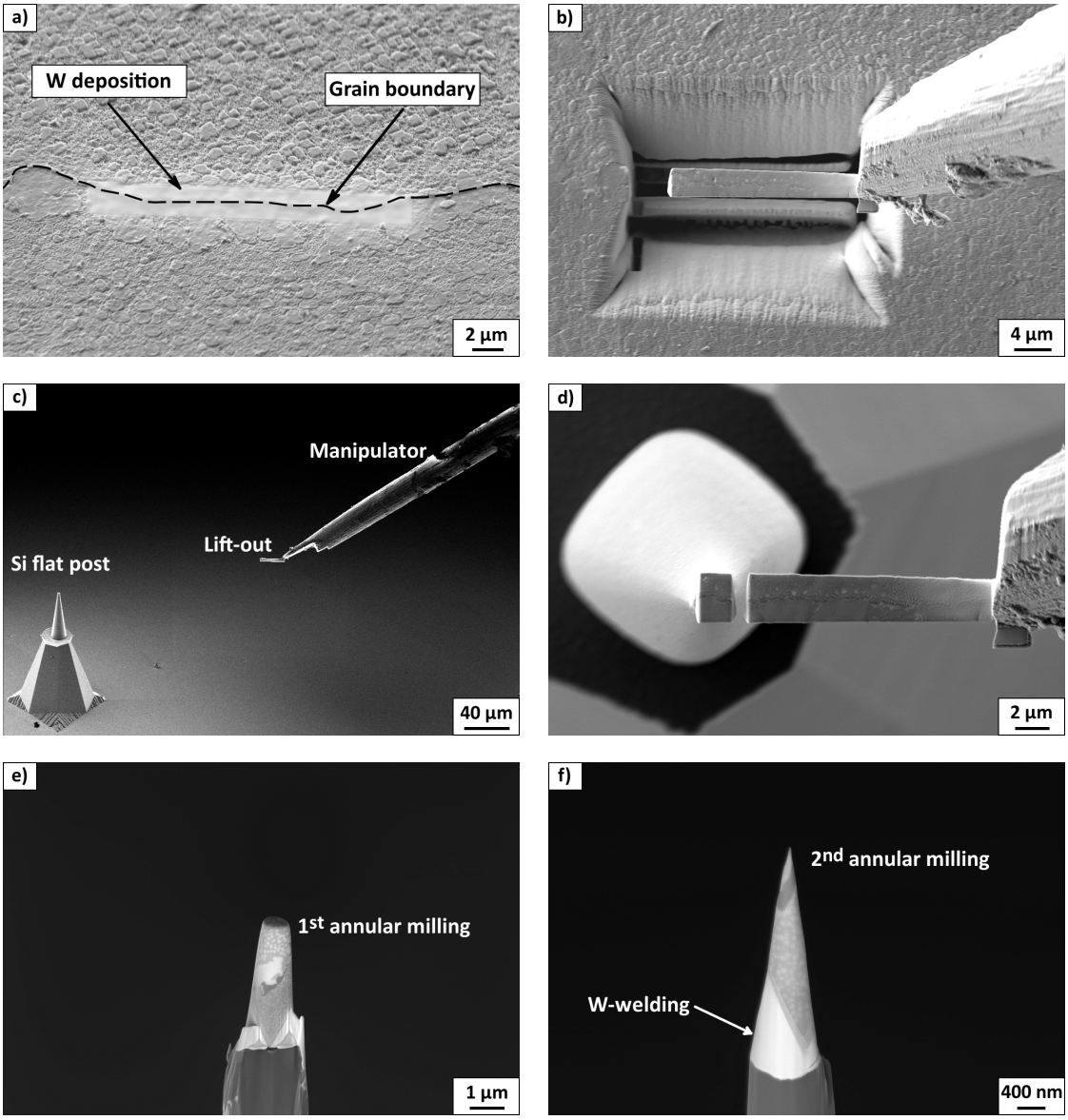


Figure 3.2: Secondary SEM images showing the stages of the lift-out process and APT sample preparation: a) W protective layer is deposited on area of interest, b) side trenches milled at an angle 30 ° from normal to the surface, c) transfer of bar to supportive Si flat posts, d) welding of bar Si flat post and cut of slice from the bar, e) first annular milling and f) second annular milling.

Chapter 4

The Effect of Boron on Grain Boundary Character in a New Polycrystalline Superalloy

4.1 Introduction

Boron is added to the nickel-based superalloys, in small quantities and has the significant effect of improving the mechanical properties of these materials, in particular creep performance [20, 39, 90]. Boron acts a grain boundary strengthening element; it is well known that it prefers to reside at the grain boundaries on account of its different atomic size and electronic properties [91, 92]. But one cannot be satisfied with this explanation. Some important questions exist concerning this so-called boron effect, which deserve consideration.

For instance, in what state does boron reside at the grain boundaries? As elemental segregation or as a second phase? If the latter, which phase is prevalent? How much boron is necessary to impart optimised performance, and why? How do the properties vary around the optimum concentration? What happens if the boron is removed entirely? Moreover, these alloys contain a number of different phases other than the matrix γ, for instance the strengthening phase γ' as well as carbides as such MC and $M_{23}C_6$ which can also lie on the grain boundaries. Therefore, at which of the different interfaces is boron preferentially located?

Answers to these questions are needed to promote fundamental understanding of the boron effect. The principal overarching issue is one of better characterisation; systematic experimentation at high resolution is required. Here, complementary analytical techniques, specifically atom probe tomography, transmission electron microscopy and high resolution secondary ion mass spectroscopy, are used to study the boron distribution in a new experimental single crystal superalloy [86]. Using four variants, including one which is boron free, has provided new insights to begin to resolve some of the issues identified above.

4.2 Background

The role of boron in superalloy metallurgy is contentious. Various conflicting reasons have been put forward for its beneficial effects. Among them, the most popular include an increase in boundary strength and cohesivity [45,93]. For instance, Briant and Messmer [94,95] have emphasised the effect of chemical bonding on grain boundary embrittlement; thus when an impurity element resides at the grain boundary, it can be expected to alter locally the chemical bonding on the basis of a differing electronegativity. Such effects will draw charge from the metal atoms onto the impurity,

and as a consequence less charge is available to participate in the local metal-metal bonding. Thus embrittlement occurs. Elements such boron do not draw charge from the metal atoms but rather form covalent bonds, and hence cohesion might be increased at grain boundaries. In general, the more electronegative the impurity element with respect to the metal solvent, the greater the amount of embrittlement expected [94, 95].

Boron has also been implicated in microstructural modifications of grain boundary character. For example, it has been proposed that minor additions of boron are advantageous to creep life and creep ductility by decreasing the agglomeration of $M_{23}C_6$ at the grain boundaries during protracted loading at temperature [7, 8, 93, 96, 97]. It has been proposed that continuous layers of $M_{23}C_6$ along the grain boundaries serves as a crack initiation site, presumably on the basis of the brittleness of this phase. It has been argued that boron may play a role in the transfer of slip from one plastically deforming grain to neighbouring ones, but without substantive proof [98]. In addition, boron has been found to segregate to the γ/γ' interface at grain boundaries, presumably due to its size and its low solubility in those phases [44]. Moreover, it can combine with elements such as chromium or molybdenum to form borides; however their precise composition and crystallography remain in doubt [93, 99].

Moreover, it has been suggested that any strong interaction between boron atoms and dislocation cores might impede dislocation motion and hence increase resistance to fatigue cracking [100]. Indeed, a mechanism by which the grain boundary dislocation motion is encouraged by boron has been proposed [41]. It is well known that grain boundaries serve as obstacles to dislocation movement, creating dislocation pileups in the vicinity of grain boundaries. This results in strain concentration, initiation of micro-cracks and eventually to premature failure. Therefore, it has been

suggested that some elements, for instance boron, may not improve the strength of the material, but on the contrary, soften it by facilitating grain boundary dislocation movement. Finally, it has been claimed that the segregation of boron may fill vacancies at grain boundaries, thus decreasing the grain boundary diffusivity. It is known that at high temperatures and low stresses cracks initiate at the boundaries due to diffusional phenomena [29]. As a consequence, as the grain boundary diffusivity decreases, the rate of void formation might be expected to decrease and simultaneously the occurrence of γ' denuded zones retarded, thus improving creep properties [93].

Note that each of the above mechanisms requires the presence of boron at grain boundaries. However, at this stage it is not clear whether the improved grain boundary strength can be ascribed to boron being segregated along the grain boundaries or alternatively incorporated into borides and/or carbides. Table 4.1 summarises available studies on the effect of boron in different superalloys [43, 46–48, 101–112]. Although one must take care in drawing conclusions particularly due to the well-known difficulty in characterising and quantifying boron levels, the most common observation finds boron to be segregated at grain boundaries, followed by studies supporting the presence of intergranular borides. In other studies, both segregation of boron and precipitation of borides have been observed, whereas the least common observation is the presence of boron in carbides such as MC and $M_{23}C_6$. What is clear is that application of high resolution characterisation techniques will aid in the rationalisation of the boron effect.

Reference	Year	Alloy	Boron, at.%	Solid solution	Boride	Carbide
Tytko [47]	2012	617B	0.02	Yes	No	Yes
Hong [101]	2012	Alloy 263	0.015	Yes	No	No
Alam [102]	2012	(718) WE971/G727	0.059/0.064	Yes	No	No
Yan [46]	2008	Experimental	0.10	No	Yes	Yes
Zhang [103]	2008	Rene80	0.065	No	Yes	No
Zhang [104]	2008	IN738	0.060	No	Yes	No
Ojo and Zhang [43]	2008	Rene80	0.065	No	Yes	No
Lemarchand [105]	2002	N18	0.083	Yes	No	No
Cadel [106]	2002	N18	0.083	No	Yes	No
Chen [23]	1998	IN718 -Low/High boron	0.006/0.023	Yes	No	No
Huang [108]	1997	IN718	0.016	Yes	No	No
Blavette [109]	1996	Astroloy	0.11	Yes	Yes	Yes
Letellier [110]	1994	Astroloy	0.11	Yes	No	No
Letellier [111]	1993	Astroloy	0.11	Yes	No	No
Buchon [112]	1991	NA4	0.09	Yes	No	No
Delargy [48]	1983	IN939	0.05	No	No	Yes

Table 4.1: Summary of published studies of boron-containing superalloys, in which boron is claimed to be present either (i) in elemental form at grain boundaries, or (ii) as a boride.

4.3 Experimental Procedures

High-resolution characterisation analysis was conducted for a boron-free and three boron-containing variants of STAL15-CC. The boron-containing alloys were called low boron (LB - 0.03 at.% B), medium boron (MB - 0.05 at.% B) and relatively high boron (HB - 0.08 at.% B). Grain boundaries after full heat-treatment were characterised using SEM, APT, TEM and NanoSIMS. The material and the microstructural characterisation methods used in this study were described in detail in Chapter 3. In addition, Thermo-Calc (database TTNI8) and DICTRA (database MOBNI3) were used for equilibrium phase calculations and kinetics, respectively. The software and corresponding databases were provided by Thermo-Calc Software AB, Stockholm, Sweden.

4.4 Results

4.4.1 Observations on Grain Boundary Morphology by Electron Microscopy

Using a backscattered detector, SEM images with a strong dependence on the average atomic number Z were obtained. Backscattered SEM images showing the microstructure of fully heat treated boron free, low, medium and high boron alloys are given in Figure 4.1. Careful examination of the contrast variations in these microstructures reveals the precipitation of γ' particles and various types of carbides and the presence of what will identified below as grain boundary borides in the boron containing alloys.

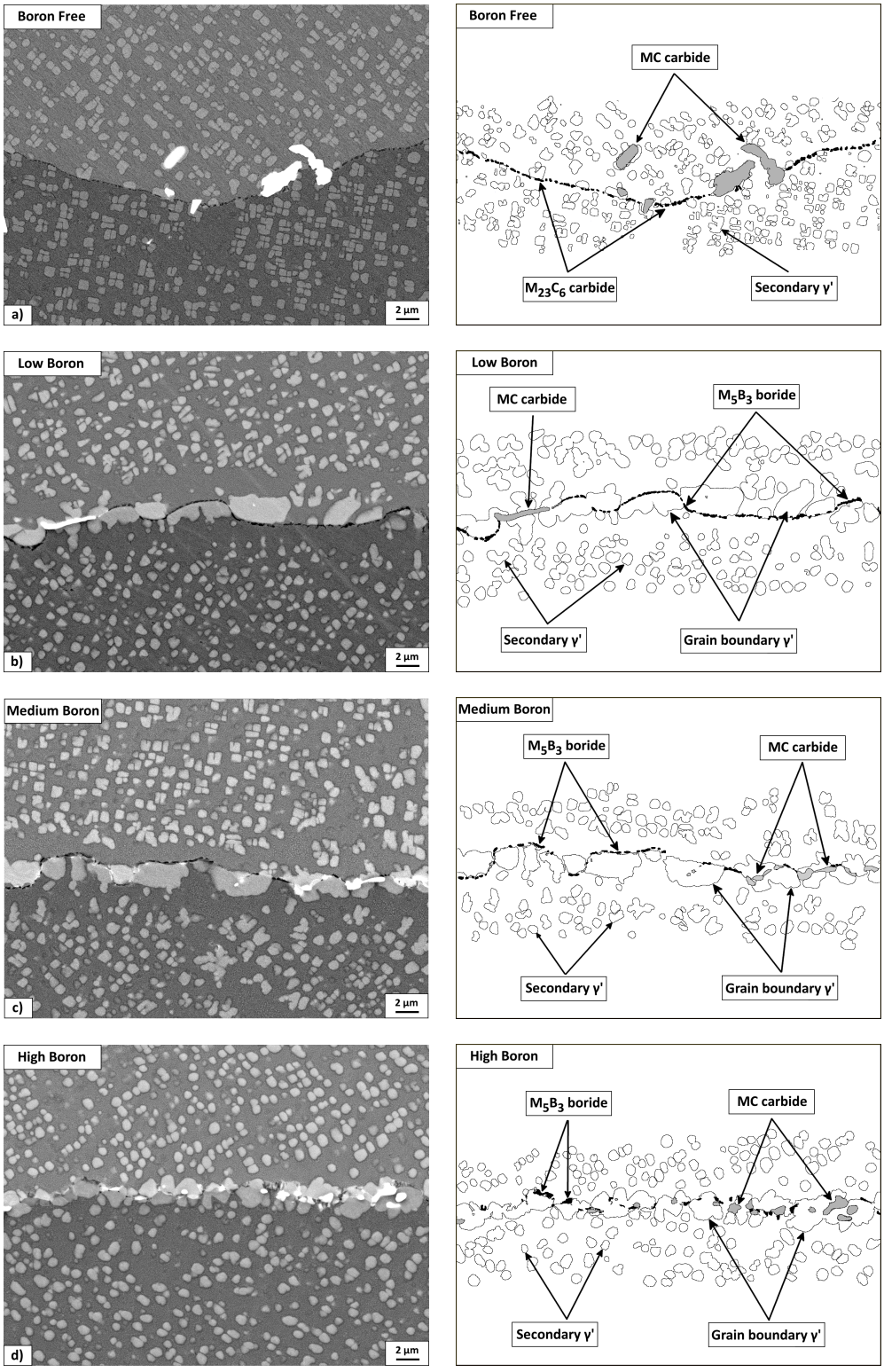


Figure 4.1: Backscattered SEM images of fully heat microstructures of: a) boron-free, b) low boron, c) medium boron and d) high boron alloys alongside corresponding descriptive schematic illustrations.

Combined SEM and TEM analyses confirmed the precipitation of inter- and intragranular carbides for all the investigated superalloys. These particles exhibit the brightest Z contrast in the backscattered images and have a cubic structure which corresponds to MC-type carbides; a TEM micrograph of a typical grain boundary MC carbide is given in Figure 4.2. The high Z contrast implies the partitioning of heavy elements such as Ta and W. The MC carbides were found to precipitate at the grain boundaries, exhibiting an elongated or blocky morphology. By contrast, intragranular MC carbides have mainly script-like shapes and the occurrence of blocky carbides is less likely. The shape and morphology of the MC carbides were not found to be affected by the boron additions.

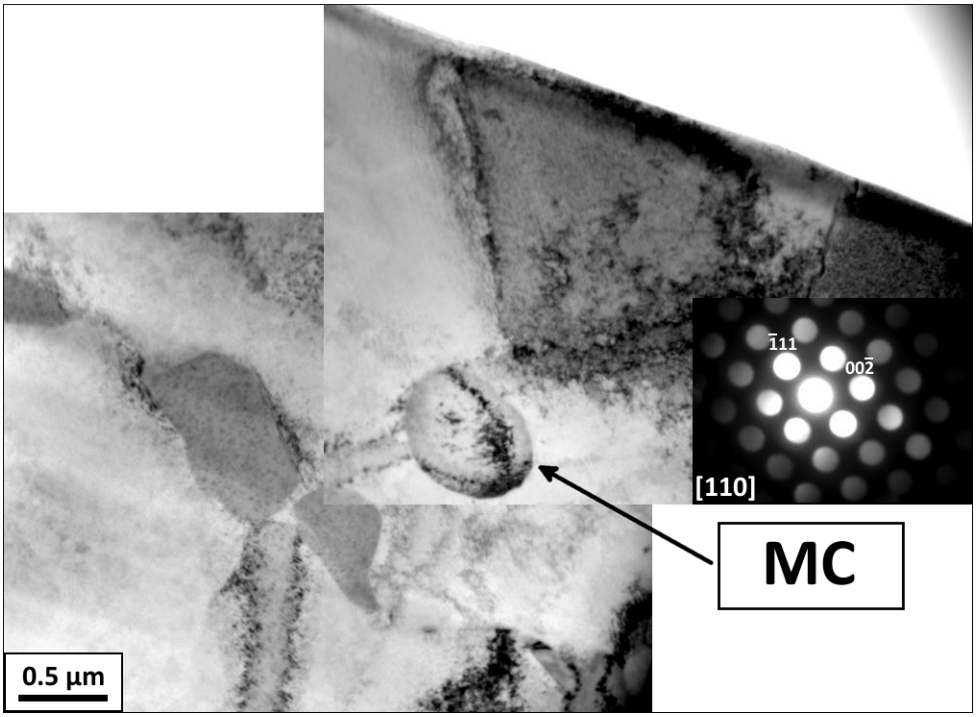


Figure 4.2: TEM micrograph of fully heat treated microstructure from a grain boundary region of high boron alloy showing an intergranular MC carbide.

Moreover, the backscattered images revealed the precipitation of particles along the grain boundaries which exhibit the lowest Z contrast, suggesting the partitioning

of light elements such as carbon and boron. In the case of the boron-free alloy these particles correspond to $M_{23}C_6$-type carbides. However in the boron-containing alloys these particles have a tetragonal structure which corresponds to M_5B_3-type boride. A large number of particles in different boron-doped samples were analysed by TEM without identifying any intergranular $M_{23}C_6$ carbides. The TEM image and corresponding diffraction pattern from a typical grain boundary region of a boron-containing alloy are presented in Figure 4.3.

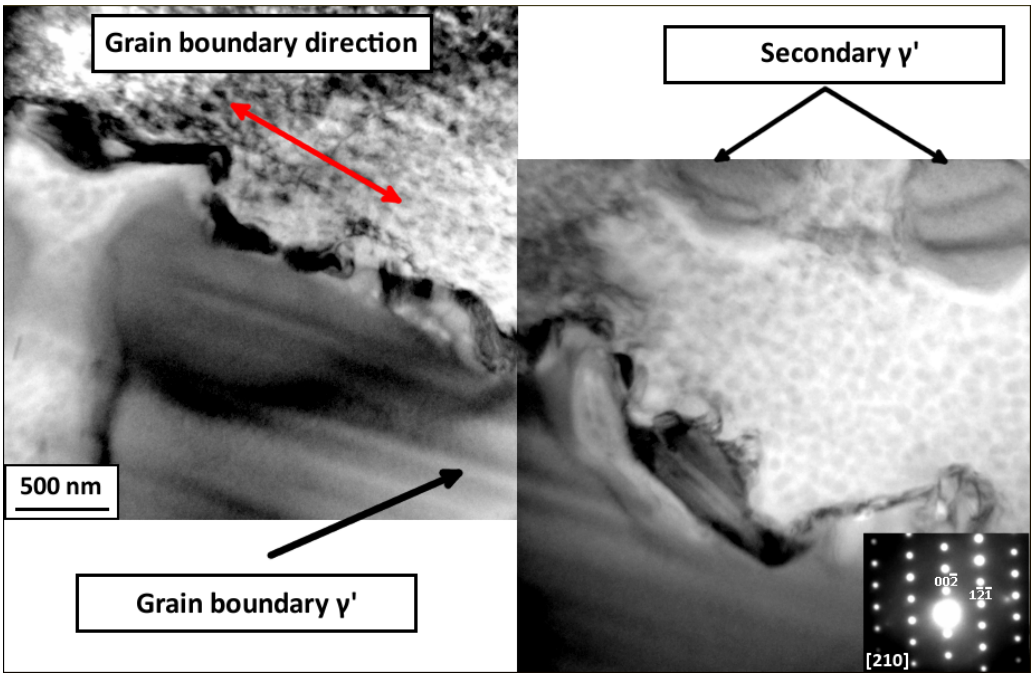


Figure 4.3: TEM micrograph of fully heat treated microstructure from a grain boundary region of the medium boron alloy. Representative M_5B_3 borides along the grain boundary and grain boundary γ' are illustrated. The grain boundary direction is denoted by the red arrow.

Although no $M_{23}C_6$ carbides were found at the grain boundaries of the boron-containing alloys, nano-sized $M_{23}C_6$ carbides were observed at the vicinity of grain boundaries of boron-containing alloys. TEM analysis revealed that these $M_{23}C_6$ carbides are coherent with the γ matrix, as illustrated in Figure 4.4. They exhibit a

plate-shaped morphology and they are up to 200 nm in length and 30 nm in thickness. In addition, they are randomly distributed close to grain boundaries but their presence is not continuous. Similar morphology of $M_{23}C_6$ carbides was not observed in the boron-free alloy.

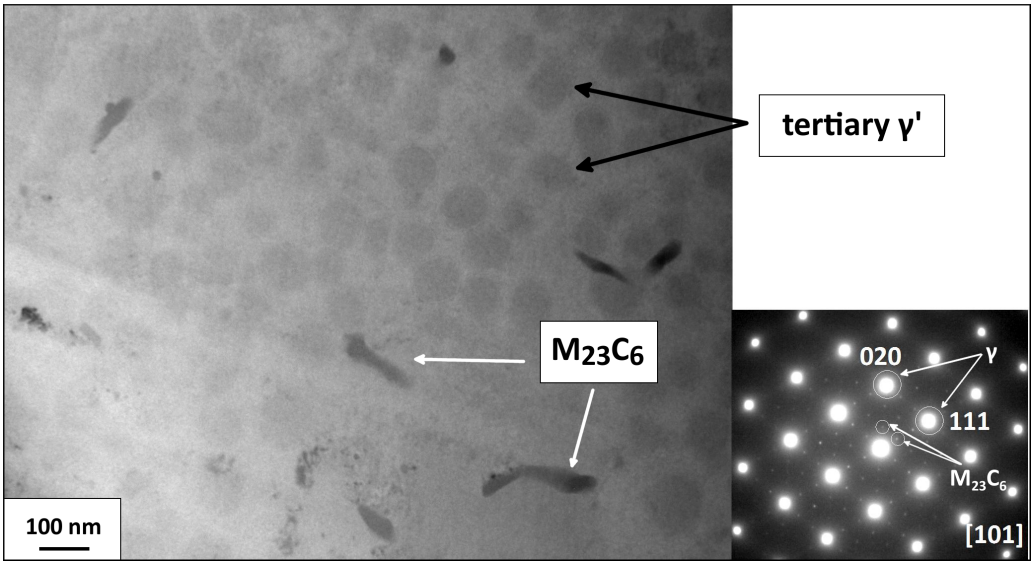


Figure 4.4: TEM micrograph of fully heat treated microstructure of the high boron alloy. Representative $M_{23}C_6$ carbides and tertiary γ' in the γ matrix are illustrated.

Finally, the breakdown of MC carbides particularly in the vicinity of grain boundaries in the boron containing alloys led to the formation of γ' particles close to grain boundaries. They exhibit a relatively larger size compared to secondary γ' particles precipitated in the grain interiors. At grain boundaries decorated mostly by borides, these γ' occur as large discrete particles in the vicinity of boundaries (Figure 4.1(b)). However, when the MC carbides dominate along the boundaries, the grain boundary γ' particles can form nearly continuous layers along the grain boundaries, as illustrated in Figure 4.1(d)). It is believed that rupture life and ductility can be improved by enveloping the brittle grain boundary carbides and therefore retarding crack initiation at high temperatures [6]. Excessive grain boundary γ' layers are not

observed in the boron free alloy.

4.4.2 Analysis by Atom Probe Tomography

Atom probe tomography (APT) was utilised to investigate in detail the concentrations of carbon and boron in the grain boundary particles. Lift-out samples for atom probe analysis were selected carefully from grain boundary regions for all four different alloys, as illustrated in Figure 4.5. The process followed for the lift-out and specimen preparation is described in [89]. The selected grain boundaries contain both the carbides and borides, as identified in the SEM and TEM investigations.

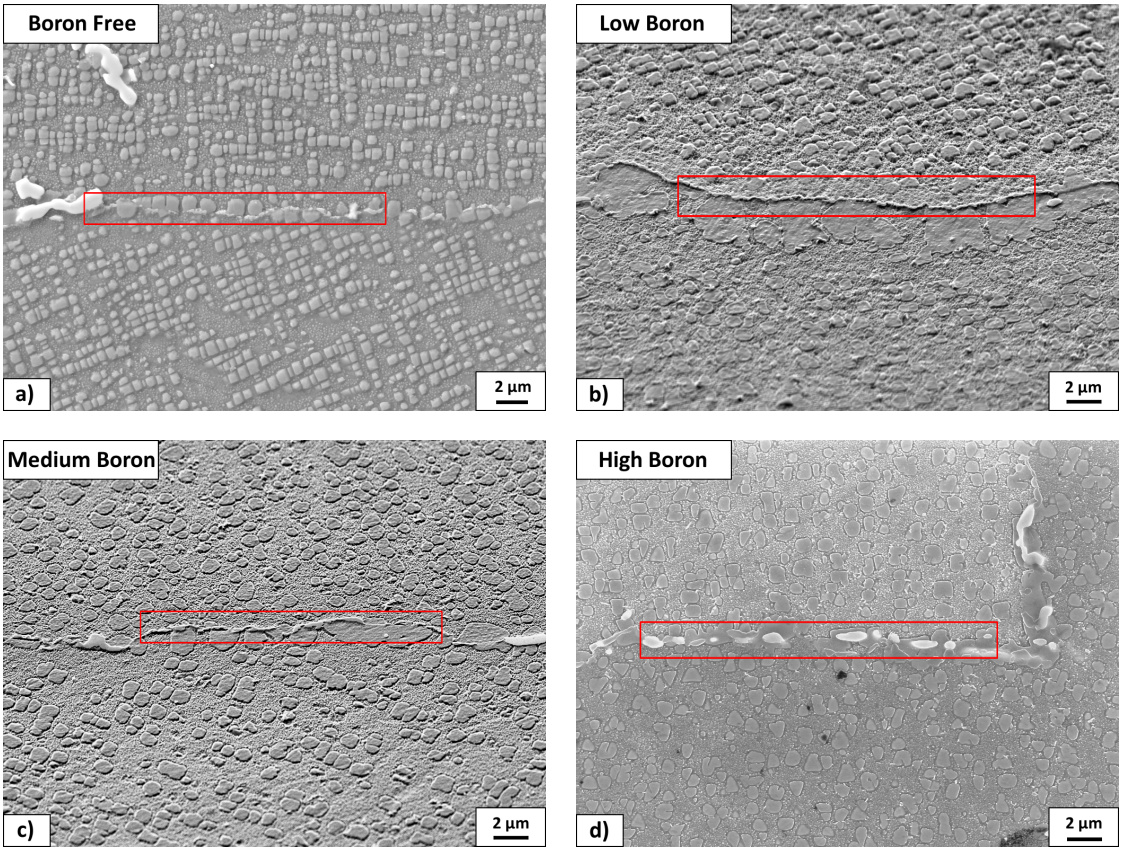


Figure 4.5: Selected grain boundary regions of fully heat treated microstructures of: a) boron free, b) low boron, c) medium boron and d) high boron alloys for atom probe tomography.

Table 4.2 summarises the compositions of the carbides and borides as obtained by APT analysis. In order to cover all the investigated interfaces, data for the $M_{23}C_6$ carbide from the boron free alloy are presented, since this type of carbide was observed only at this alloy. The MC carbide dataset comes from a boron containing alloy and its chemistry is representative for the boron-doped alloys. Finally, representative borides from boron containing alloys are presented and discussed. As one of the main focal points of this Chapter is the presence of borides in superalloys, more than one dataset containing borides collected from different boron-containing alloys are presented.

Table 4.2: Chemical composition of carbides and borides as measured by atom probe tomography (at.%).

	$M_{23}C_6$	MC	M_5B_3	M_5B_3
B	0.5 ± 0.01	0.3 ± 0.02	36.2 ± 0.17	36.6 ± 0.14
C	19.7 ± 0.02	49.6 ± 0.18	0.0	0.2 ± 0.02
Cr	70.4 ± 0.04	0.4 ± 0.02	60.6 ± 0.17	57.9 ± 0.14
Mo	2.5 ± 0.02	0.2 ± 0.02	1.1 ± 0.04	2.3 ± 0.04
Co	1.3 ± 0.01	0.2 ± 0.02	0.5 ± 0.02	0.5 ± 0.02
Ta	0.0	48.3 ± 0.18	0.0	0.0
Ni	3.6 ± 0.02	0.7 ± 0.03	0.1 ± 0.02	0.3 ± 0.02
Al	0.0	0.0	0.0	0.0
W	2.0 ± 0.01	0.2 ± 0.02	1.4 ± 0.04	2.2 ± 0.04

Figure 4.6 is representative of the grain boundary area atom probe reconstruction from the boron-free alloy, from which information about the composition of individual γ, γ' and $M_{23}C_6$ phases can be extracted. The $M_{23}C_6$ carbides were found to be enriched in chromium, whereas other elements such Mo, W and Ni contribute in much lower percentages, as given in Table 4.2. The stoichiometry of the Cr-rich carbide corresponds to $M_{23}C_6$. In addition, a small amount of boron (0.5 at.% B) was measured in these $M_{23}C_6$ particles and its presence is ascribed to impurities in the melt stock.

The grain boundary contained within this reconstruction is at the $\gamma/M_{23}C_6$ interface. Proximity histograms, which are elemental composition profiles measured as a function of distance from the $\gamma/M_{23}C_6$ interface are presented in Figure 4.9(a). A carbon enrichment at the interface of width approximately 3 nm was observed, indicating that carbon not only participates in the formation of carbides at grain boundaries but also occurs as segregent to particular interfaces. No enrichment of any other element at the $\gamma/M_{23}C_6$ interface was observed by atom probe tomography for the boron free alloy.

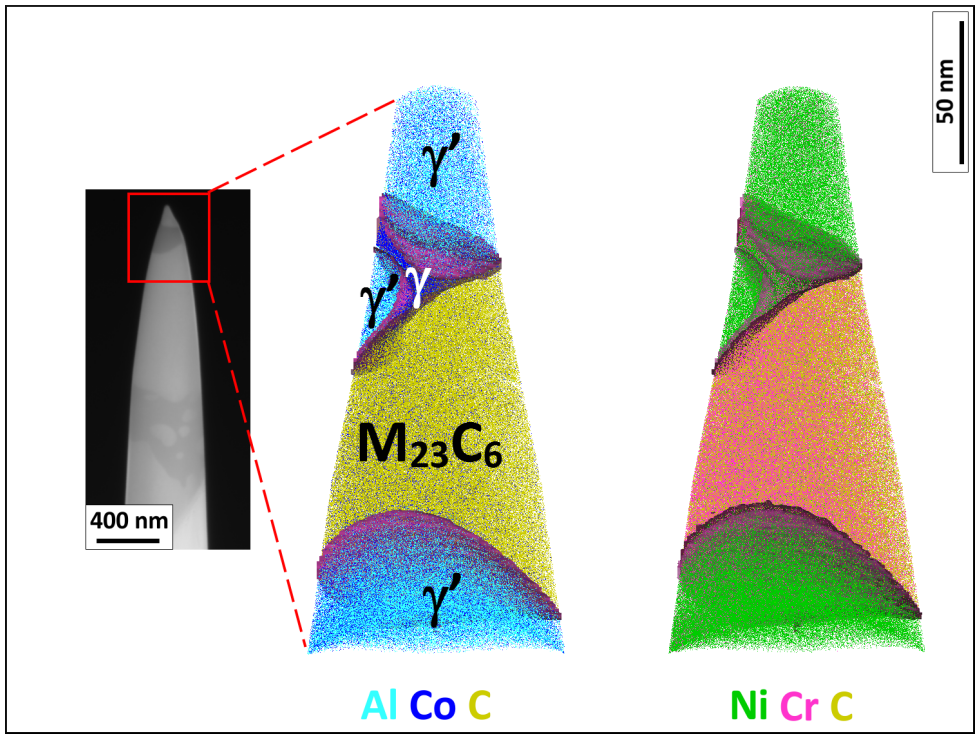


Figure 4.6: SEM micrograph of atom probe tip obtained from fully heat treated grain boundary of the boron free alloy alongside atom probe reconstruction.

Atom probe samples were also analysed in order to obtain the composition of the intergranular MC carbides. Figure 4.7 is an atom probe reconstruction containing an MC carbide, γ and γ' phases collected from a boron containing alloy. The carbide

was found to be Ta-rich and its stoichiometry corresponds to MC-type carbides, confirming the TEM results. Here the grain boundary interface corresponds to both γ'/MC and γ/MC interfaces and their proximity histograms are depicted in Figures 4.9(b) and 4.9(c), respectively. No significant carbon enrichment, as observed for the $\gamma/M_{23}C_6$ interface in 4.9(a), was found at either interface. However, aluminium segregation was observed to the γ'/MC interface and to a lesser extent to the γ/MC interface. In addition, chromium enrichment occurred at the γ/MC interface. No boron enrichment was observed at the MC/γ' and MC/γ interfaces.

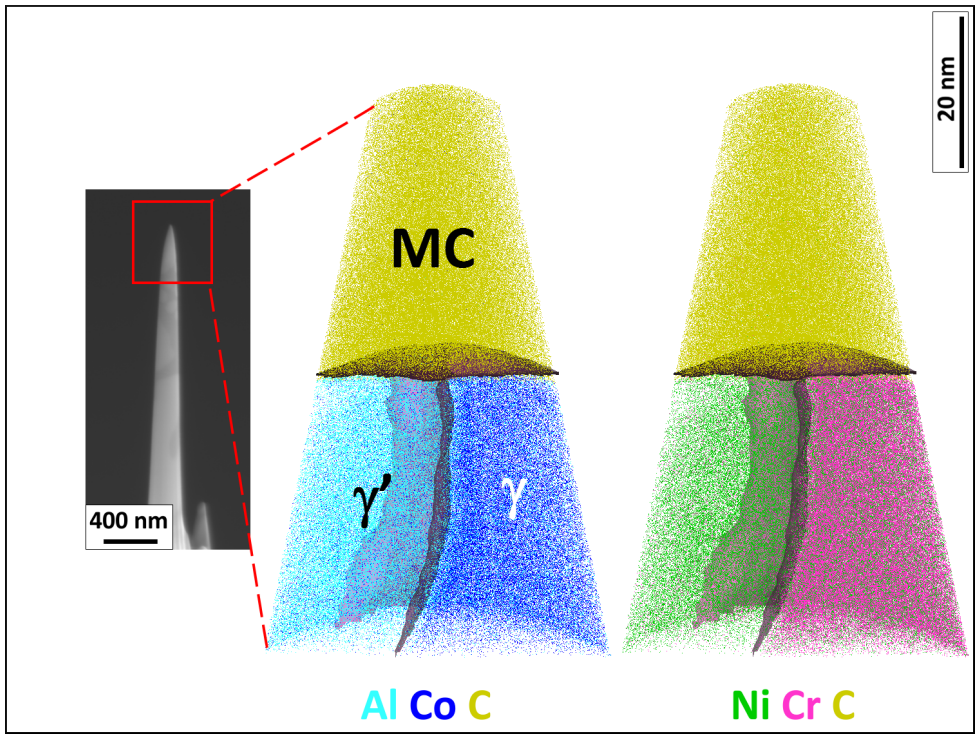


Figure 4.7: SEM micrograph of atom probe tip obtained from fully heat treated grain boundary of the high boron alloy alongside atom probe reconstruction.

The SEM and TEM investigations revealed the precipitation of borides along the grain boundaries of the boron-containing alloys. Figures 4.8(a) and 4.8(b) illustrate two representative APT analyses of the grain boundary region where these

borides were identified. It was found that these borides are mainly enriched in chromium, and their stoichiometry corresponds to M_5B_3 borides, as it can be seen in Table 4.2; in excellent agreement with the TEM findings. In addition, minor amounts of Mo and W were found within the borides, and a very small amount of carbon was observed in one of the detected borides.

In both these APT reconstructions (4.8(a) and 4.8(b)) the grain boundary lies at the γ'/M_5B_3 interfaces. Composition profiles across these γ'/M_5B_3 interfaces revealed a zone approximately 3 nm wide enriched in boron, as illustrated in Figures 4.9(d) and 4.9(e). Similar behaviour for boron was not observed for any other interface, including γ/γ' and γ/M_5B_3. For instance, composition profiles across the γ/M_5B_3 interface are illustrated in Figure 4.9(f). Besides the boron enrichment, higher concentrations of cobalt were found at the γ'/M_5B_3 interface in both reconstructions. In addition, from Figures 4.9(d) and 4.9(e) it can be noticed that there is no carbon segregation at the grain boundary interface in either reconstructions; this will be explained in detail in the discussion section.

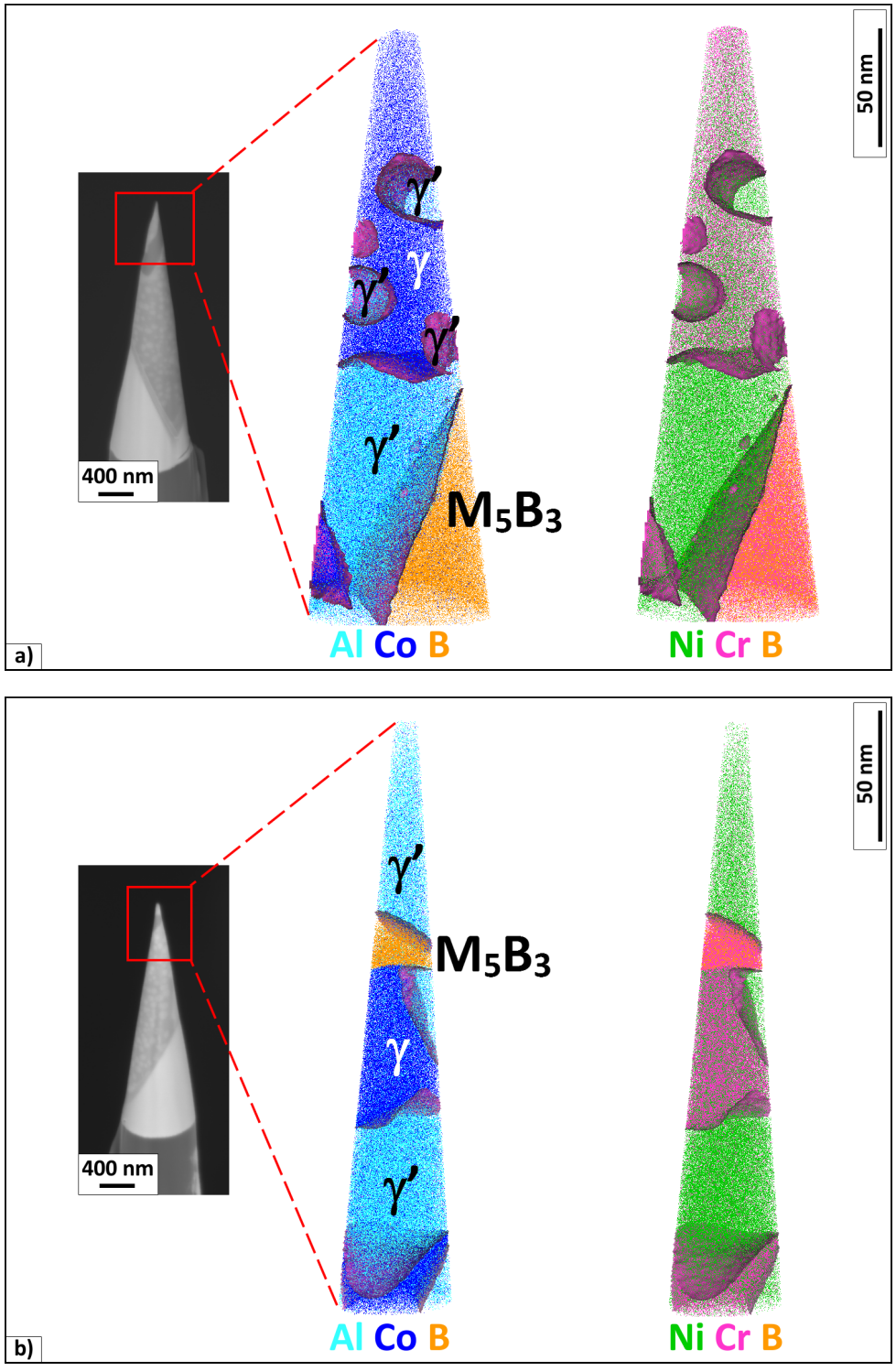


Figure 4.8: SEM micrographs of atom probe tips obtained from fully heat treated grain boundaries of: a) low boron and b) medium boron alloys alongside atom probe reconstructions.

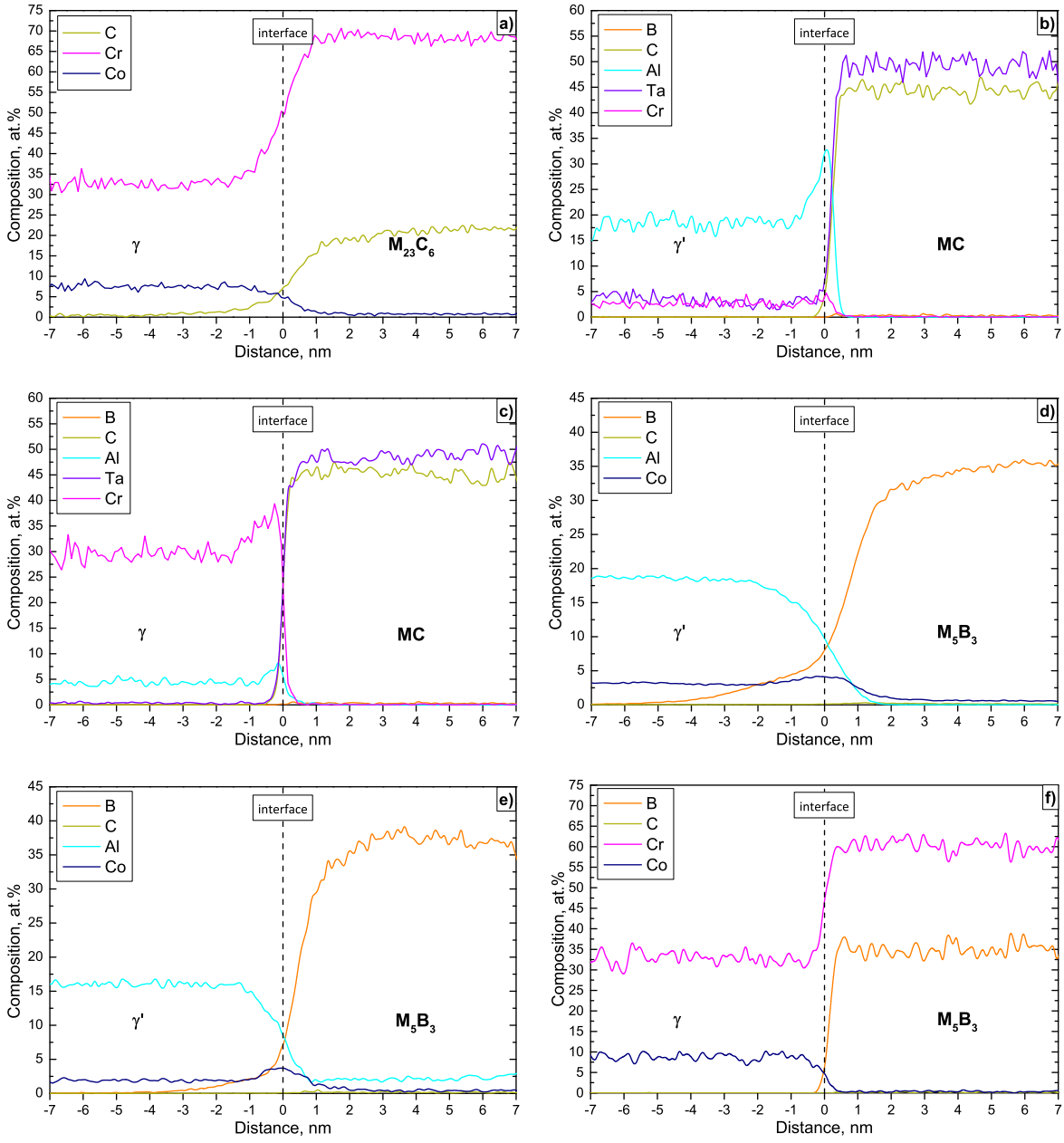


Figure 4.9: Concentration profiles analysis across grain boundary interfaces collected from atom probe tomography: a) concentration of C, Cr and Co at $\gamma/M_{23}C_6$ interface from the boron free alloy (data in Figure 4.6), b) and c) concentration of B, C, Al, Ta and Cr at MC/γ' and MC/γ interface from the high boron alloy (data in Figure 4.7), d) concentration of B, C, Al and Co at γ'/M_5B_3 interface from the low boron alloy (data in Figure 4.8(a)), e) concentration of B, C, Al and Co at γ'/M_5B_3 interface from the medium boron alloy (data in Figure 4.8(b)) and f) concentration of B, C, Cr and Co at γ/M_5B_3 interface from the medium boron alloy (data in Figure 4.8(b)). Error less than 0.05 at.%.

4.4.3 NanoSIMS Analysis

The above results confirm that significant quantities of boron exist in the form of borides at the grain boundaries. However, significant questions remain. First, is the location of all the boron explained in this way, or does the matrix contain some dissolved boron? Second, can quantitative data be acquired about the size and distribution of the grain boundary borides? To answer these questions, NanoSIMS analysis has been utilised, because this technique provides complementary capabilities, including analytical sensitivity – which is important for boron analysis at low concentrations – over larger volume of material compared to that can be studied by APT.

Figure 4.10 presents NanoSIMS elemental maps for the boron-containing alloys. The partitioning of boron into Cr-rich borides along the grain boundaries is clearly apparent. We did not detect boron in solid solution in the matrix or segregated at grain boundaries in any of the investigated boron-containing alloys. Line-scans across the borides in these NanoSIMS elemental maps show concurrent partitioning of chromium, boron and small concentrations of carbon, in excellent agreement with the atom probe datasets, as shown in Figure 4.11.

Moreover, much of the carbon detected was found to be tied up by Ta and contributes to the formation of MC carbides. In particular, strong carbon signals were found from both intergranular blocky and elongated and script-type intragranular Ta-rich MC carbides. As discussed for boron above, segregation of carbon at the grain boundaries was not observed. Finally, backscattered SEM images of the areas scanned by the NanoSIMS grain boundaries are shown in Figure 4.12, corresponding to the locations denoted by the red boxes in Figure 4.10. These images allow direct one-to-one correlation of the contrast levels in the BSE images with the chemical

maps in the NanoSIMS. The darkest contrast is thus clearly from the fine boride particles along the grain boundary.

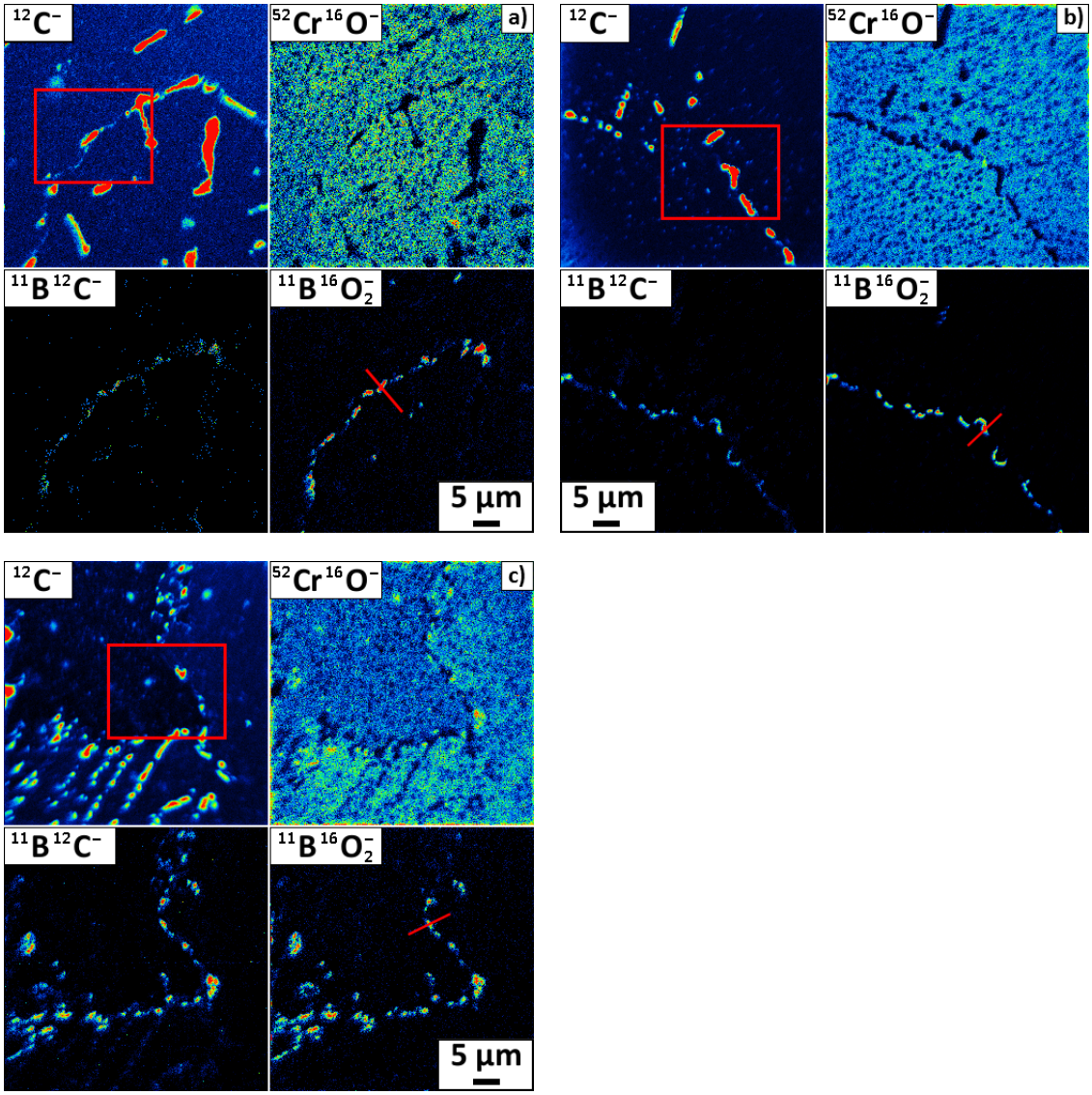


Figure 4.10: NanoSIMS images showing partitioning of C and B at intra- and intergranular carbides and intergranular borides in fully heat treated microstructures of: a) low boron b) medium boron and c) high boron alloys. Red boxes indicate the location of subsequent SEM imaging and red lines indicate the position and direction of the line scans.

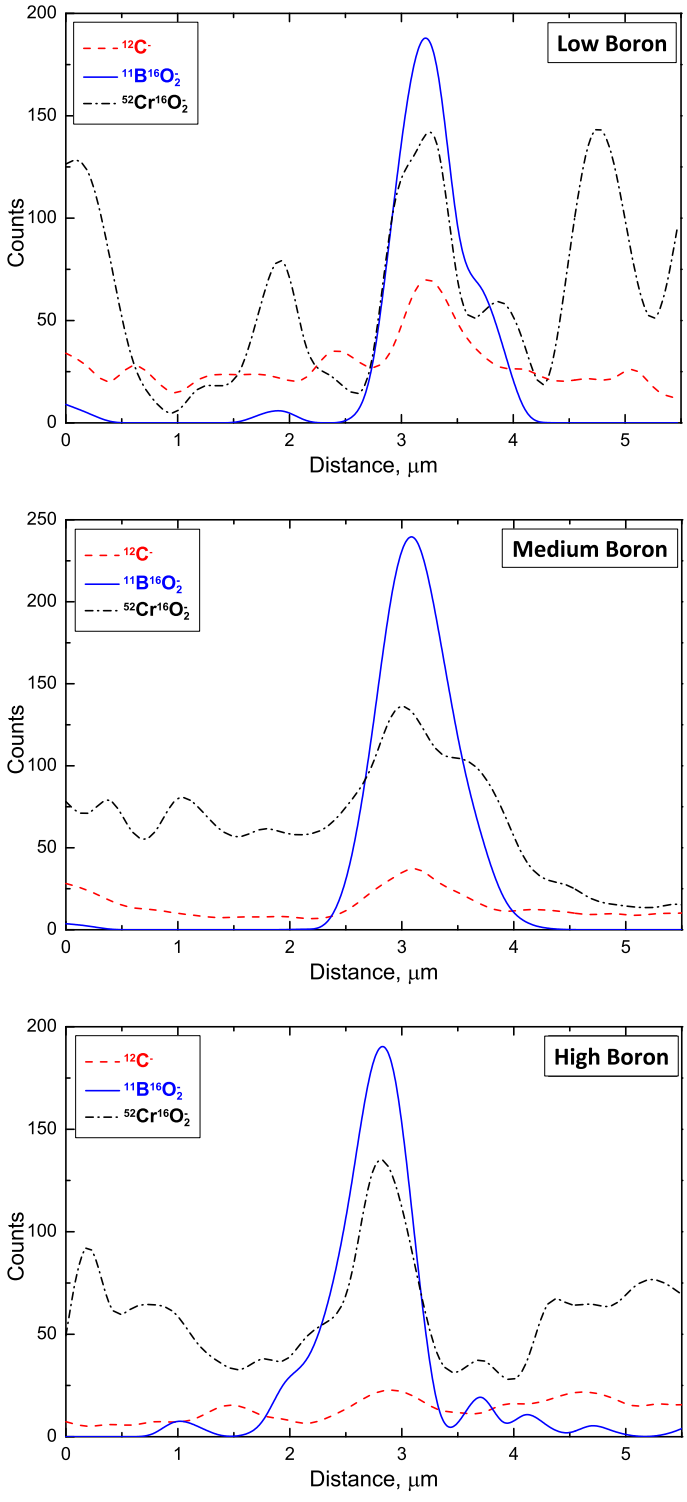


Figure 4.11: Line-scans across the grain boundaries as labelled in the NanoSIMS maps (see Figure 4.10), confirming the precipitation of Cr-rich borides.

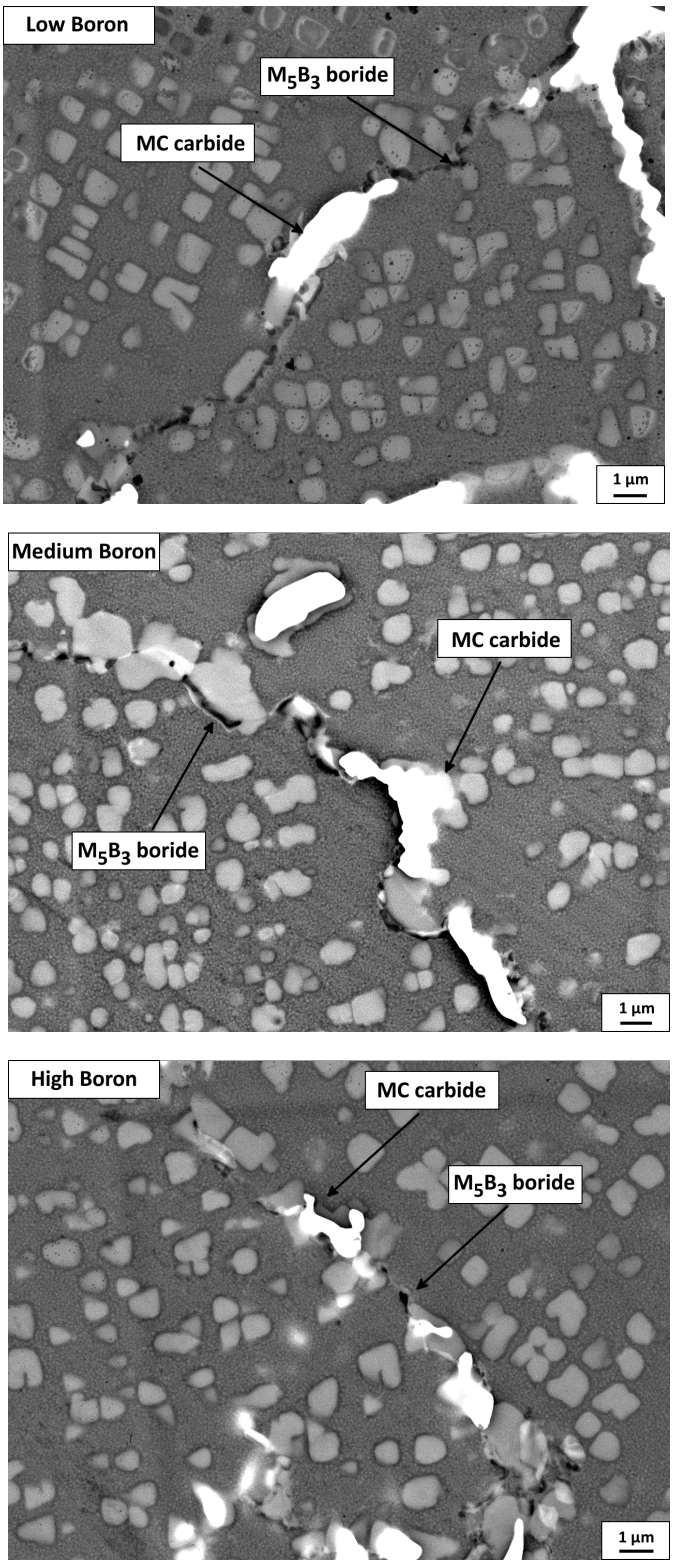


Figure 4.12: Backscattered SEM images from areas investigated by NanoSIMS. Images correspond to the red boxes in Figure 4.10.

4.5 Discussion

4.5.1 Grain Boundary Character

The results presented here demonstrate conclusively that additions of boron alter substantially the grain boundary character, in terms of which particular grain boundary phases form, of polycrystalline superalloys such as STAL15-CC. A boron addition as little as 0.03 at.% promotes the formation of intergranular M_5B_3 borides at the expense of $M_{23}C_6$ carbides. Thus, above this threshold the precipitation of borides arises at the grain boundaries; below it the $M_{23}C_6$ carbide is preferred.

The atom probe tomography results demonstrate that, even below the threshold level and even in a nominally boron-free variant, trace levels of boron can substitute for carbon in the $M_{23}C_6$, as confirmed in Table 4.2. Moreover, a thorough investigation of the $\gamma/M_{23}C_6$ interface revealed co-segregation of boron with carbon, as shown in the proximity graph in Figure 4.13. Such boron enrichment at the $\gamma/M_{23}C_6$ interface has been observed previously by atom probe tomography in a different nickel-based superalloy [47].

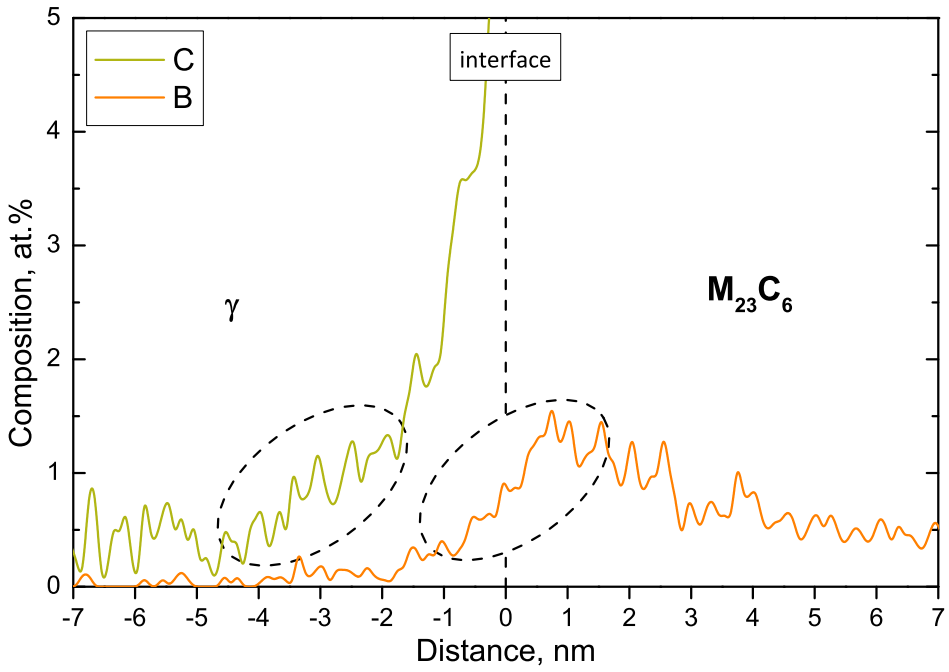


Figure 4.13: Concentration profiles analysis across the $\gamma/M_{23}C_6$ interface from the boron-free alloy collected by atom probe tomography (see Figure 4.6). Dashed ellipses indicate the carbon and boron enrichment. Error less than 0.05 at.%.

Moreover, the NanoSIMS results indicate that very little if any boron is found within the grains away from the grain boundaries. Thus one can expect the extent of precipitation of borides at grain boundaries to be controlled not just by the boron content but also by the average grain size. One can be quantitative about this by estimating the boride thickness expected at the grain boundaries as a function of grain size and mean boron content, on the assumption of its uniform and consistent decoration of them. The results are given in Figure 4.14. It can be seen that for a given boron content the thickness of the boride increases as the grain size increases, consistent with a decrease in the grain boundary area. The calculations recover reasonable estimates of the boride thickness normal to the grain boundary. For example, for a total boron content of 0.05 at.% corresponding to the medium boron variant studied here and a grain size of approximately 750 μm the boride thickness

is $\sim 50\,\mathrm{nm}$.

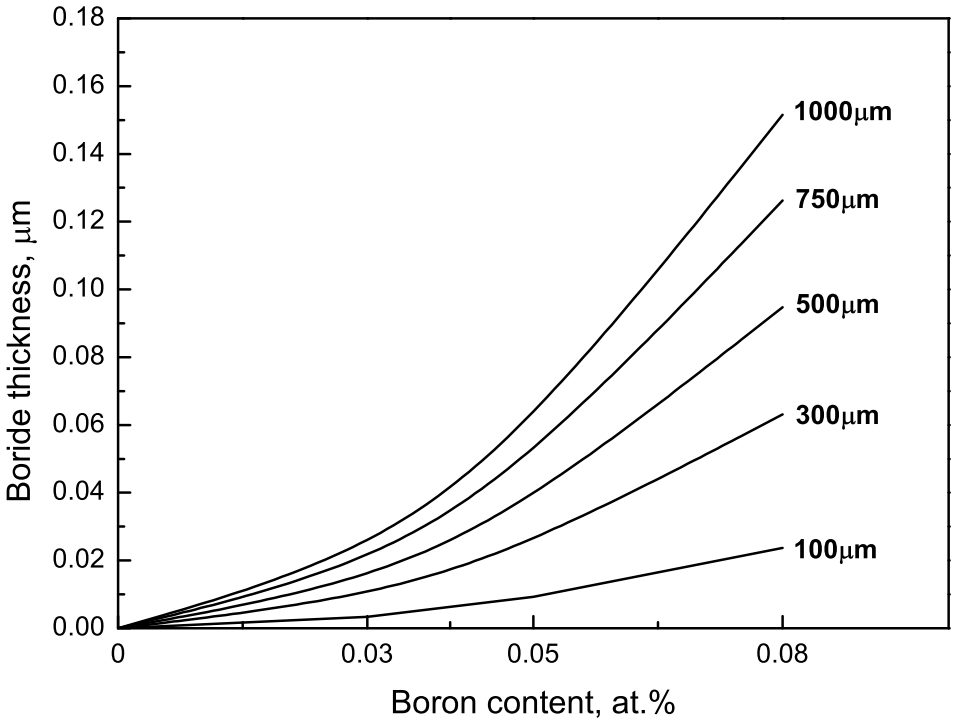


Figure 4.14: Calculated thickness of borides as function of average grain size and boron content.

It is interesting to compare these findings with observations reported in the literature. Figure 4.15 illustrates the results of a literature search of published data on a range of superalloys plotted as boron *vs.* chromium content, and indicating for each individual alloy the state claimed for boron either as in solid solution or as borides. Of course, a degree of subjectivity is introduced via the interpretation needed of the literature. Nevertheless, a relationship between the chromium and boron contents is found by plotting contour lines for different values of the solubility product, k, where $k = \frac{\alpha_{Cr_5B_3}}{[Cr]^5[B]^3}$ and $\alpha_{Cr_5B_3}$ is the chemical potential of Cr_5B_3. It can be seen that during the design of new superalloys, for a given Cr level, the boron content can be carefully selected in order to either promote the precipitation

of borides or keep the boron in solid solution at grain boundaries. Whilst there is not precise agreement with the available experimental data, a suitable value of k can be found which delimits these two situations.

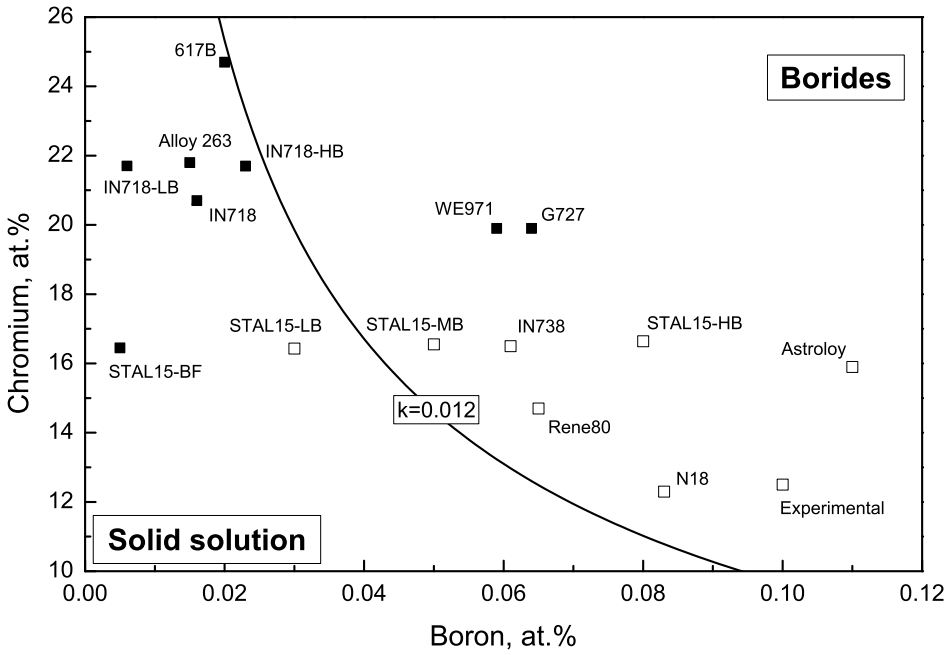


Figure 4.15: A summary of superalloys plotted in a boron *vs.* chromium graph indicating for each alloy whether the boron is in the form of solid solution (denoted by solid-filled squares) or solid solution and borides (denoted by empty squares).

Finally, the discrete MC carbides which are usually located at grain boundaries, form directly from the liquid during solidification at temperatures higher than those at which borides start forming. In this case, a nearly continuous γ' layer subsequently forms due to MC decomposition, as illustrated in Figure 4.1(d). The role of this complex morphology on the mechanical properties is controversial. On the one hand, it is believed that when the brittle MC carbides are enveloped within γ' layers, creep ductility and fracture toughness are improved. On the other hand, excessive precipitation of these layers can be catastrophic for the mechanical properties, since they serve as stress concentration sites at grain boundaries [6]. The effect of the γ'

layers at the grain boundaries is investigated in Chapter 5.

4.5.2 On the Importance of Grain Boundary Character on Creep Response

It is important to put the experimental findings into perspective by considering the influence of the grain boundary character on mechanical behaviour. To do this, a number of creep tests at different temperatures and stresses were designed, in order to correlate the optimal boron content with the best creep performance for this superalloy. Creep specimens were machined from fully heat-treated bars of STAL15-CC, with a gauge length 25 mm and a gauge diameter 5 mm. Preliminary results are illustrated in Figure 4.16; the constant load creep performance for all the investigated alloys at 750 °C/455 MPa is shown.

These results confirm that the modification to the grain boundary structure *via* alloying with boron is crucial in conferring the necessary high temperature mechanical properties in this alloying system. Figure 4.17 shows the fracture surfaces of the boron free and medium boron alloys. In the boron free case, intergranular creep failure is dominant (Figure 4.17(a)), whereas in the medium boron alloy there are strong indications of a mixed inter- and transgranular failure mechanism (Figure 4.17(b)). The transition from totally intergranular to mixed inter- and transgranular failure between boron free and medium medium boron alloys implies a dramatic enhancement of grain boundary strength.

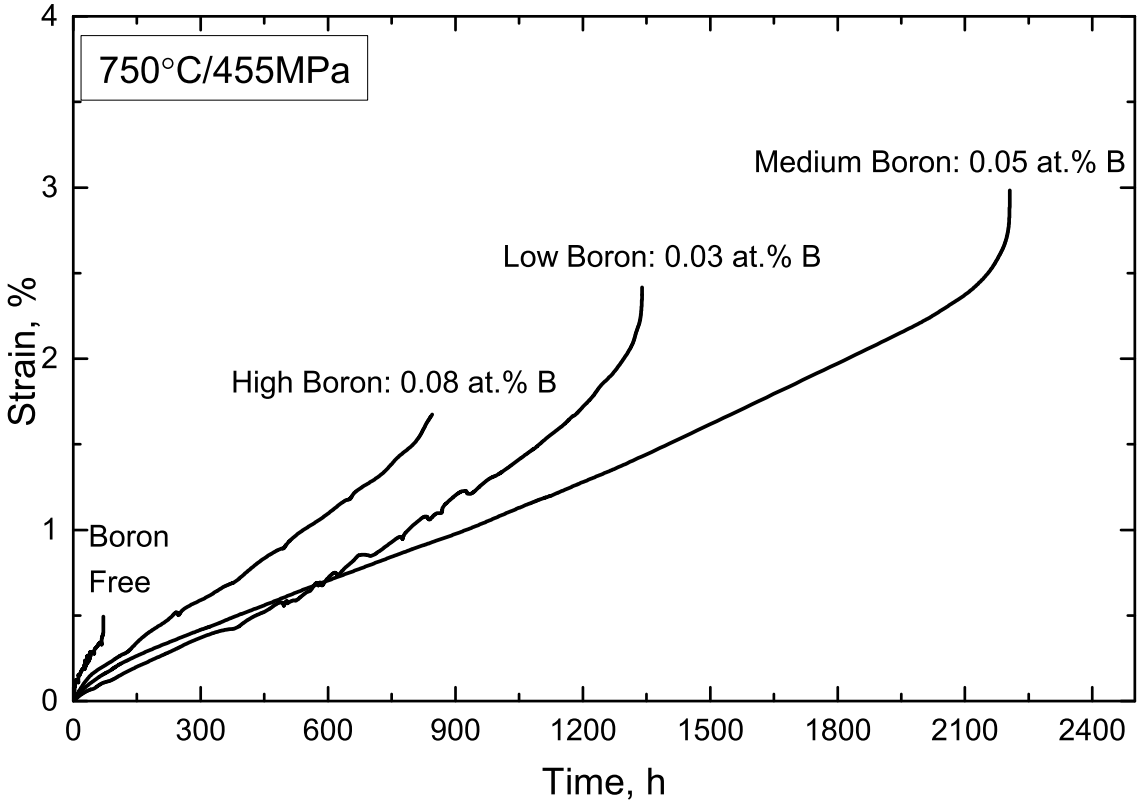


Figure 4.16: Creep strain *vs.* time curve for the investigated alloys.

Moreover, Figure 4.18 illustrates secondary cracks from sections cut parallel to stress axis of the boron free and medium boron alloys. In the boron free alloy, the grain boundary exhibits a non-serrated character. Thus, voids on the incoherent interface interlink and form a continuous crack path as illustrated in Figure 4.18(a). By contrast, for the medium boron alloy a rather serrated grain boundary character is observed as compared to the boron free case. As a consequence, continuous voids along the grain boundaries are eliminated and creep performance is enhanced, see Figure 4.18(b). The role of boron on grain boundary serration is discussed in detail in Chapter 5.

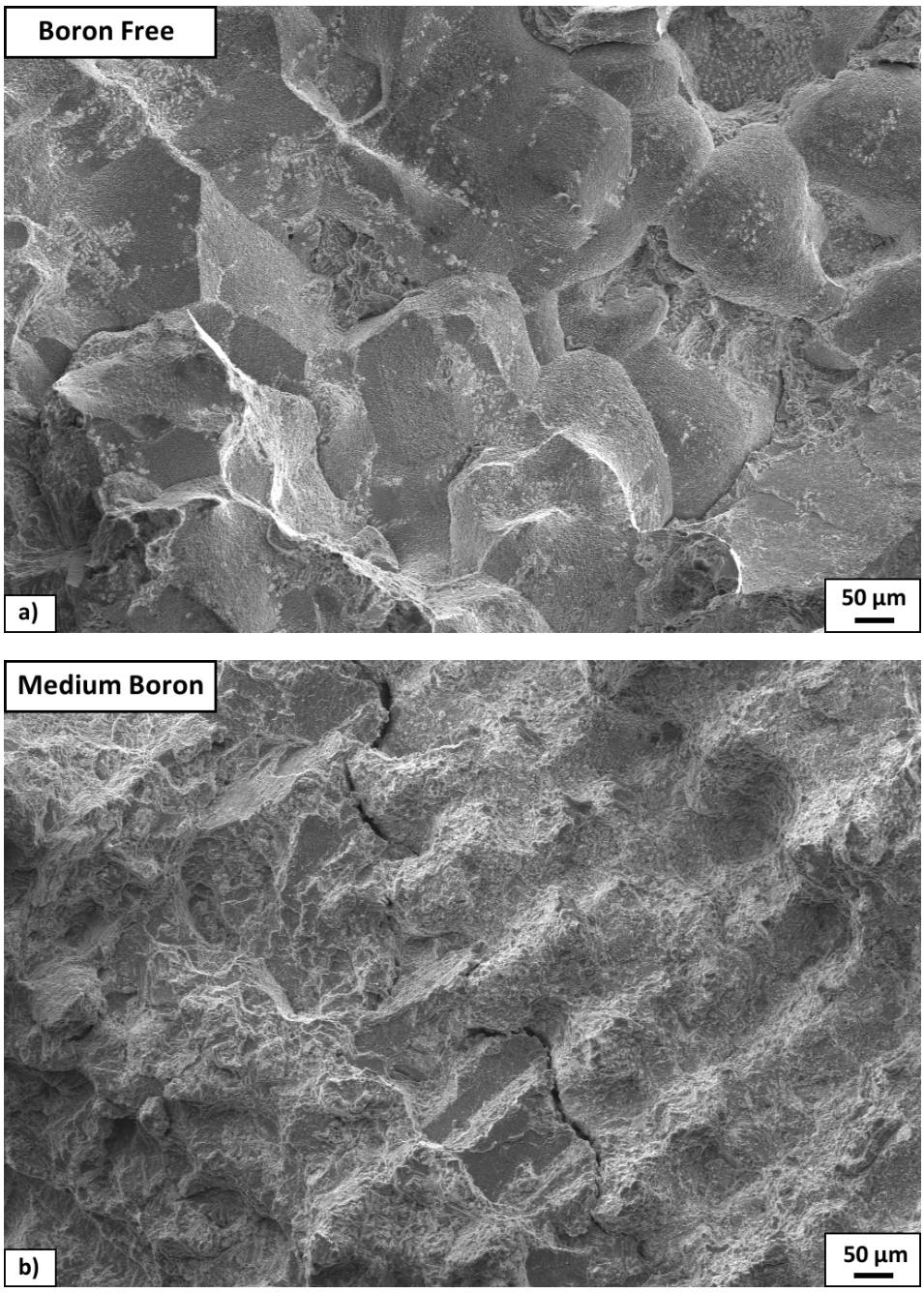


Figure 4.17: Fracture surfaces of creep specimens tested at 750 °C/455 MPa: a) intergranular failure of boron free alloy and b) mixed inter- and transgranular failure of medium boron alloy.

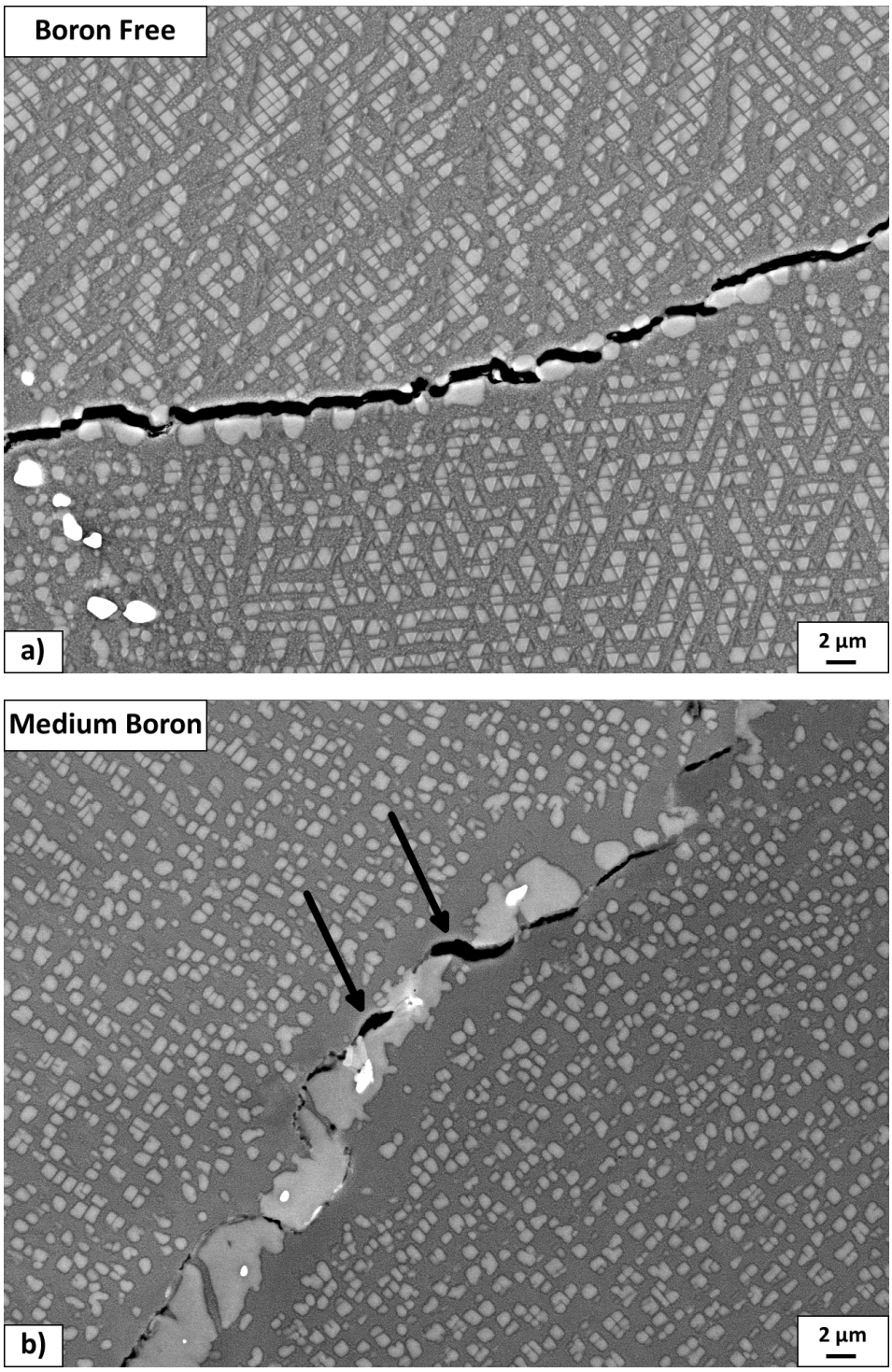


Figure 4.18: Backscattered SEM images of the creep specimens tested at 750 °C/455 MPa showing secondary cracks in: a) boron free and b) medium boron alloys. Dark areas at the grain boundaries indicated by arrows correspond to cracks in the medium boron alloy; the rest dark areas correspond to intergranular borides. Stress axis along perpendicular axis.

These results suggest that boron rather carbon plays the dominant role in grain boundary strengthening. The presence of $M_{23}C_6$ carbides along the grain boundaries of the boron free alloy combined with a co-segregation of carbon and boron leads to the worst creep performance. A significant improvement in creep rupture time is caused by the addition of 0.03 at.% B, due to the suppression of $M_{23}C_6$ carbides at grain boundaries by the precipitation of borides. Further addition of boron results in the precipitation of a higher volume fraction of borides; thereby, the medium boron alloy performs the best in terms of creep rupture time, for this particular set of conditions. But excessive boron, as in the high boron alloy, adversely affects creep resistance and results in the shortest creep rupture time yet it performs remarkably better than the boron-free alloy. From the above, it becomes readily apparent that beyond a critical volume fraction of borides precipitating at grain boundaries, their beneficial effect on creep properties is lost.

Finally, it may be true that the observed γ' layers at grain boundaries in the boron-containing alloys have a further concomitant role on the improve of creep performance, by hindering crack initiation at grain boundaries. MC carbides at grain boundaries enveloped within γ' layers were limited in the case of the boron free alloy, thus suggesting that a higher number of crack initiation sites is present as compared to the boron-containing alloys. Hence, it is suggested that a reduction of carbon content may further improve the creep properties of STAL15-CC. The effect of γ' layers at grain boundaries is investigated in detail in Chapter 5.

4.5.3 Grain Boundary Chemistry

Based on the atom probe analysis of the grain boundary interfaces, some further comments can be made concerning the possible role of grain boundary diffusion. It

is suggested that boron affects the diffusion of carbon along the grain boundaries. A high carbon concentration was found only at the grain boundary interface $\gamma/M_{23}C_6$ in the boron-free alloy, with concomitant boron segregation. However, in the presence of higher boron concentrations in the bulk material, carbon enrichment is suppressed and high boron concentrations dominate at grain boundary interfaces, such as the γ'/M_5B_3 interfaces in the boron-doped alloys, Figures 4.9(d) and 4.9(e).

This can be at least partially explained by the much higher mobility of boron compared to that of carbon. Whilst estimates of grain boundary mobilities are not well known, consider the calculated tracer diffusivity for boron and carbon in γ matrix, based on the MOBNI3 database [113], see Figure 4.19.

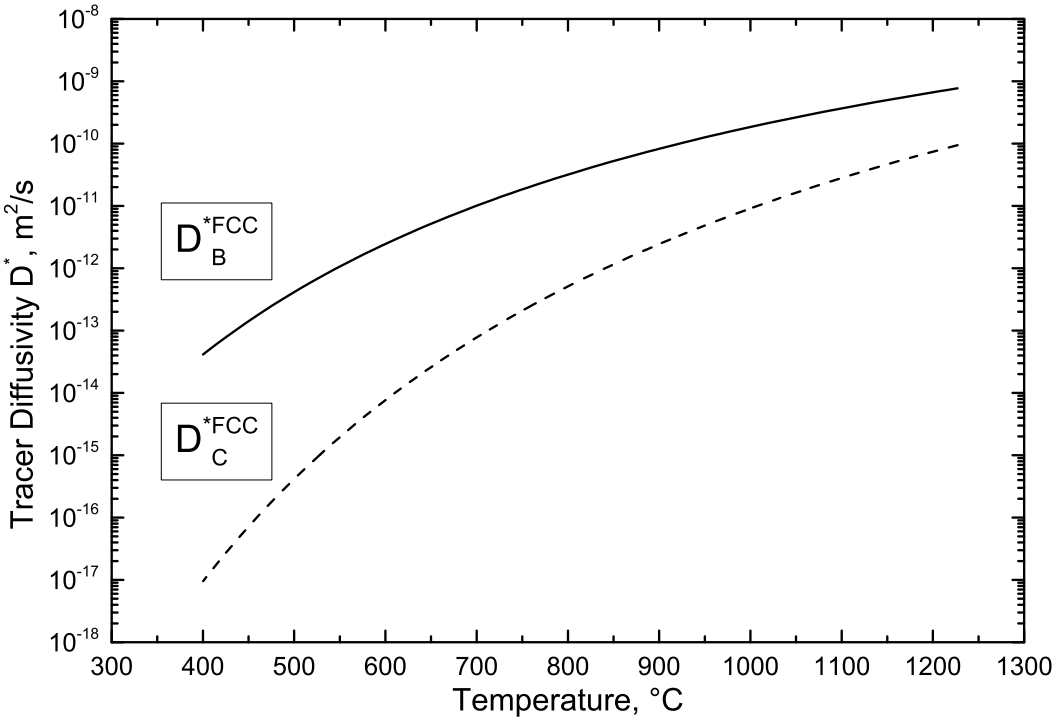


Figure 4.19: DICTRA calculations of boron and carbon tracer diffusivity in γ phase, based on the mobility database MOBNI3.

Clearly, boron can be expected to diffuse more quickly than carbon. This fact, combined with the higher amounts of boron in the boron-containing alloys, may lead to grain boundary sites being occupied primarily by boron, thereby hindering carbon segregation at the grain boundaries. These observations can be correlated directly with the occurrence of nano-sized $M_{23}C_6$ carbides in the grain rather than at the grain boundaries of the boron-containing alloys.

Furthermore, the morphologies of particles at grain boundaries can be altered due to the higher mobility of boron in γ matrix. For instance, when boron diffusion dominates, it can result in grain boundaries being decorated only with Cr-rich borides, as can be seen for instance in Figure 4.1(b). These effects may play a role in the mechanism of boride precipitation which so obviously influences the creep performance of this system.

4.6 Summary and Conclusions

In this study, detailed high resolution characterisation has been carried out of grain boundaries in boron-containing and boron-free versions of a new nickel-based superalloy which is being designed for power generation applications. The following specific conclusions can be drawn:

- In the boron-free case, carbides are prevalent at the grain boundaries. Scanning electron microscopy and atom probe tomography confirm the presence of Cr-rich $M_{23}C_6$ and Ta-rich MC carbides.

- When boron is absent, atom probe tomography has detected a C-enriched zone of approximately 3 nm at the grain boundary interface $\gamma/M_{23}C_6$. Trace boron

levels were found to co-segregate with carbon at the $\gamma/M_{23}C_6$ interface. Very little boron was found dissolved in the $M_{23}C_6$.

- In the boron-containing alloys, borides rather than carbides are prevalent at the grain boundaries. Transmission electron microscopy and atom probe tomography confirm the precipitation of Cr-rich M_5B_3 borides at grain boundaries.

- Atom probe analyses shown a B-enriched zone of approximately 3 nm at the γ'/M_5B_3 interface for all the boron-doped alloys. Carbon enrichment is suppressed by higher amounts of boron, combined with the higher boron mobility in γ compared to carbon. Such behaviour was not observed for any other type of interface.

- Segregation of boron or carbon was not detected at the MC/γ and MC/γ' grain boundary interfaces. These interfaces are the least desirable due to their low cohesion.

- Nano-SIMS mapping confirms that the majority of the boron in the boron-containing alloys is indeed present in the form of Cr-rich M_5B_3 borides, and not in bulk solid solution.

Chapter 5

The Role of Boron on Improving Ductility in a New Polycrystalline Superalloy

5.1 Introduction

The ductility of the nickel-based superalloys can be exploited for high temperature applications [114]. But what factors influence it? When in polycrystalline form, intergranular fracture is common particularly under the high temperature conditions of greatest technological relevance; it follows that the effects occurring at the grain boundaries must play a significant role in promoting or limiting ductility [115, 116]. But more fundamental studies are needed to elucidate the physical mechanisms which are at play.

One difficulty is that traditional approaches rely upon post-mortem studies for the deduction of microstructure/property relationships in such materials. For example, emphasis is often placed on fracture surfaces or dislocation structures examined at ambient conditions, when in fact it is the effects occurring at temperature and with the load applied which are clearly of the greatest relevance. *In-situ* studies circumvent these difficulties and are therefore of significant value in the search for a greater appreciation of the phenomena which control properties [117, 118].

In this Chapter, a study is made of the behaviour of a prototype polycrystalline superalloy designed recently for power generation applications. A boron-free and boron-containing variant are examined. *In-situ* tensile tests are carried out in the scanning electron microscope to examine the factors promoting ductility. In this way, insights are provided into the role played by boron in promoting ductility in these alloys.

5.2 Background

As will become apparent later in this Chapter, a significant role is played by boron in the serration of grain boundaries in this superalloy and therefore attention is paid here to the prior literature on this topic. The serration of grain boundaries has been reported to have an influence on mechanical properties in polycrystalline nickel-based superalloys by impeding grain crack propagation [101, 119–123]. In particular, voids and cavities forming at serrated grain boundaries cannot interlink; preventing the formation of a continuous crack path. Moreover, serrated grain boundaries invoke longer diffusion paths along the grain boundaries. Environmental effects at elevated temperatures are thus retarded. A grain boundary is considered to be a serrated grain boundary when the serration amplitude is larger than $0.5\,\mu$m [101]. However, the

driving force for the formation of grain boundary serrations is not well understood.

Different theories have been developed that attempt to rationalise the formation of serrated grain boundaries in nickel superalloys. Firstly, serrated grain boundaries are strongly related with heterogeneous nucleation of γ' at the grain boundaries [122, 124–126]. In this case, a serration results from pinning of a grain boundary at primary γ' precipitate in conjunction with its movement between the primary γ' particles. The grain boundary migration continues until γ' particles form homogeneously throughout the grain; playing the role of a physical barrier that prevents further migration. Moreover, the occurrence of a serration depends strongly on the cooling rate from the solution treatment temperature through the γ' precipitation zone [123, 124, 127, 128]. Low cooling rates result in serrated grain boundaries, providing sufficient time for grain boundaries to grow. Rapid cooling led to smaller heterogeneously formed γ' particles; consequently planar grain boundaries form [123, 127]. The serration amplitude and wavelength increase as cooling rate decreases and solution temperature increases.

Another prerequisite for this mechanism requires the solution heat treatment temperature to be well above the solvus temperature of the major grain boundary carbides, e.g. $M_{23}C_6$. However, the role of $M_{23}C_6$ carbides in the formation of serrated grain boundaries or not is controversial. Studies suggest the idea that serrated grain boundaries form due to the precipitation of $M_{23}C_6$ carbides at the grain boundaries, whereas planar grain boundaries occur in their absence [129, 130].

By contrast, Hong *et al.* [101] suggests that composition has a role; providing a driving force for grain boundary serrations from discontinuous chromium and carbon segregation along the grain boundaries in a Nimonic 263 alloy. Inhomogenous segregation of carbon and chromium provide varying magnitudes of lattice distortion

along the grain boundaries, while this is not observed when the segregation is continuous. This has been rationalised using a calculation by McLean [131], where the lattice strain energy for carbon, given as $47.9\,\mathrm{kJ\,mol^{-1}}$, was found to be far greater than chromium, at $1.2\,\mathrm{kJ\,mol^{-1}}$ [101]. As a consequence, grain boundary serration is not expected in cases of low carbon content in solid solution.

If the accumulation of strain energy results in a distortion of the grain boundary itself, one can infer that serrated grain boundaries may occur between a distorted and undistorted lattice border arising from discontinuous segregation. It was suggested that the non-uniform distortional lattice strain along the grain boundary acts as the driving force for the onset of grain boundary serrations. Contrary to this, in a study of a ternary Ni-xCr-0.1C model alloy, chromium was found to increase the serration amplitude [132].

Apart from carbon and chromium, serrated grain boundaries were found to form with the segregation of boron at the grain boundary in Astroloy, as confirmed by atom probe studies [111]. In the current study serrated grain boundaries were observed in a boron-containing alloy; whereas planar grain boundaries occur in the absence of boron.

5.3 Experimental Procedures

The prototype nickel-based polycrystalline superalloy STAL15-CC was used in this study. In order to investigate the effect of boron on the mechanical properties, test-bars with no boron (boron free - BF) and boron-containing (BC - 0.05 at.% B) content were produced by conventional casting. The boron-containing alloy corresponds to the medium boron variant of STAL15-CC, which was shown to have the best creep performance in terms of creep rupture time as described in Chapter 4.

5.3.1 High-Temperature Tensile Tests

Tensile tests were performed using an Instron 8800 electro-thermal mechanical testing (ETMT) device at 750 °C and under displacement control with speed of 10 μm s^{-1} and 0.1 μm s^{-1}, corresponding to strain rates, $\dot{\epsilon}$, of approximately 2×10^{-3} s^{-1} and 2×10^{-5} s^{-1}, respectively. Specimens were machined from fully heat treated bars by electro-discharge machining (EDM). The gauge volume of the specimens was designed as 5 mm length × 2 mm width × 1 mm thick. Specimens were mechanically ground with abrasive media prior to tests to remove the oxidised layer present from the EDM. Heating was achieved by passing direct current (DC) through the gauge length of the specimen controlled by a thermocouple which was spot-welded to the centre of the gauge length. The displacement between the grips was measured with the use of a linear variable differential transducer (LVDT). Figure 5.1 illustrates the described experimental set-up.

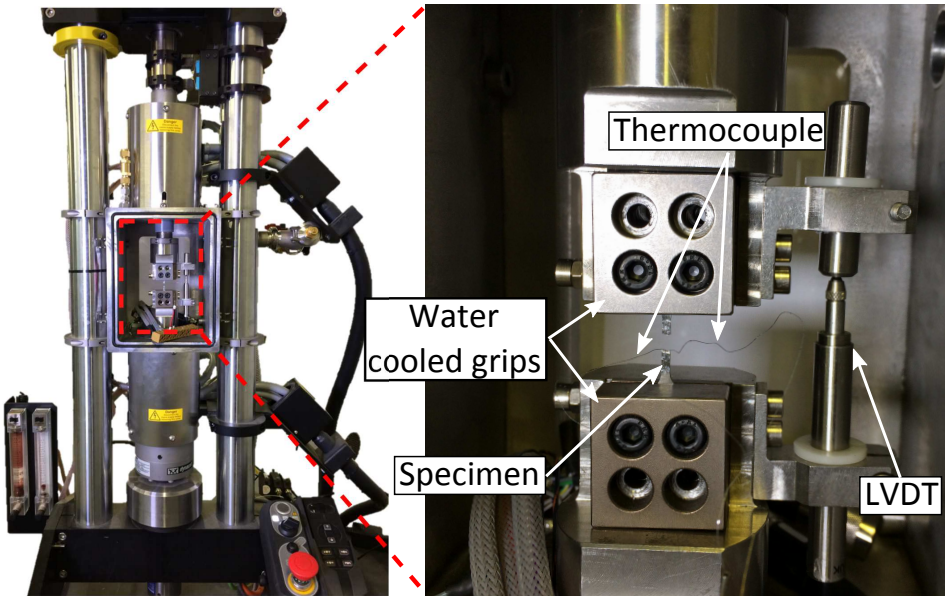


Figure 5.1: Detailed experimental set-up for performing tensile tests using the ETMT device in this study.

In-situ tensile tests were performed at 750 °C and under displacement control with speed of 0.1 μm s^{-1}, corresponding to strain rate, $\dot{\epsilon}$, of approximately 2×10^{-5} s^{-1} to failure. A Kammrath-Weiss *in-situ* module, equipped with a resistance heater, was mounted on a Zeiss EVO SEM with a LaB_6 filament. Double dogbone specimens were machined from fully heat-treated bars by EDM with a gauge volume of 5 mm length $\times$ 2 mm width $\times$ 1 mm thick. Once again the surfaces were mechanically ground with abrasive media to a 1 μm finish. Secondary electron images were obtained at 750 °C with surfaces etched using Kalling's solution to reveal grain boundaries.

Two thermocouples were used to monitor temperature during the tests; one was fitted between the sample and the heater and the other was spot-welded onto the sample surface. In order to improve thermal conductivity in vacuum conditions, heating was via conduction from a heated surface, with the sample held in place with tungsten wire springs; gold leaves were placed in between to improve thermal conductivity. An illustration of the experimental set-up is shown in Figure 5.2.

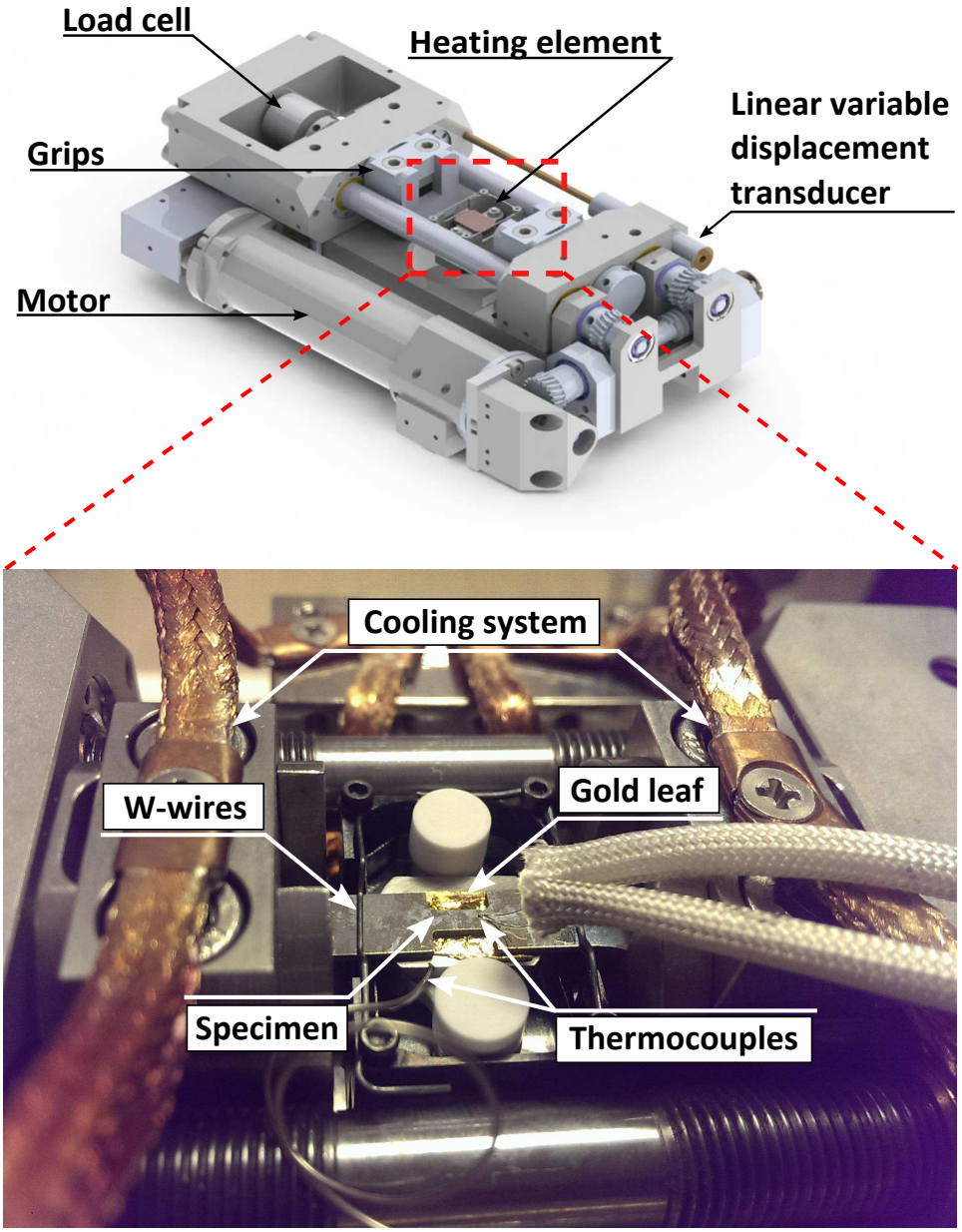


Figure 5.2: Detailed experimental set-up used for the *in-situ* tensile tests in this study.

5.3.2 High-Resolution EBSD Strain Mapping

Cross-correlation-based high-resolution electron backscattered diffraction (HR-EBSD) analysis was conducted from fully heat treated specimens before and after deformation at elevated temperatures. This method allows the investigation of elastic strains at microscopic scales [133]. Information on plastic deformation can be inferred by quantifying the geometrically necessary dislocation (GND) density, based upon measurement of the lattice curvature and subsequent analysis of the Nye tensor [134]. This technique has been utilised in various materials to study for instance GND distributions after tensile deformation in Ti [135] and residual stresses and GND accumulation in annealed [136, 137] and deformed copper [138]. The method has also been applied to superalloys with measurements being made of strains and GND densities near carbide particles and oxide agglomerates after thermal loading and room temperature deformation [139, 140].

Specimens with the exact same geometry as in the case of the *in-situ* tensile tests were polished to $0.04\,\mu$m colloidal silica finish for HR-EBSD analysis. Grain boundaries perpendicular to the tensile axis were selected. Prior to any deformation, backscattered images were taken and HR-EBSD maps were collected. The specimens were then deformed under vacuum at $750\,^{\circ}$C and under displacement control with speed of $0.1\,\mu\mathrm{m\,s^{-1}}$ using the *in-situ* tensile module mounted on a Zeiss EVO SEM and interrupted after a total of $0.5\,\%$ permanent deformation. The specimens were then cooled slowly to room temperature ($0.8\,^{\circ}$C/s) and diffraction patterns were collected on a JEOL 6500F. Although the tests were conducted in vacuum, the surface of the specimens was slightly oxidised. This layer was removed by lightly polishing with colloidal silica, suitable for further characterisation. HR-EBSD maps were subsequently collected from the same grain boundary regions as prior to deformation.

HR-EBSD patterns were recorded as described in Chapter 3. Lattice rotations and elastic strain variations within the sample cause small shifts in the positions of zone axes and other features in the EBSD patterns obtained as the electron beam is scanned over the sample. These small pattern shifts are measured relative to a reference pattern selected in each grain using automated image-processing based on cross-correlation analysis and then related to the size and nature of the strains and rotations.

5.4 Results

5.4.1 Grain Boundary Serration

Figures 5.3(a) and 5.4(a) show backscattered SEM images from typical fully heat treated grain boundary regions of both investigated alloys. Corresponding EBSD analysis is shown in Figures 5.3(b) and 5.4(b). The inverse pole figure (IPF) maps is shown to identify crystal orientation and strain maps associated with ϵ_{11}, ϵ_{12} and ϵ_{22} components are given.

Serration of the grain boundary is present in case of the boron-containing alloy, whereas a relatively planar grain boundary is observed in the boron-free sample. In Chapter 4 it was shown that in the case of the boron-free alloy Cr-rich $M_{23}C_6$ were found to decorate the grain boundaries whereas their formation was suppressed by the addition of boron. Instead, Cr-rich M_5B_3 borides form along the grain boundaries of the boron-containing alloy. The precipitation of Ta-rich MC carbides was not influenced by the addition of boron.

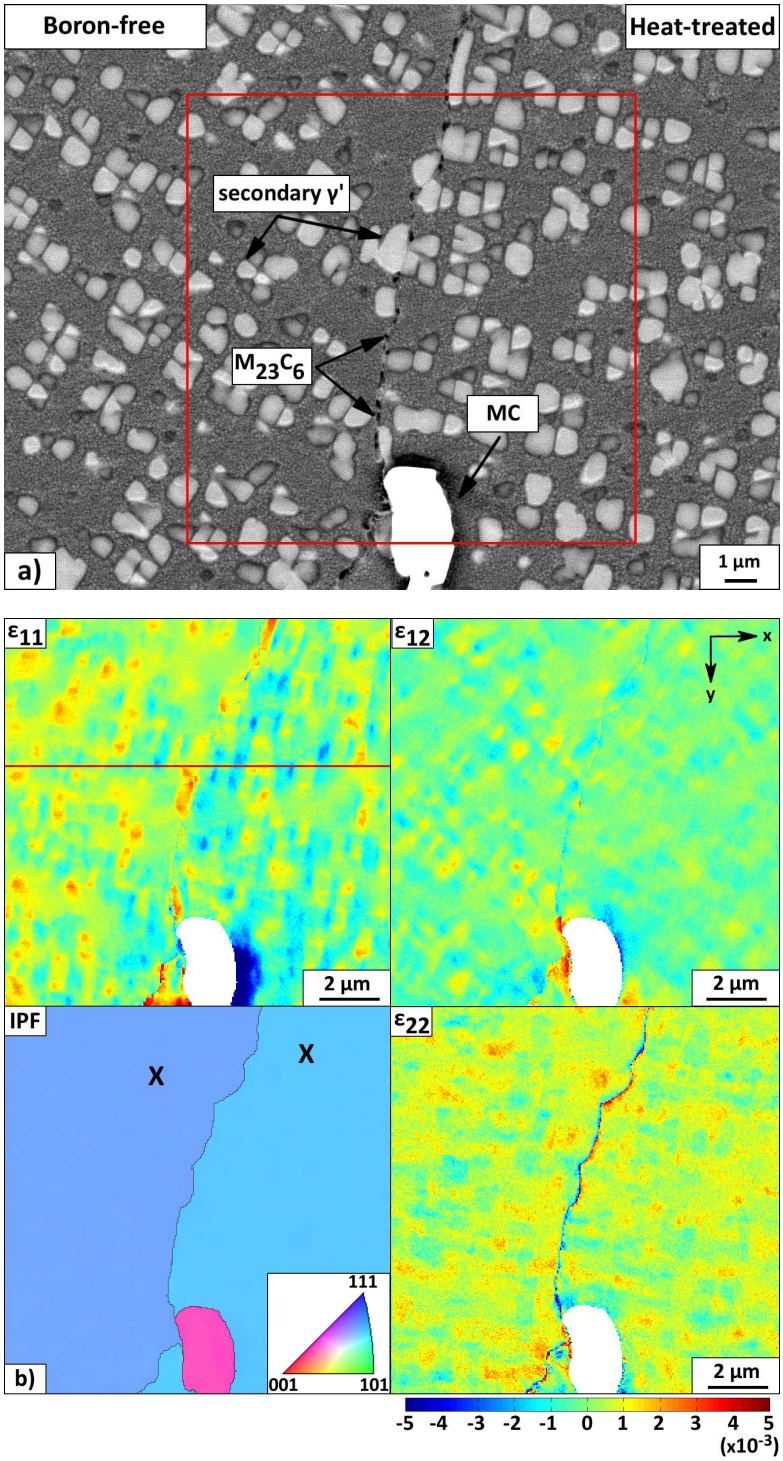


Figure 5.3: Grain boundary region from the boron-free alloy: a) backscattered SEM image after full heat treatment and b) HR-EBSD strain maps alongside inverse pole figure (IPF) map of the investigated area as denoted by the red box. The red line corresponds to line-scans shown in Figure 5.11. The X's indicate the reference points for the strain map analysis.

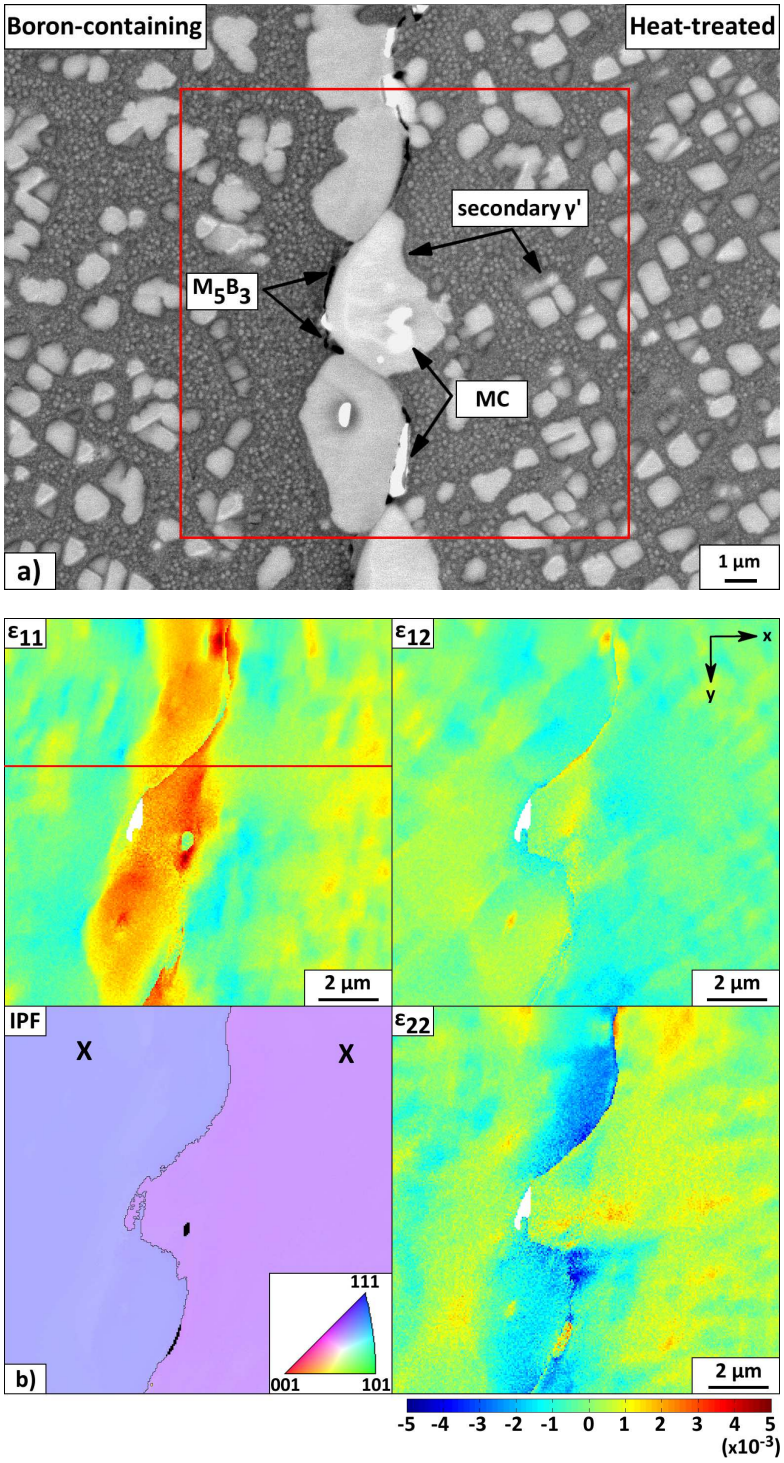


Figure 5.4: Grain boundary region from the boron-containing alloy: a) backscattered SEM image after full heat treatment and b) HR-EBSD strain maps alongside inverse pole figure (IPF) map of the investigated area as denoted by the red box. The red line corresponds to line-scans shown in Figure 5.11. The X's indicate the reference points for the strain map analysis.

Furthermore, Figures 5.3(b) and 5.4(b) illustrate HR-EBSD strain maps prior to deformation for the boron-free and boron-containing alloys, respectively. The γ/γ' microstructure is revealed in the strain maps. Cooling from the ageing temperature combined with the different thermal expansion coefficients between the γ/γ' microstructure and the carbides/borides results in residual thermal strains, as can be seen in the HR-EBSD maps.

In the boron-free case residual thermal strains are observed in the vicinity of MC carbide at the grain boundary. In particular, the normal strain ϵ_{11} along the horizontal x axis is mostly compressive to the right of the MC carbide. Similar observations were made before for a directionally solidified superalloy containing blocky MC carbides and for a powder metallurgy produced nickel superalloy containing non-metallic inclusions [139, 140]. Any direct correlation of residual thermal strains with the presence of $M_{23}C_6$ carbides along the grain boundaries was not possible, due to the small size of these particles. Thermal residual strains are uniformly distributed within the grains.

In the boron-containing alloy the intergranular MC carbides are mainly enveloped within γ' layers along the grain boundary. The observed residual thermal strains are concentrated around and within these layers. The grain boundary γ' forms an almost continuous layer along this part of the boundary and thermal strains ϵ_{11} across the vertical boundary layer are more tensile within that layer. The strains ϵ_{22} along the layer tend to be compressive within the grain boundary γ'. Strain variations associated with the γ' particles within the grain are present but less obvious in the boron-containing alloy due to the presence of the grain boundary γ'. It is noted that this occurs at a grain boundary which is serrated. Variations in the residual thermal strains across the grains can be observed in the boron-containing case.

5.4.2 Tensile Performance at 750 °C

The stress *vs.* engineering strain curves for both boron-free (BF) and boron-containing (BC) alloys at 750 °C and strain rates, $\dot{\epsilon}$, $2\times10^{-3}\,s^{-1}$ and $2\times10^{-5}\,s^{-1}$ are shown in Figure 5.5. It can be seen that the beneficial effect of boron at elevated temperatures exhibits a strain rate dependent character. In particular, for the higher investigated strain rate, the performance of both alloys is similar in terms of ductility; implying no improvement in tensile properties by the addition of boron.

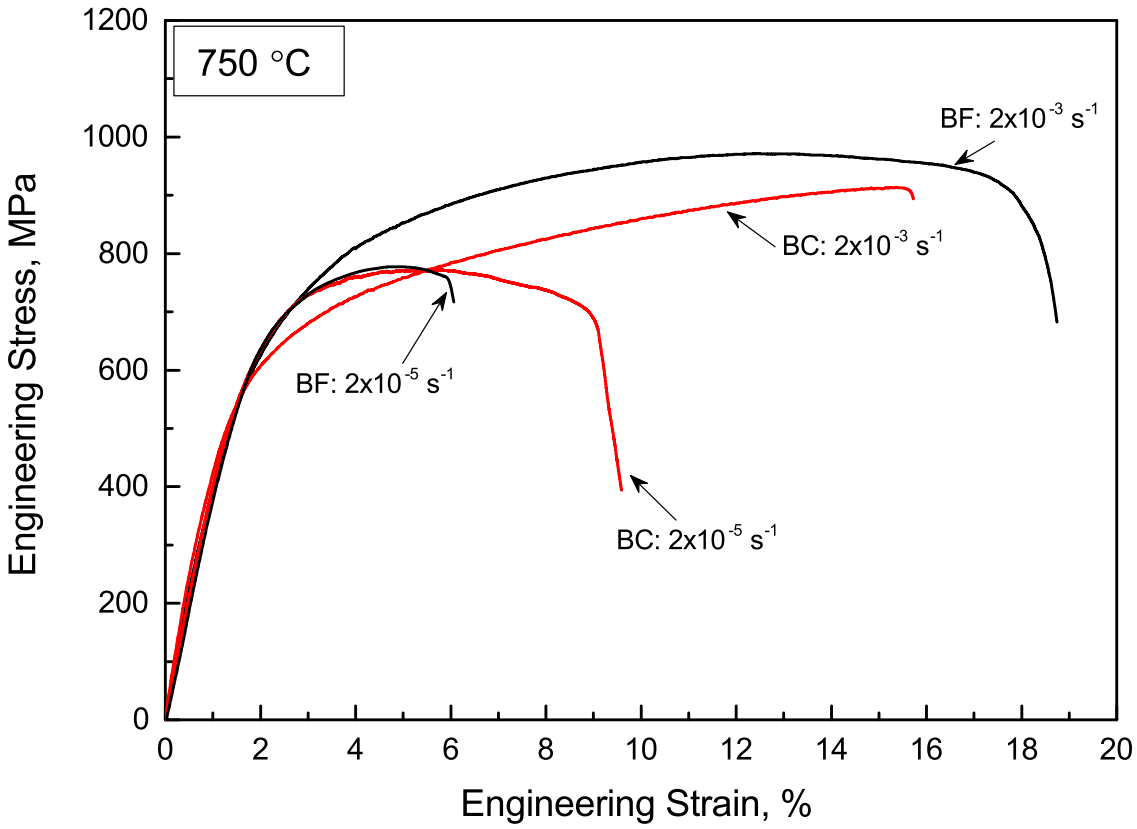


Figure 5.5: Engineering strain *vs.* engineering stress curves at 750 °C and strain rates 2x10^{-3} s^{-1} and 2x10^{-5} s^{-1} for both boron-free and boron-containing alloys collected using the ETMT device.

However, as the strain rate decreases, a different behaviour is observed for both alloys. In the case of the boron-free alloy, a dramatic drop compared to the higher rate test by nearly 60 % in ductility is observed, whereas in the boron-containing alloy the ductility is reduced only 30 %. The UTS recorded for the two alloys at this lower strain rate are very similar. At the lower strain rate, diffusion phenomena at grain boundaries becomes more important. Thus, factors such as the grain boundary character, and therefore boron addition is highly important. For this reason, the *in-situ* tensile tests were performed only at the lower investigated strain rate.

It is noteworthy that an overestimation of strain during tensile tests using the ETMT device is possible due to the nature of the experimental set-up. The reason for it could be the undefined effective gauge length, which is strongly linked with the non-uniform temperature profile along the sample. Nevertheless, the strain data shown here can be used for a qualitative comparative analysis between different samples. Any future quantitative analysis should be performed on standard-sized test specimens by measuring the displacement with the use of an extensometer.

The improvement in ductility is also confirmed by the examination of the different fracture surface character between the boron-free and boron-containing alloy. Figure 5.6 illustrates surface measurements of the fracture surfaces of the specimens tested using the ETMT at strain rate $2\times10^{-5}\,\mathrm{s}^{-1}$. The measurements were conducted using an optical Alicona microscope. In the boron-free case shown in Figure 5.6(a), a relatively flat fracture surface is observed, indicating a brittle fracture of the boron-free alloy at 750 °C. By contrast, a less flat fracture surface is observed in the case of the boron-containing alloy (Figure 5.6(b)), implying a more ductile fracture.

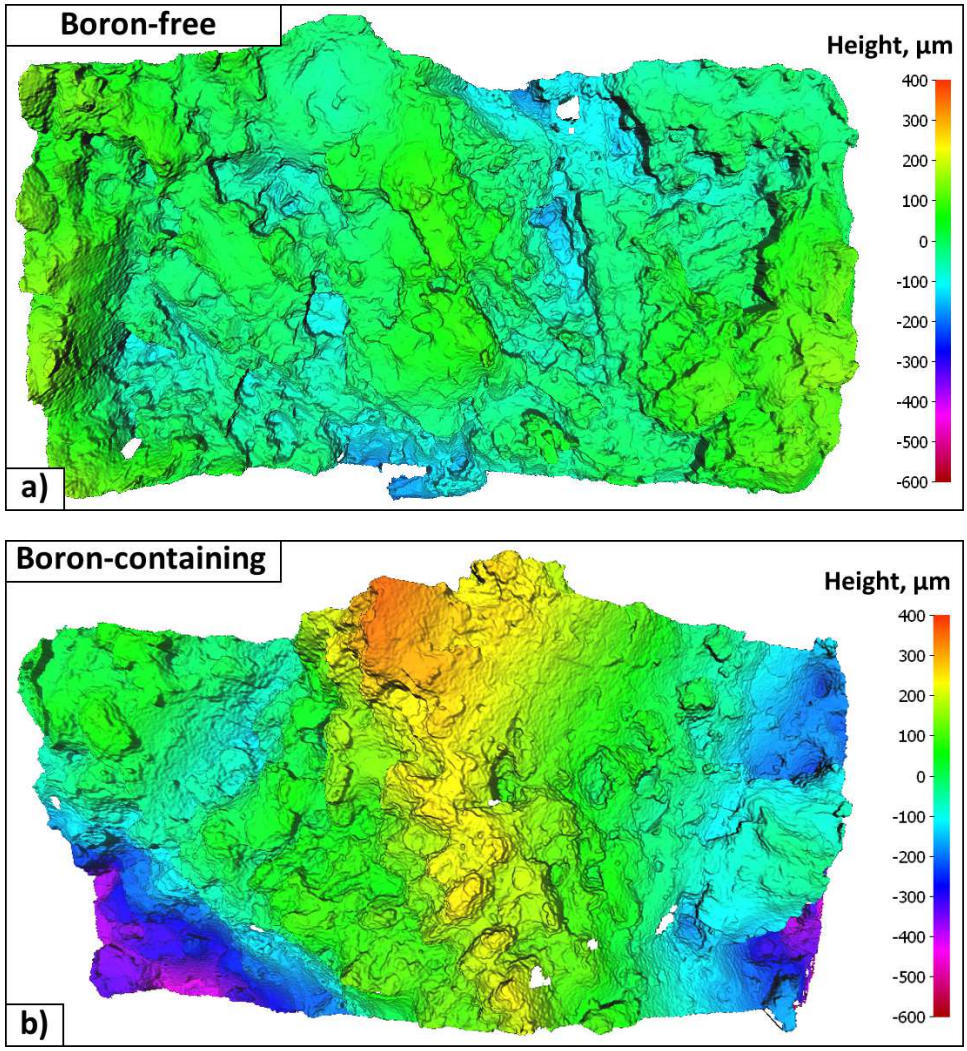


Figure 5.6: Fracture surfaces of ETMT specimens from: a) boron-free and b) boron-containing alloys tested at 750 °C and strain rate 2x10^{-5} s^{-1}. Topography measurements performed using an Alicona microscope.

5.4.3 *In-situ* Observations

Interrupted *in-situ* tensile tests were performed for both alloys, investigating the grain boundaries shown in Figures 5.3(a) and 5.4(a). The tensile tests were performed at 750 °C and under displacement control with speed of 0.1 μm s^{-1}, corresponding to strain rate, $\dot{\epsilon}$, of 2×10^{-5} s^{-1}. They were interrupted after a total of 0.5 % perma-

nent plastic deformation, in order to collect data for EBSD strain mapping analysis. Figures 5.7(a) and 5.8(a) show the analysed grain boundary regions from the boron-free and boron-containing alloy after the deformation and corresponding HR-EBSD strain maps are shown in Figures 5.7(b) and 5.8(b), respectively.

After deformation the HR-EBSD maps reveal clear difference between the two alloys. In the case of the boron-free alloy, the most striking feature is the band of high in-plane shear strain ϵ_{12} in the left hand grain which is concentrated near the grain boundary and is particularly intense near the MC carbide towards the bottom of the map. The normal strains (ϵ_{11} and ϵ_{22}) show smaller variations compared to the shear strain and variations around the secondary γ' are less marked than before deformation. The GND density map in Figure 5.7(b) shows a thin band of high GND density which accumulates along nearly the entire length of the investigated grain boundary. The GND density map also shows rings of higher density generated by dislocation activity in the γ matrix surrounding the secondary γ' particles. Microvoids have also formed at the grain boundaries associated with $M_{23}C_6$ carbides as indicated by white arrows in Figure 5.7(a).

In the case of the boron-containing alloy, the band of high ϵ_{11} strain across the grain boundary γ' layer has been significantly reduced by the deformation, as illustrated in Figure 5.8(b). In-plane shear strains ϵ_{12} increase markedly compared to the the undeformed state and high values are localised at the grain boundary within the grain boundary γ'. The GND density shows greater dislocation storage close to the grain boundary compared to the boron-free alloy, and furthermore the high GND regions are not continuous along the grain boundary but instead are strongly associated with segments of the boundary that are perpendicular to the load axis. Boundary segments inclined at +/- 45 ° to the loading axis have relatively low GND density associated with them.

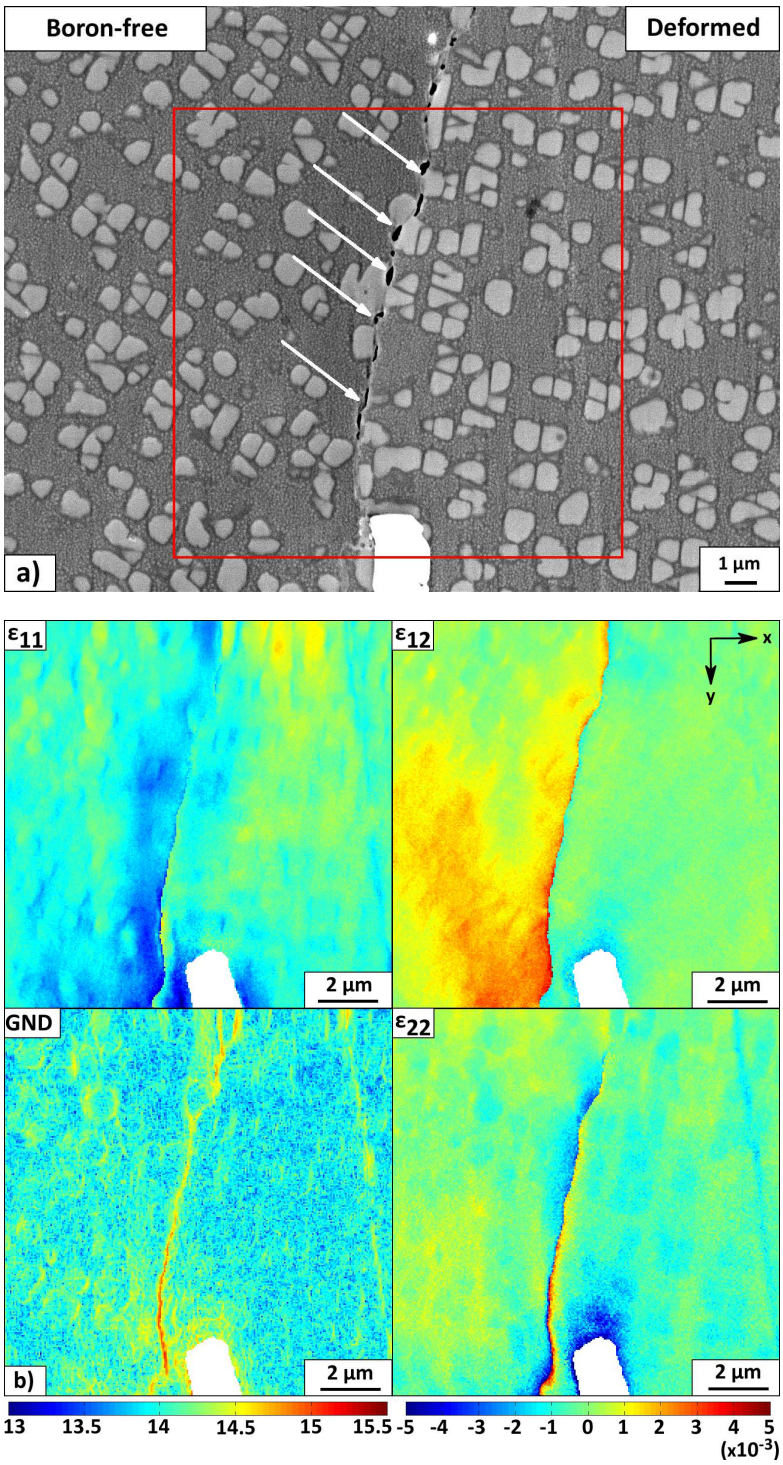


Figure 5.7: Grain boundary region from the boron-free alloy: a) backscattered SEM image after $\sim$0.5 % deformation at 750 °C and strain rate 2x10^{-5} s^{-1} and b) HR-EBSD strain maps and GND density map of the investigated area as denoted by the red box after deformation with the scale bar in $\log_{10}$ scale of dislocation lines m^{-2}. Note the load direction is along the x axis. The white arrows indicate voids.

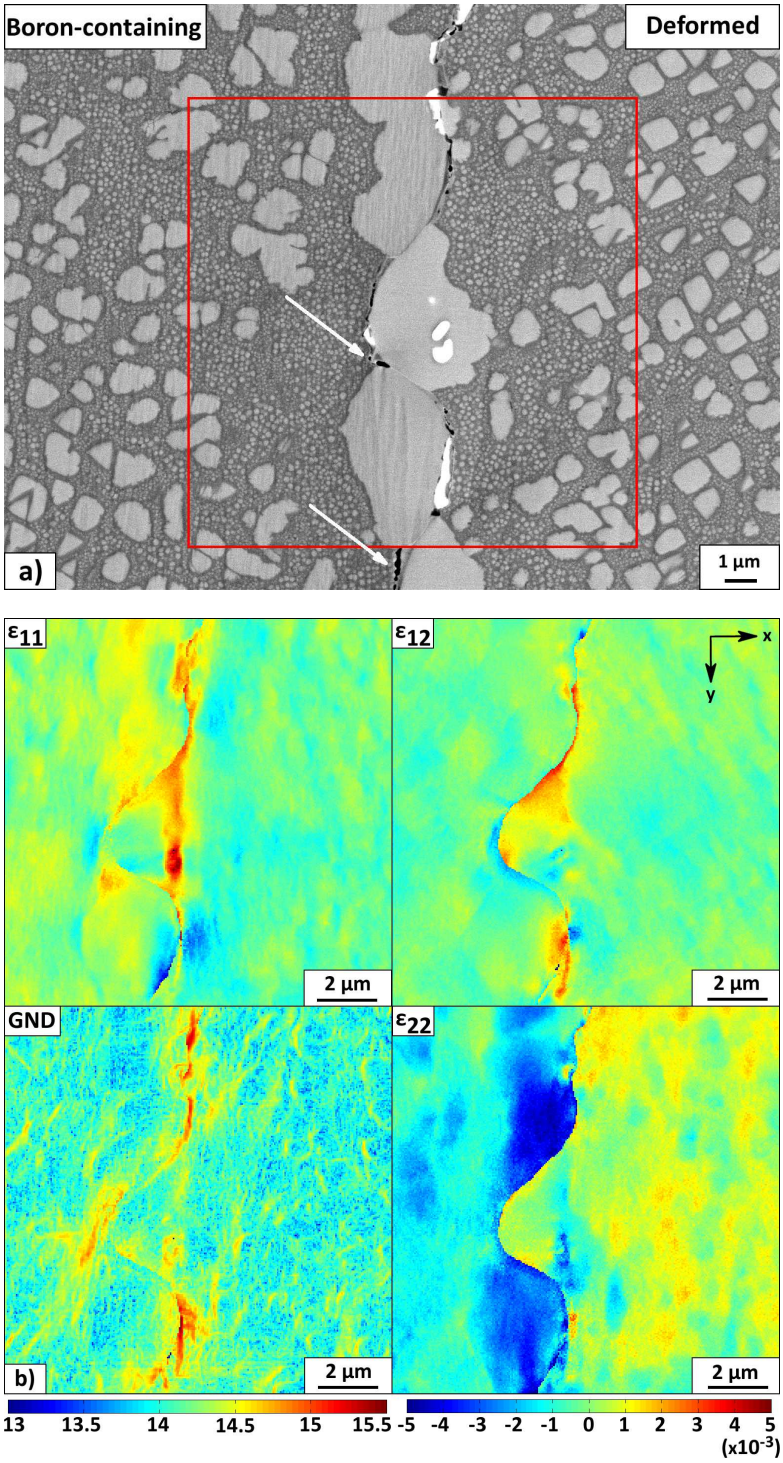


Figure 5.8: Grain boundary region from the boron-containing alloy: a) backscattered SEM image after $\sim$0.5 % deformation at 750 °C and strain rate 2x10^{-5} s^{-1} and b) HR-EBSD strain maps and GND density map of the investigated area as denoted by the red box after deformation with the scale bar in $\log_{10}$ scale of dislocation lines m^{-2}. Note the load direction is along the x axis. The white arrows indicate voids.

Moreover, boron-free and boron-containing specimens tested in tension to failure at 750 °C and under displacement control with speed of $0.1\,\mu\mathrm{m\,s^{-1}}$ using the *in-situ* tensile module. All the figures shown in this study from the *in-situ* investigations were captured at 750 °C.

Figures 5.9 and 5.10 illustrate series of secondary electron SEM images of fully heat treated grain boundary regions of boron-free and boron-containing alloys tested in tension to failure, respectively. In both cases, damage formation is concentrated solely at the grain boundaries, resulting in intergranular failure. However, some differences are observed in the crack propagation along the grain boundaries between the two alloys. In particular, in the boron-free case voids form just after yield (Figure 5.9(b)) along the grain boundary. Voids form at incoherent interfaces at the grain boundaries, particularly between the $M_{23}C_6$ and the incoherent grain. As strain is increased, voids grow and interlink leading to a continuous crack path along the grain boundary.

By contrast, in the boron-containing alloy, voids form only at interfaces perpendicular to tensile axis (Figure 5.10(b)). As the test proceeds and strains increase voids grow. Due to the serrated character of the grain boundary, voids cannot form a continuous crack path that would lead to premature failure as in the boron-free alloy. Excessive cracking of intergranular MC carbides was not observed at 750 °C for either alloy.

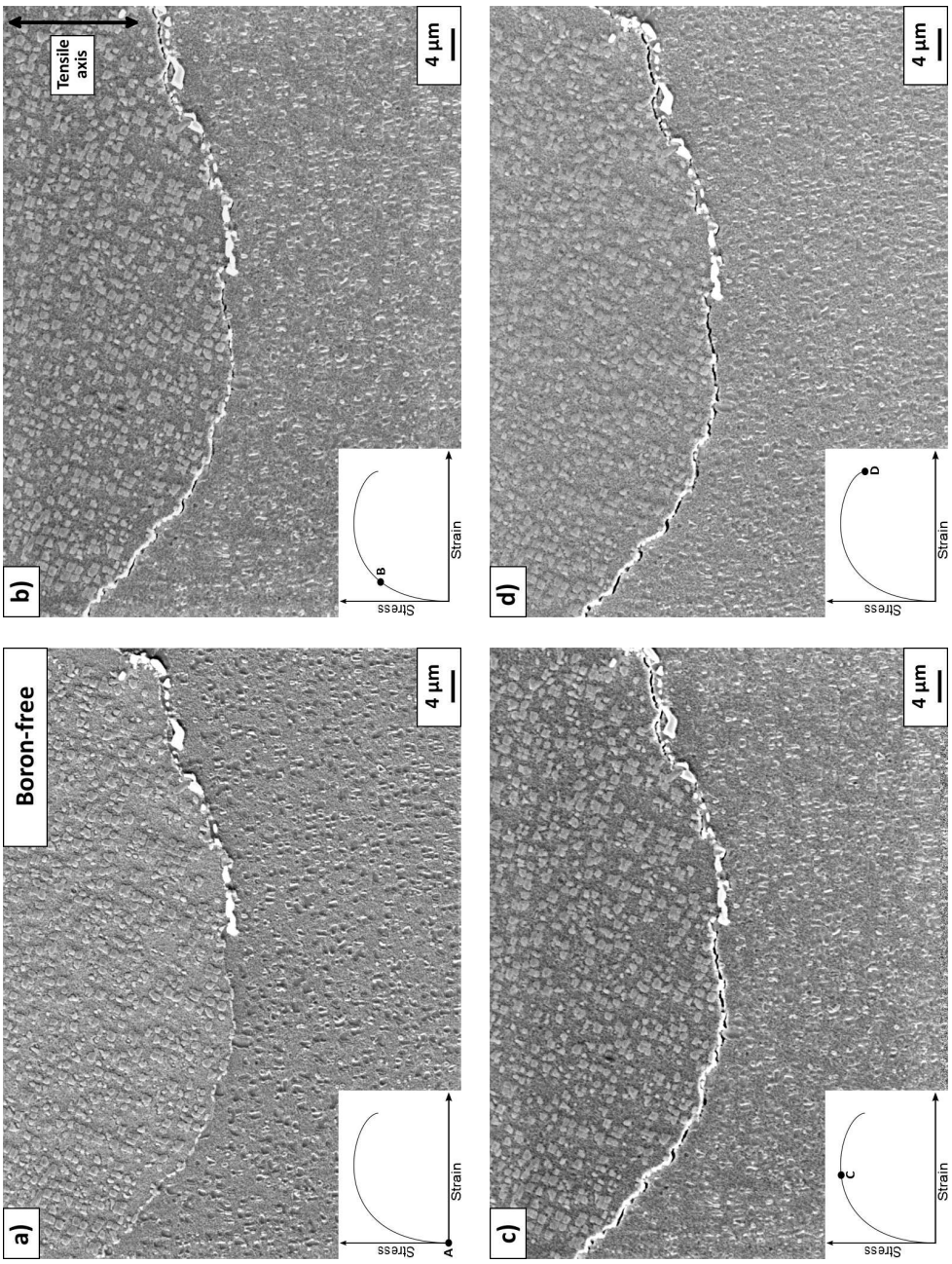


Figure 5.9: Sequential SEM images of a fully heat treated grain boundary region of the boron-free alloy tested in tension to failure: a) prior to deformation, b) after yield point, c) $\sim 3\,\%$ strain and d) after failure. Tensile axis in perpendicular direction.

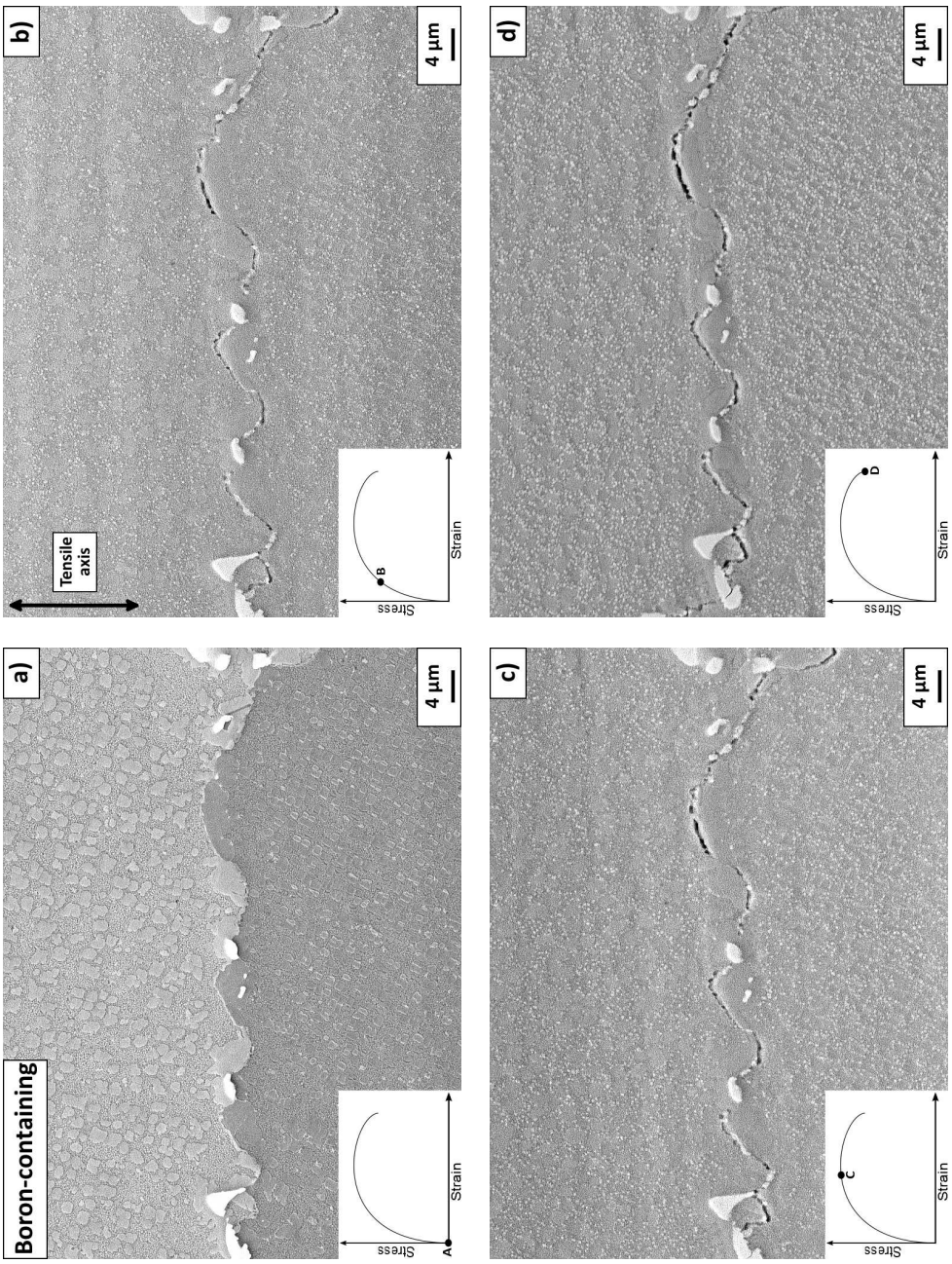


Figure 5.10: Sequential SEM images of a fully heat treated grain boundary region of the boron-containing alloy tested in tension to failure: a) prior to deformation, b) after yield point, c) $\sim 3\,\%$ strain strain and d) after failure. Tensile axis in perpendicular direction.

5.5 Discussion

5.5.1 The Ductilising Effect of Boron

The results conclusively show that the addition of boron improves the ductility at elevated temperatures. The beneficial effect of boron is more pronounced at relatively slow strain rates as shown earlier (see Figure 5.5), where the grain boundary character has stronger influence on the mechanical properties. Voids formation and oxidation along the grain boundaries determines that the failure is intergranular.

Moreover, it was shown that the addition of boron results in grain boundary segments being serrated; thus ductility is improved. The misorientation between the grains where serration occurs was measured using the EBSD method. The measured misorientation between the two investigated grains presented in Figure 5.4(b) is listed in Table 5.1 (1st measurement); information from other serrated grain boundaries is also given. It is clearly shown that the serration occurs at random high angle grain boundaries exhibiting no lattice sites coinciding between the two grains.

Winning *et al.* [141] has shown that high angle grain boundaries can move under the influence of an external shear stress. In a similar manner, increased lattice strain energy caused by the segregation of elements such as boron to the grain boundaries can initiate grain boundary motion which will eventually result in a serrated grain boundary. The segregation needs to be discontinuous in order for different segments of the grain boundary to exhibit a different lattice strain energy.

Table 5.1: Summary of serrated grain boundaries and corresponding misorientation, serration amplitude and wavelength measurements for the boron-containing alloy.

Misorientation, θ°	**Amplitude A, μm**	**Wavelength λ, μm**
26	1.3	4.8
28	1.6	3.1
40	1.2	3.7
40	1.2	3.8
56	1.5	3.3

In Figures 5.3(b) and 5.4(b) the different distribution of lattice strains are evident between the boron-free and boron-containing alloy. In the case of the boron-free alloy, the lattice strains are shown to be relatively uniformly distributed whereas the addition of boron resulted in the serrated segments of the grain boundary leading to higher lattice strains compared to grain interior.

Figure 5.11 shows an arbitrary line-scans across the grains of the boron-free and boron-containing alloys, showing the measured lattice strain as a function of distance. The position of the line-scans in the strain maps is shown in Figures 5.3(b) and 5.4(b). The higher lattice strains at the grain boundary compared to those in the bulk are apparent in the boron-containing alloy. The fluctuation of lattice strains across the grains in the boron-free alloy are present from the secondary γ' precipitates. Fluctuation of similar amplitude and spacing are not observed in the boron-containing alloy, as expected in absence of secondary γ'.

The amplitude and wavelength of the serrated grain boundaries were measured and shown in Table 5.1. Similar values for the serration amplitude and wavelength were measured for the various grain boundaries, indicating that there is no correlation between the misorientation and the magnitude of serration, for the selected boundaries observed in this work.

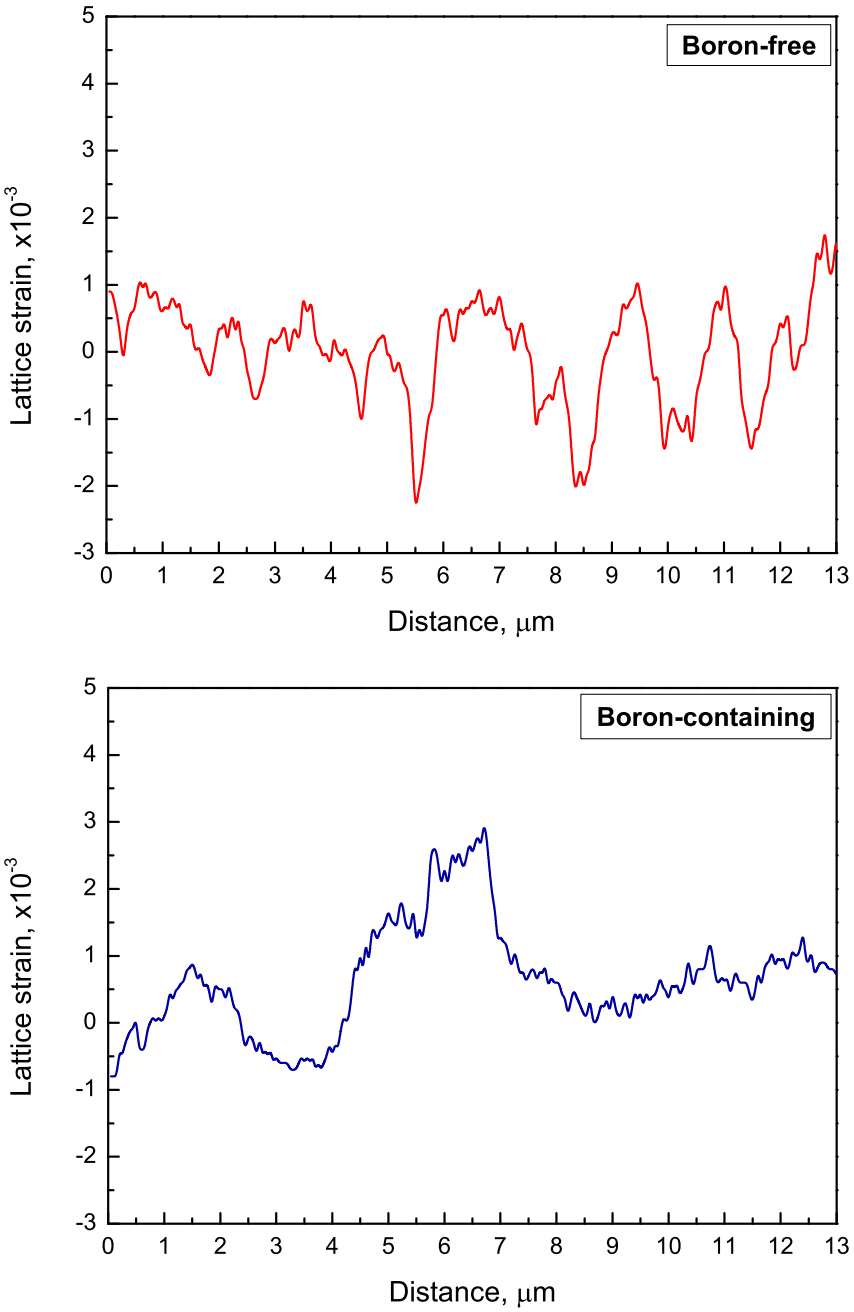


Figure 5.11: Lattice strain line-scans across the grains as denoted by the red lines in Figures 5.3(b) and 5.4(b) for the boron-free and boron-containing, respectively.

5.5.2 Crack Initiation and Propagation

The EBSD analysis has shown that a transition from planar to serrated grain boundaries can be achieved by the minor addition of boron. Serrated grain boundaries can dramatically improve mechanical properties by retarding crack growth, impeding cavity link and increasing the propagation path along the grain boundaries [142]. This study adds that at the lowest investigated strain rates, it is evident that voids form at incoherent interfaces along the grain boundaries, as observed in Figures 5.9 and 5.10. At those particular sites, the catastrophic combination of stress concentration and oxidation at the grain boundary regions leads to intergranular failure.

In the case of the boron-free alloy, voids form at the interfaces of between the $M_{23}C_6$ particles and the γ/γ' microstructure. Due to the planar character of the grain boundary, voids can interlink somewhat easier, forming a continuous intergranular crack path. By contrast, in the case of the boron-containing alloy, it is more difficult for the voids that have formed at grain boundaries to interlink. Thus, crack propagation is must be retarded in the boron-containing alloy. However, voids were found to initiate between the M_5B_3 borides and the γ/γ' microstructure, when the borides are at the segments of the grain boundary perpendicular to load axis. This observation can rationalise the creep performance of the high boron variant of STAL15-CC in Chapter 4; excess of borides at the grain boundaries will not further improve the mechanical properties.

Subsurface characterisation of deformed specimens has also been performed to further substantiate the HR-EBSD and microstructure observations made on the surface. In particular, the boron-containing specimen was sectioned using a dual column FIB instrument. Figure 5.12 illustrates a serrated grain boundary tested at 750 °C and strain rate $2\times10^{-5}\,s^{-1}$; note the load axis is in the horizontal direction.

It is shown that the crack propagates at the interface perpendicular to tensile axis and its propagation is retarded when it reaches the part of the grain boundary not perpendicular to the tensile axis (arrow 1). A second void can also be seen forming far from the surface of the specimen without interlinking with the main crack (arrow 2). Note that the second void forms at the grain boundary segment perpendicular to tensile axis.

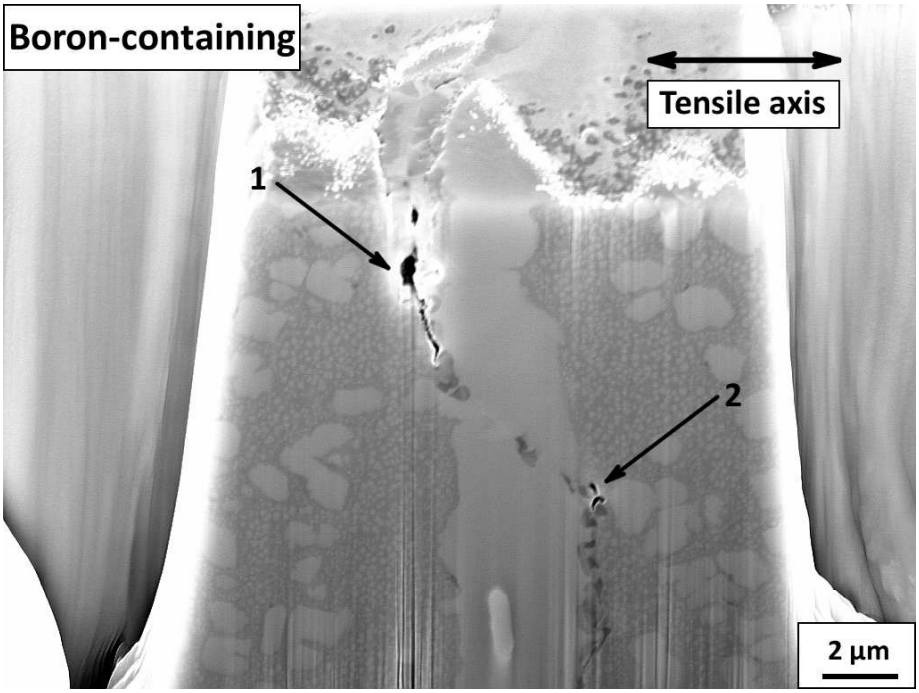


Figure 5.12: SEM image of FIB-section of a serrated grain boundary tested at 750 °C and strain rate 2x10^{-5} s^{-1}. The arrows indicate voids at interfaces perpendicular to tensile axis. Continuous crack path is not observed.

In addition, γ' layers form along the grain boundaries driven by the reduction in total interfacial energy, which has been shown to locally increase by the presence of boron [143]. The γ' layers can prevent the accumulation of plastic deformation at the interfaces between MC and γ/γ' microstructure and thus retard crack initiation at these specific sites. This beneficial effect of γ' layers will be more pronounced at

temperatures lower than 750 °C, when the MC carbides exhibit low ductility.

5.5.3 The Importance of Boron as Grain Boundary Element

As it was mentioned earlier in Chapter 4, there is much of evidence to support the idea that boron rather than carbon is the most crucial grain boundary strengthener in nickel-based superalloys. It was shown that minor additions of boron are beneficial to the mechanical properties by controlling the grain boundary character *i.e.* suppression of $M_{23}C_6$ carbides and precipitation of M_5B_3 borides and formation of serrated grain boundaries. By contrast, the addition of carbon and the subsequent formation of various carbides (MC, $M_{23}C_6$) and their effect on superalloys still remains controversial among researchers [116].

In this study, excessive cracking of MC carbides during the *in-situ* tensile tests to failure at 750 °C was not observed for both alloys. However, these tests last no longer than 2 hours, so the stability of MC carbides cannot be completely evaluated. It is well known that MC carbides oxidise faster than the γ/γ' microstructure and surface eruptions occur as a result of the oxidation in flat unstressed specimens [144–146]. Considering these factors, flat polished and unstressed samples from both boron-free and boron-containing alloys were exposed at 750 °C for 50 hours.

Similar observations as above were made in this current study, as illustrated in Figure 5.13(a). MC carbides oxidise causing surface eruptions in the polished unstressed boron-free and boron-containing specimens exposed at 750 °C for 50 hours. Such volume expansion can cause locally high stress concentrations to a region with pre-existing strains around MC carbides due to heat treatment, leading eventually to the formation of microcracks. Besides, porosity around the oxidised MC carbide was observed as shown in Figure 5.13(b). It is thus suggested that during over prolonged

exposure times, MC carbides can serve as location for crack initiation, particularly when they reside at grain boundaries where diffusion-driven phenomena are present. The effect of MC carbides on the mechanical properties of superalloys is further investigated in Chapter 6.

Moreover, secondary SEM micrographs of FIB-sections from the specimens exposed at 750 °C for 50 hours revealed γ' denuded zones along the grain boundaries of the boron-free alloy. Besides, no $M_{23}C_6$ carbides were found at least in a depth up to 7 μm as it can be seen in Figure 5.14(a). By contrast, in the boron-containing alloy γ' denuded areas were not observed; M_5B_3 were present as illustrated in Figure 5.14(b). The occurrence of areas susceptible to early fracture at elevated temperatures such as the γ' denuded zones is clearly undesirable, particularly when they form in such short times. In addition, first-principles calculation have shown that the Ni/M_5B_3 interfaces are more resistant towards O-embrittlement than coherent Ni/Ni_3Al interfaces [147].

It is therefore suggested that the precipitation of borides is more preferable than the precipitation of $M_{23}C_6$ carbides, in order to achieve a more stable microstructure and grain boundary character. In summary, it is clear that the addition of boron is more crucial for nickel superalloys designed for power generation applications, whilst lower carbon levels that provide a smaller MC volume fraction can potentially improve their mechanical properties.

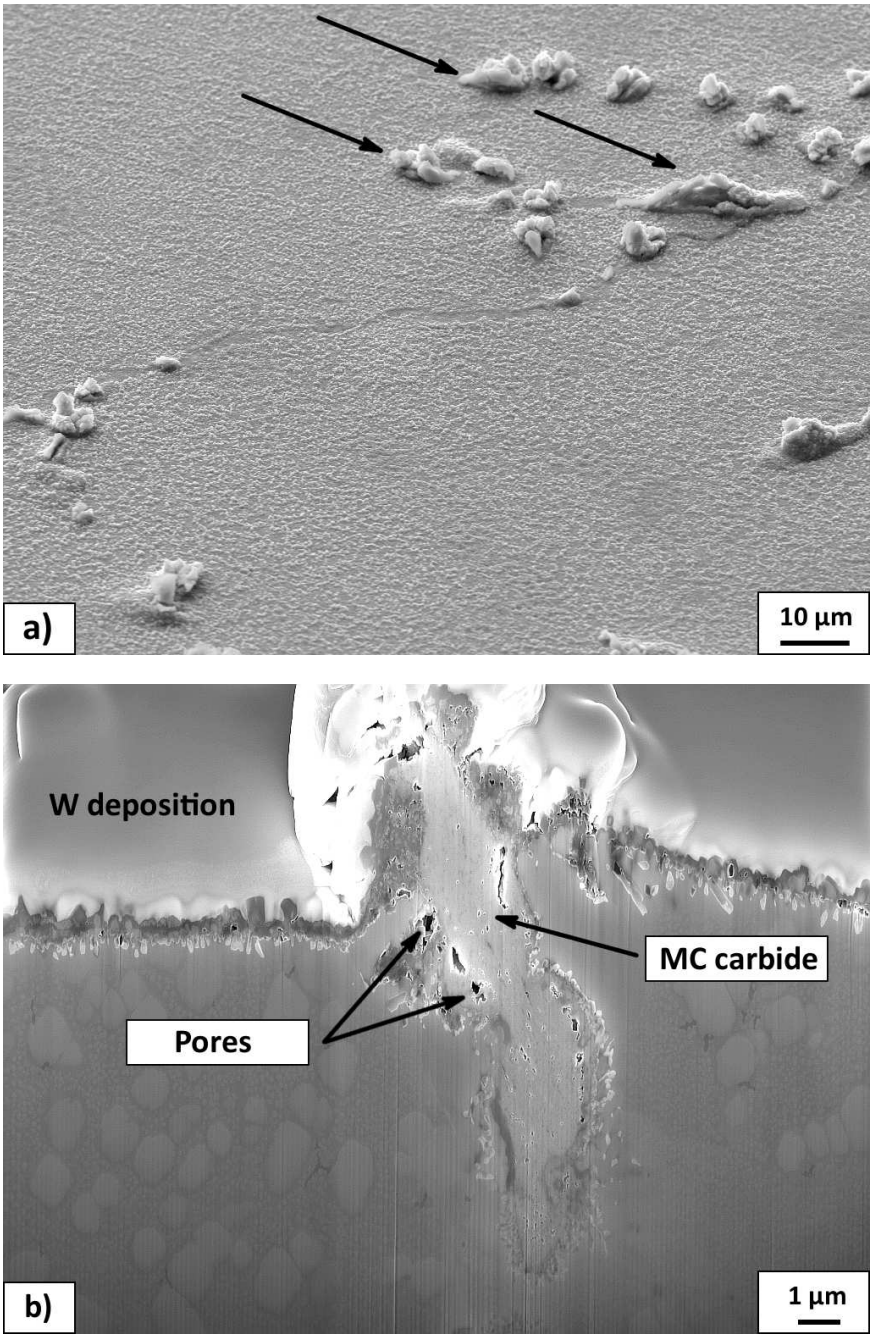


Figure 5.13: Secondary SEM images showing: a) surface eruptions due to the oxidation of Ta-rich MC carbides as indicated by the arrows and b) FIB-section of oxidised MC carbide from the boron-containing alloy exposed at 750 °C for 50 hours, showing pores related with the oxidised MC carbide.

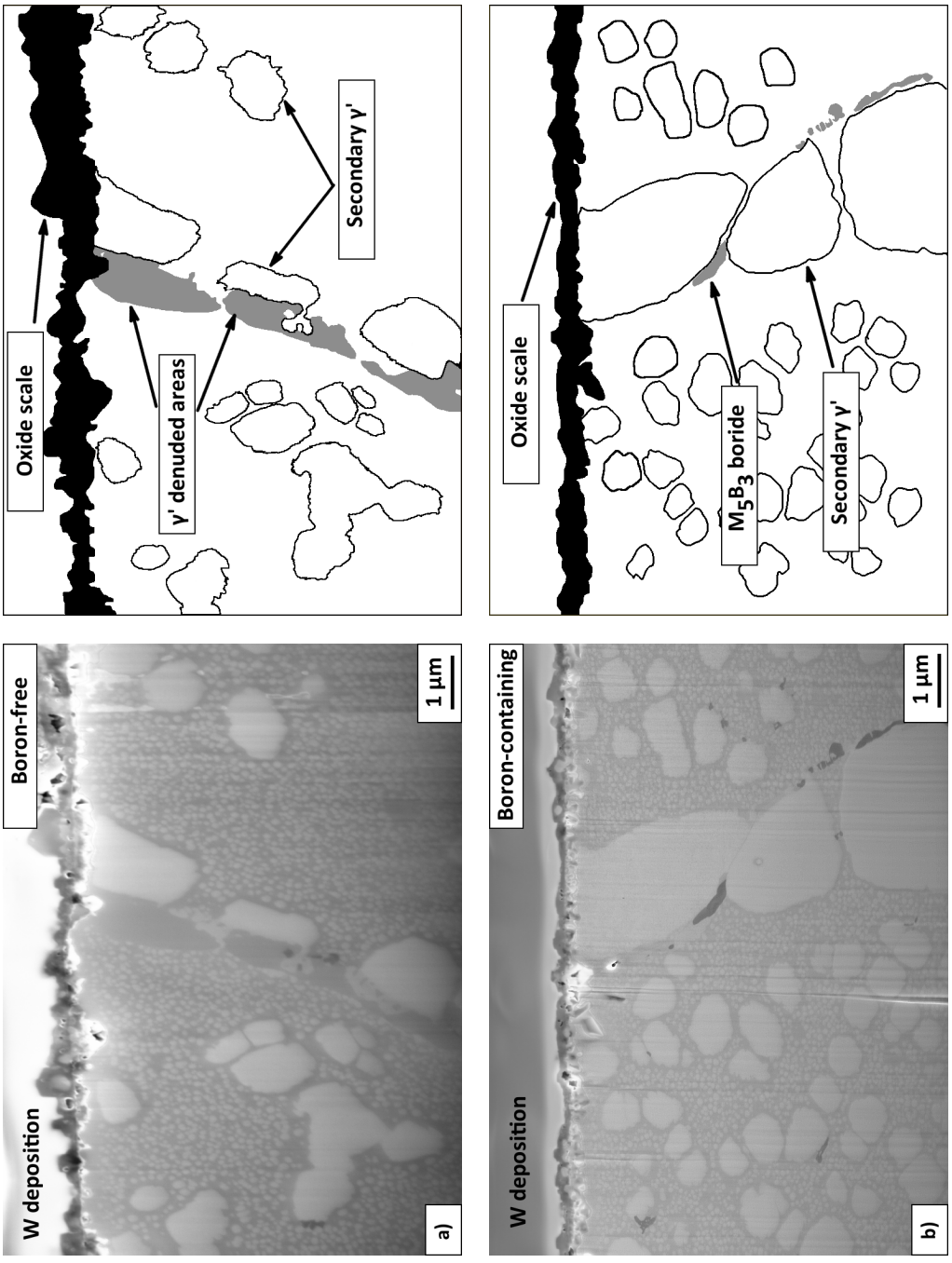


Figure 5.14: SEM figures of FIB-sections from grain boundary regions of: a) boron-free and b) boron-containing alloys exposed at 750 °C for 50 hours, alongside corresponding descriptive schematic illustrations.

5.6 Summary and Conclusions

The mechanical behaviour at elevated temperature of a prototype nickel-based superalloy has been studied, with emphasis on the improvement in ductility conferred by boron. Use is made of a miniaturised electro-thermal mechanical testing system and an *in-situ* SEM testing module with complimentary HR-EBSD strain mapping analysis. The following specific conclusions can be drawn:

- With boron present, the formation of serrated grain boundaries is promoted for random high-angle grain boundaries; by contrast the grain boundaries are of more planar form when boron is absent.
- Serrated grain boundaries exhibit an average wavelength of 3.7 μm and amplitude of 1.3 μm. No correlation between the misorientation and the magnitude of serration was observed.
- *In-situ* tensile tests at 750 °C confirm the formation of voids preferentially at segments of grain boundaries perpendicular to the tensile axis, but boron addition and grain boundary serration retard void formation and propagation.
- High-resolution EBSD strain mapping indicates uniformly distributed lattice strains across the grains in the boron-free alloy. By contrast, higher residual elastic strains were observed at the segments of grain boundary being serrated in the boron-containing alloy.
- Although residual thermal strains were revealed around MC carbides after heat treatment, excessive cracking of MC carbides at 750 °C was not observed by *in-situ* observations. However, void formation and local high stress concentration

is caused by the the rapid oxidation of the MC carbides at 750 °C after 50 hours.

Chapter 6

The Effect of MC Carbides on Thermal–Mechanical Fatigue of a Polycrystalline Superalloy

6.1 Introduction

Resistance to thermal-mechanical fatigue (TMF) is becoming of increasing importance to hot components for gas turbines, most notably when large temperature gradients exist from engine start up or shut-down. These yield complex stress and temperature cycles in turbine blades and vanes, and hence TMF damage may be prevalent. In addition, the advanced cooling systems used in steady-state operation also produce temperature gradients that may also result in TMF damage [148].

It is well known that a number of different methods are available for monitoring

crack growth rates when the temperature is isothermal. However, very few studies report on crack initiation and propagation behaviour during thermal cycling and in particular when a dwell period is used. As a consequence, our knowledge around the microstructural factors influencing the TMF performance of polycrystalline superalloys under such complex conditions is limited. This situation has provided the motivation for the present study. Here, new insights into the effects occurring under such conditions are sought. Apart from the high scientific interest, there is also significant industrial relevance; the service life of many hot components is not entirely controlled by the number of cycles to crack initiation, consequently a certain amount of crack propagation may occur prior to component replacement. In this case, prediction schemes for crack growth rates need to be accurate [149].

6.2 Background

The start-up and shut-down procedures of the turbine engine result in temperature gradients which need to be taken into account for the evaluation of mechanical properties of nickel superalloys. The traditional isothermal fatigue tests, for instance low cycle fatigue (LCF) tests, cannot be accurate for the investigation of these temperature gradients and their effect on fatigue performance. For instance, the TMF life of a single crystal superalloy is half of that of LCF life [150]. Thus, by conducting TMF tests the influence of temperature and stress cycling can be studied in detail.

During TMF tests, different microstructural features such as carbides can influence TMF performance and particularly crack initiation and propagation. In particular, the MC-type carbides were suggested to serve as the main crack initiation sites under TMF conditions; mainly due to their brittle nature and high oxidation rate [151–155]. However, the exact role of the carbides is not well understood under

IP and OP-TMF conditions and this is the subject of this Chapter.

In-Phase (IP) and Out-of-Phase (OP) are the most common types of TMF cycles. Figure 6.1 illustrates schematic graphs of stress *vs.* strain during IP and OP tests. In the case of IP-test, creep relaxation at the maximum temperature occurs in tension and plastic deformation takes place in compression at the cold part of the cycle. Cold-spot areas such as cooling holes or structures inside the cooling channels of the hot components of the engine are subjected to such conditions; the temperature at these parts is typically lower compared to the surrounding area.

By contrast, at the OP-tests creep relaxation at the maximum temperature occurs in compression and plastic deformation in tension. Such conditions can be found at parts of turbine blades (platform of the blade) for instance which suffer from insufficient cooling; the so-called hot-spot areas. Normally, a dwell time is applied at the maximum temperature part of the TMF cycle, in order to reproduce conditions similar to those an industrial turbine is subjected to. Dwell time can vary from several seconds to couple of hours in the lab, however the average time between start and stop can be up to 500 hours [156].

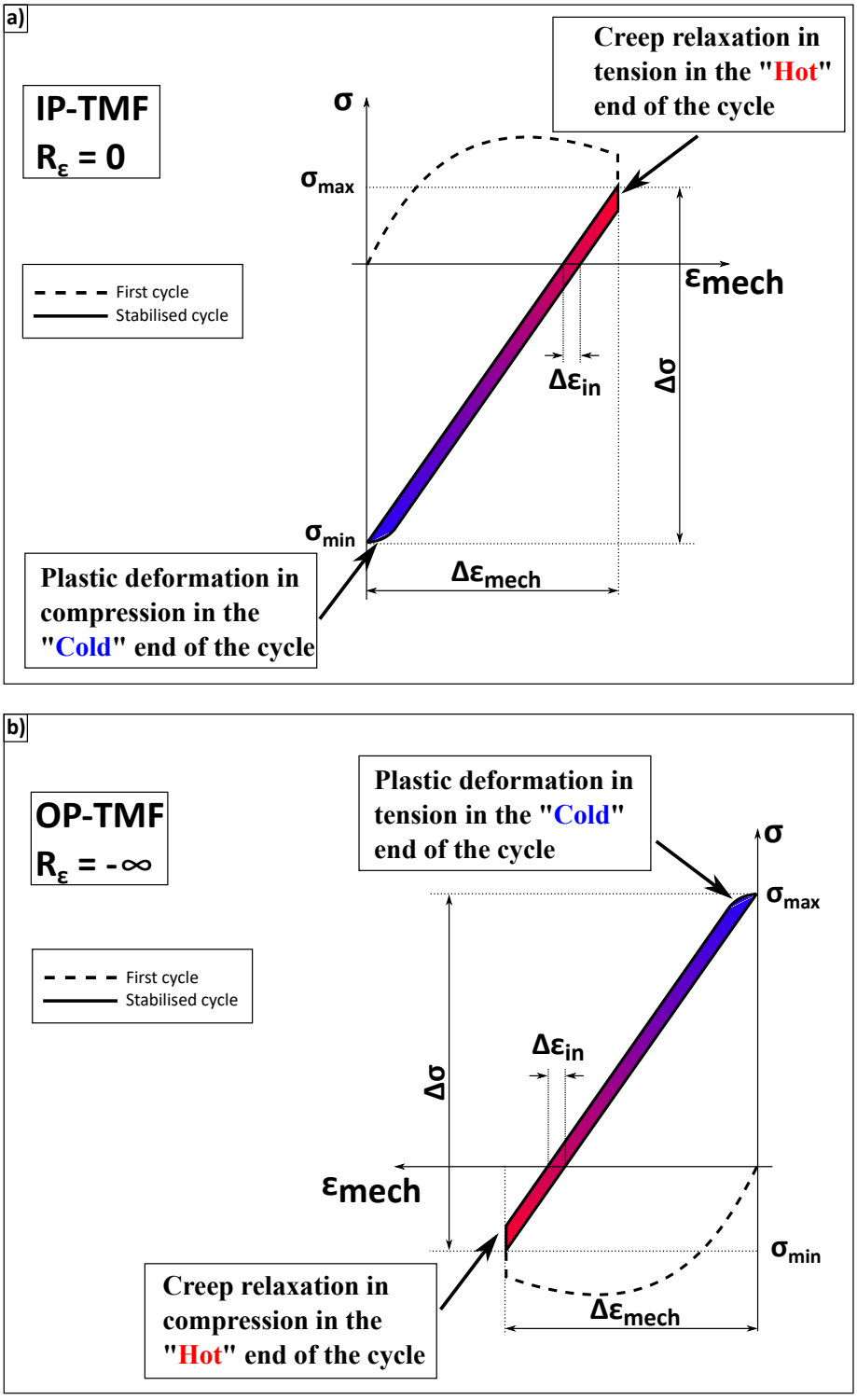


Figure 6.1: Schematic graphs of stress *vs.* strain during: a) In-Phase (IP) TMF and b) Out-of-Phase (OP) TMF [156].

6.3 Experimental Procedures

Both in-phase (IP) and out-of-phase (OP) thermal–mechanical fatigue cycling were conducted under mechanical strain control in the 100-750 °C temperature range using a MTS 810 servo-hydraulic thermal–mechanical fatigue machine; the experimental of which has also been described [157].

Single edge notched (SEN) type specimens were machined from fully heat-treated bars of IN792 with the geometry illustrated in Figure 6.2. To study the crack initiation sites and the crack propagation character during IP and OP-TMF, the specimens were sectioned parallel to the tensile axis as shown in Figure 6.2. Polished surfaces were prepared metallographically and observed by backscattered electron imaging and electron backscattered diffraction (EBSD). In addition, energy dispersive X-ray (EDX) chemical mapping was conducted using a Zeiss Merlin FEG-SEM.

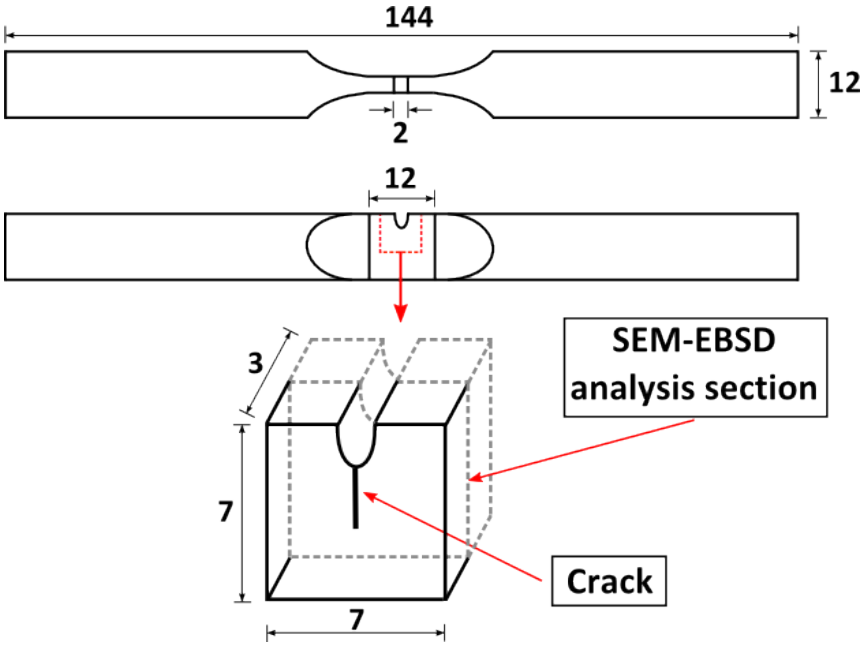


Figure 6.2: Geometry of single edge notched (SEN) type specimen.

An extensometer with a 12 mm gauge length was attached symmetrically to the specimen over the notch. All tests were conducted in displacement control by prescribing the displacement of the extensometer gauge length. In this work the displacement measured by the extensometer (ΔL) divided by the extensometer gauge length (L_0) will be referred to as the nominal total strain ($\epsilon_{nom}=\Delta L/L_0$). To enable thermal cycling, induction heating was used in combination with convection cooling from compressed air distributed onto the specimen by two cooling nozzles. To examine the effect of dwell time on TMF crack propagation, hold times of 5 and 360 minutes (6 hours) were applied at the maximum temperature. The test matrix is summarized in Table 6.1. Crack lengths were determined using the compliance method in a similar manner as outlined in ASTM E 647 for isothermal crack growth tests [149]. All tests were performed in laboratory air.

Table 6.1: IP and OP-TMF tests conducted in this study for the investigation of the effect of dwell-time during TMF.

Cycle type	**Dwell, min**	ϵ_{nom}, %
IP (R=0)	5	0.6
OP (R=-∞)	5	0.6
IP (R=0)	360	0.6
OP (R=-∞)	360	0.6

Finally, to investigate the effect of MC carbides on the TMF life, high resolution EBSD strain mapping was performed for the non-deformed and deformed specimens. The EBSD patterns were recorded following the conditions mentioned previously in Chapter 3.

6.4 Results

6.4.1 Crack Growth Rates

Data for crack length as a function of the number of cycles is summarised in Figure 6.3. Crack initiation occurred rather early in all tests and in all cases a significant number of cycles were consumed in crack propagation. A general observation was that the crack propagation rate decreased with increasing crack length, particularly after the length of the crack reached 1.5 mm. Note that for the OP test with a 5 minutes dwell, some data points are absent due to missed data logging during the test.

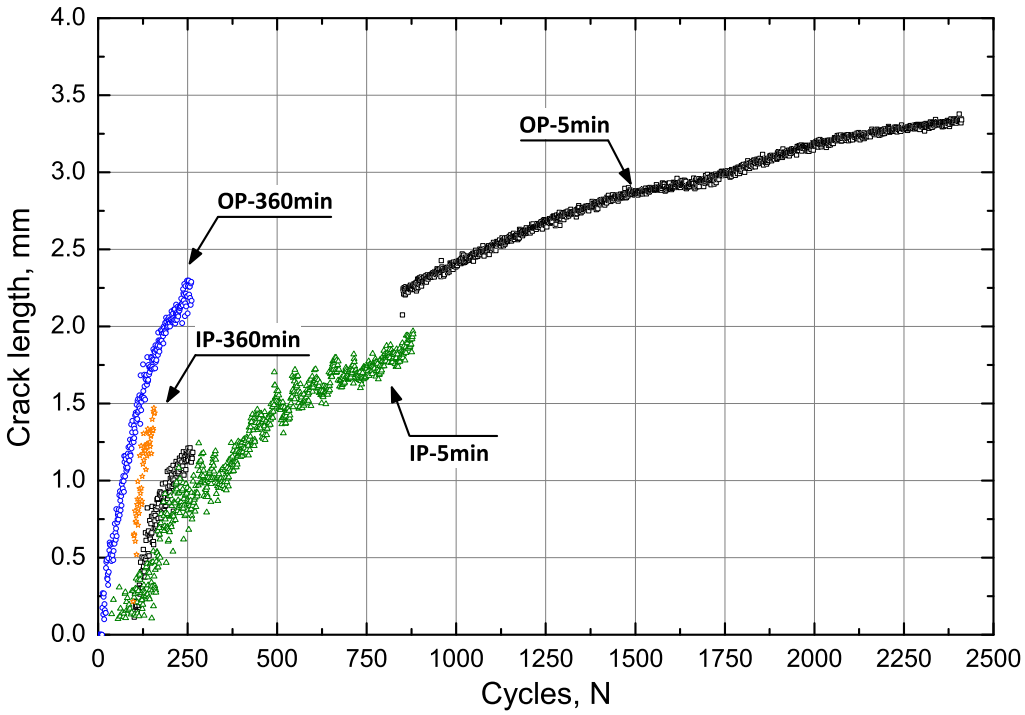


Figure 6.3: Crack length *vs.* number of cycles measurements for all the investigated TMF conditions for the IN792 alloy.

The crack growth rate is next calculated from the derivative of the crack length versus number of cycles (da/dN) data; the results of this procedure are plotted in Figure 6.4. It can be seen that the crack growth rate (da/dN) is slightly higher for the OP condition compared to IP, when the dwell time is 5 min. However, a dwell time of 6 hours at the highest temperature increases the crack growth rate dramatically in both IP and OP conditions; slightly higher crack growth rate was observed in the IP case with dwell.

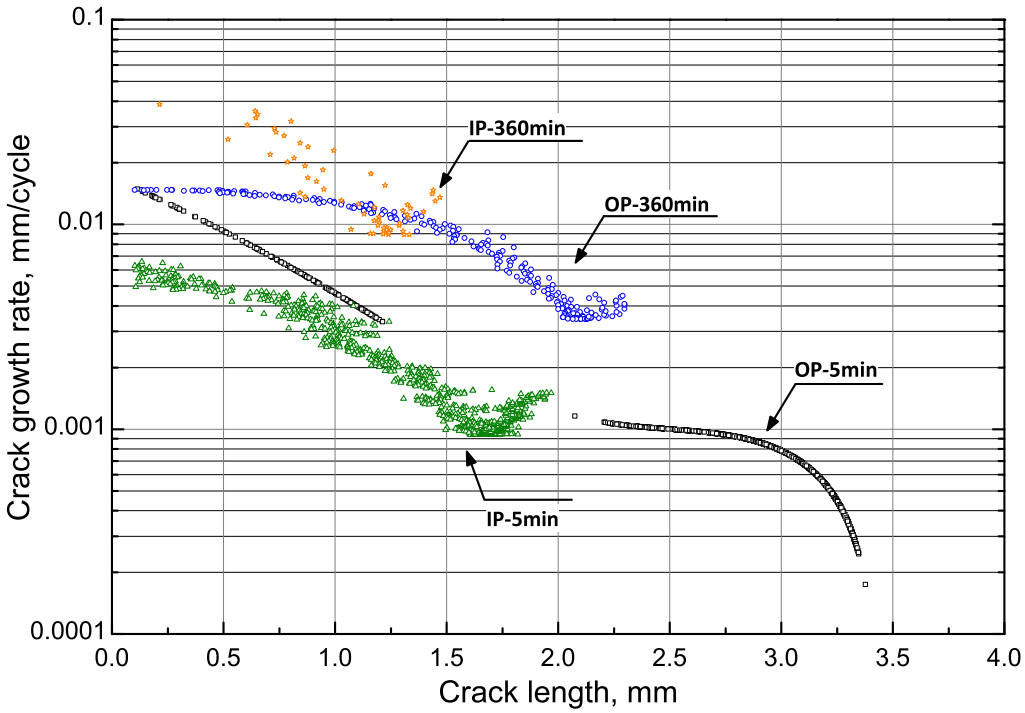


Figure 6.4: Crack growth rate *vs.* crack length graph for all the investigated TMF conditions.

The above observation can also be observed in Figure 6.5, where the crack growth rate is plotted as a function of maximum stress intensity factor. Under the assumption that linear fracture mechanics is valid at elevated temperatures, the

stress intensity factor is defined as:

$$K_I = Y\sigma\sqrt{\pi\alpha} \tag{6.1}$$

where K_{I} is the stress intensity factor, Y is the geometry factor and a is the crack length. A relationship between the stress intensity factor, the crack length and the applied force for the particular specimen geometry used in the current study has been established previously [149]. From Figure 6.5 it is apparent that a 6 hours dwell has dramatically affected the crack growth rate in the IP-tests, whereas the crack growth rate in the OP case remains evident but its influence is weaker. When the results from IP and OP with 6 hours dwell are compared, a relatively higher crack growth rate is observed for the IP-test.

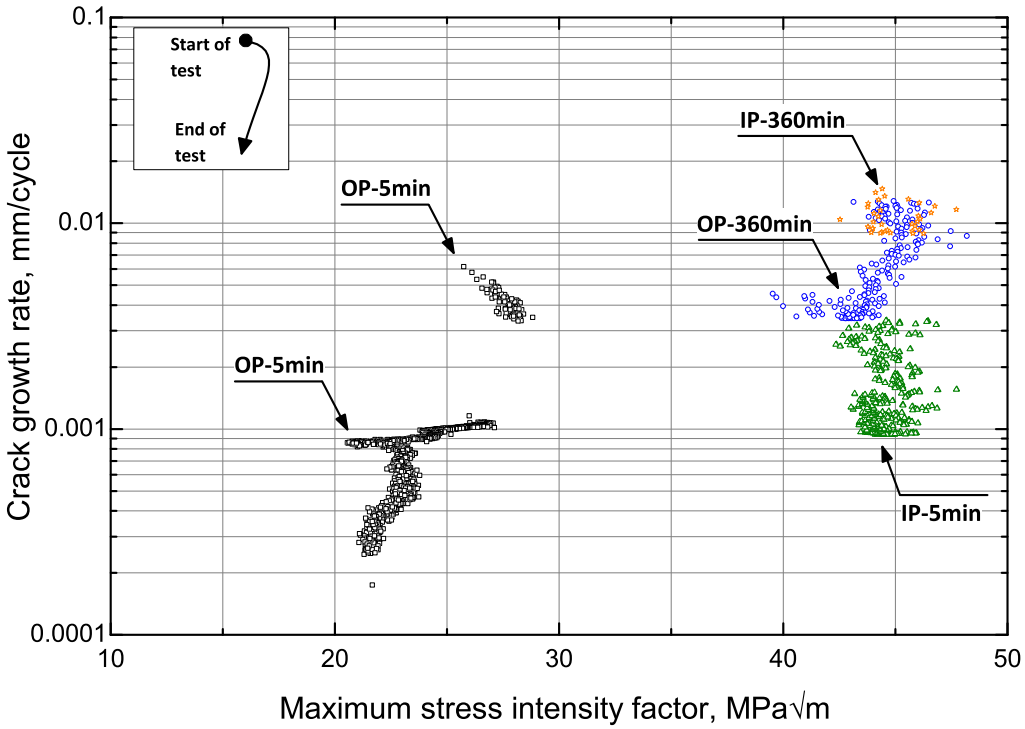


Figure 6.5: Crack growth rate as a function of the maximum stress intensity factor for all the investigated TMF conditions.

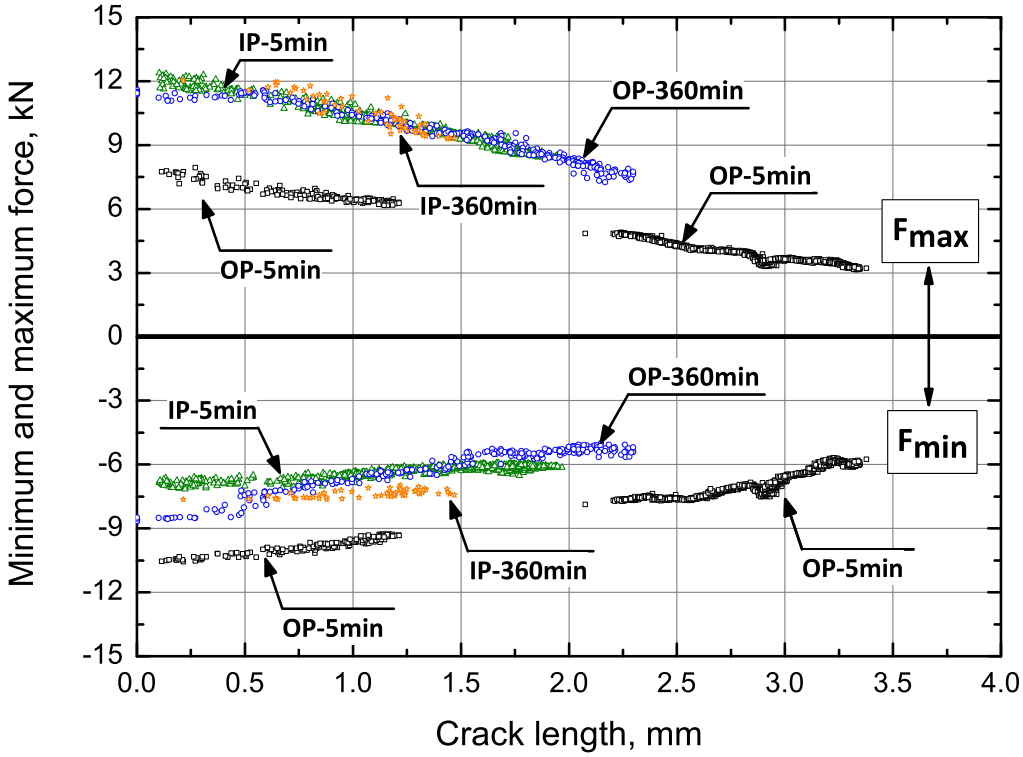


Figure 6.6: Minimum and maximum force *vs.* crack length graph for all the investigated TMF conditions.

Figure 6.6 illustrates the minimum and maximum forces as a function of crack length, respectively. Since the tests were performed in displacement control, the force response will change as the length of the crack increases, as observed. In addition, it can be seen that in the case of the 5 minutes dwell tests, the maximum force in the IP-case is relatively high compared to the OP-test. However, for the 6 hour dwell test, the maximum force in the OP-test increases substantially; similar behaviour is not observed for the IP-test.

6.4.2 Crack Initiation

In IN792, it would appear that the TMF crack initiation life is controlled by the MC-type carbides which have precipitated inter- and transgranularly. Cracks growing due to oxidation damage from the surface and through the γ' denuded zone caused by it also need to be taken into account. Table 6.2 summarises the parameters found to influence the crack initiation life of IN792 at all the investigated conditions.

In the case of the IP-tests, the MC carbides are considered to have a rather detrimental effect on the crack initiation life. In particular, for the IP-test with a 5 minutes dwell the majority of the MC carbides were observed to have cracked. In addition, voids formed at the MC and γ/γ' interfaces, as illustrated in Figure 6.7(a).

As dwell time increased under IP conditions, the cracks were found to initiate primarily at grain boundaries. However, the MC carbides still exhibit similar behaviour as previously. It is believed that the observed brittle nature of MC carbides combined with longer dwell times are responsible for the transition to intergranular crack initiation. Figure 6.7(c) illustrates voids forming at grain boundaries and at the grain interior, particularly at the interfaces between MC and matrix (γ/γ') microstructure.

Table 6.2: Summary of crack initiation sites for all the investigated conditions.

	IP-TMF	**OP-TMF**
5 min dwell	MC carbide cracking	Oxidised MC carbide close to surface
360 min dwell	Voids forming at grain boundaries/MC carbide cracking	Oxidised MC carbide close to surface

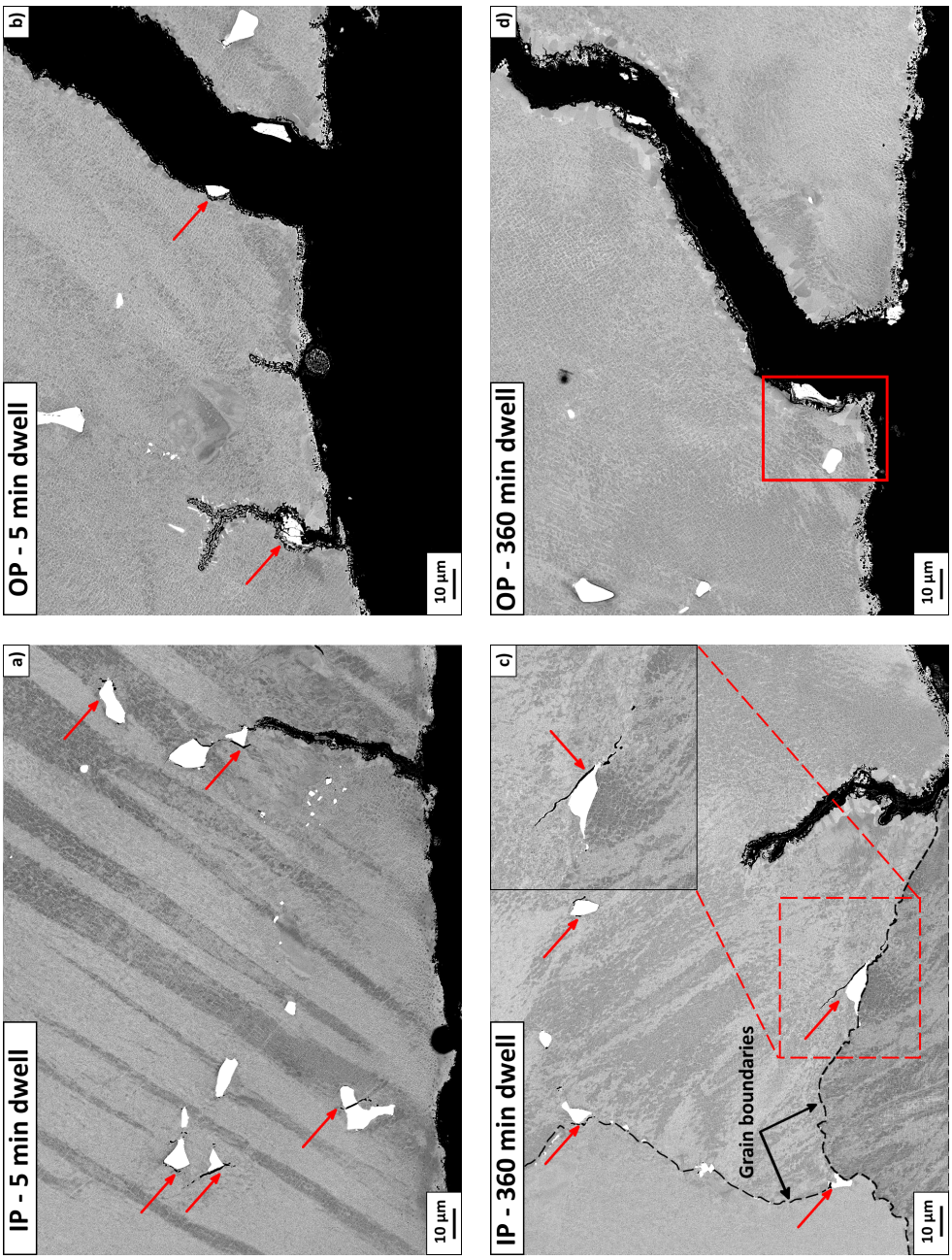


Figure 6.7: Backscattered SEM images of the crack initiation sites of: a) IP–5 minutes dwell, b) OP–5 minutes dwell, c) IP–360 minutes dwell and d) OP–360 minutes dwell specimens. Load axis is in horizontal direction. Red box denotes the area scanned for EDX mapping (see Figure 6.10). Arrows indicate voids around MC carbides.

Although the crack initiation sites can be related to oxides forming from the surface, the fact that the majority of MC carbides are cracked at the IP-tests is the prevailing observation, the formation of voids at these particular interfaces in the IP-tests dramatically decreases the crack initiation time of the alloy. MC carbides have been reported to serve as crack initiation sites in previous studies on polycrystalline superalloys particularly during isothermal fatigue studies [158–160].

In order to rationalise the void formation at the MC/matrix interfaces during IP-testing, strain mapping analysis was conducted for both IP-tests and close to MC carbides. Figure 6.8 illustrates the investigated MC carbide close to the crack tip alongside corresponding strain maps in the case of IP-test with 6 hours dwell. The accumulation of plastic deformation around the MC carbide is apparent from the backscattered image (dark contrast regions) and it is also confirmed by the geometrically necessary dislocation (GND) density measurements, as illustrated in Figure 6.8. This is expected due to the presence of high strain gradients at the interface of MC and γ/γ'. If accumulation of plastic deformation around MC carbides occurs relatively soon compared to oxidation damage in the IP-tests, then the MC carbides will serve as the predominant sites for crack initiation, and it is believed this to be the case here.

Note that due to the unknown elastic constant of the MC carbide, these regions have not been included in the cross-correlation analysis routine. These regions, in addition to any point of low diffraction pattern quality have been omitted in Figures 6.8, 6.9 and 6.12.

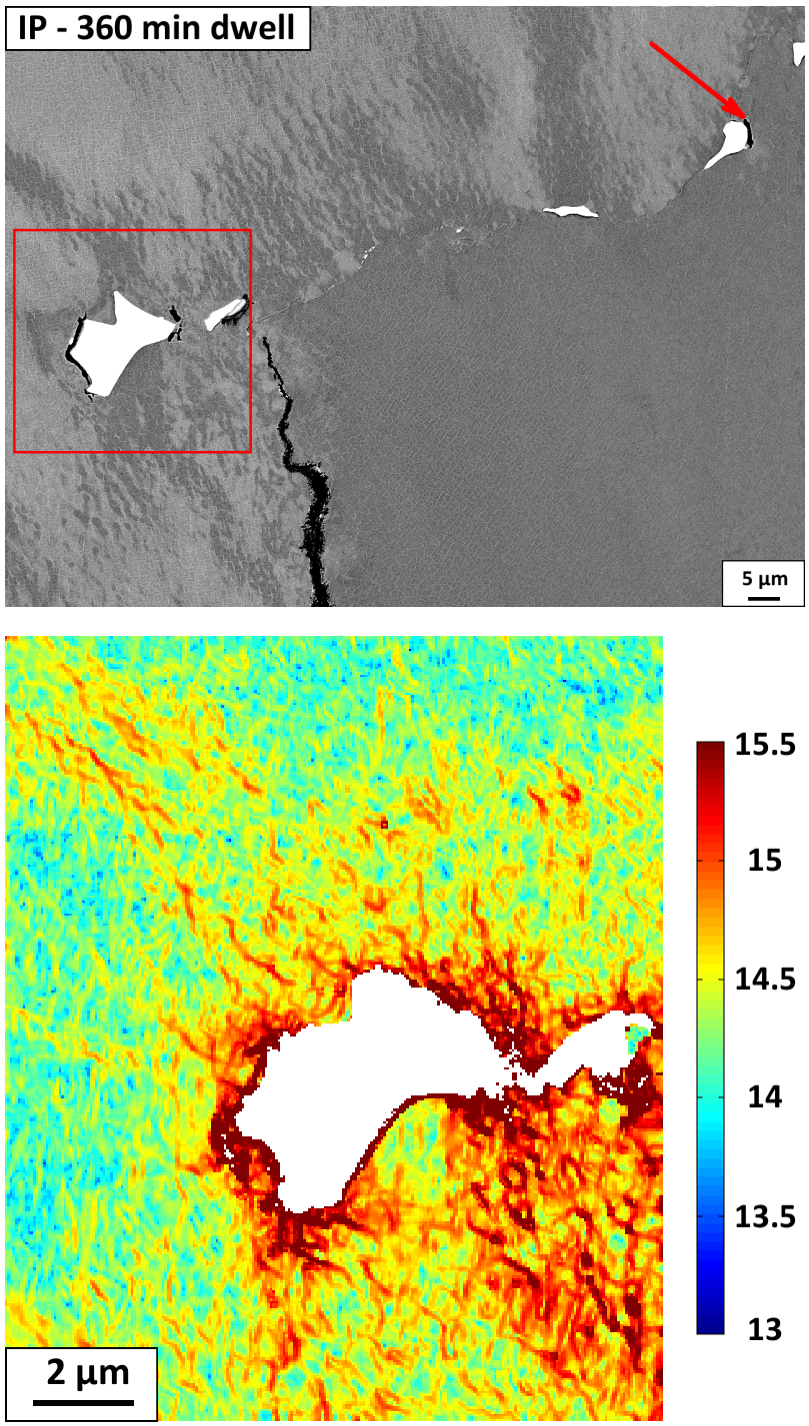


Figure 6.8: Backscattered SEM image of cracked MC carbide at the vicinity of main crack tip of IP-test with 6 hours dwell and corresponding geometrically necessary dislocations (GND) density map with the scale bar in $\log_{10}$ scale of dislocation lines m^{-2}. Load axis in the horizontal direction. The arrow indicates void at MC carbide ahead of the crack tip.

Moreover, Figure 6.9 illustrates a backscattered SEM micrograph from a carbide from the IP test with 5 minutes dwell. Large lattice rotations can be observed in the vicinity of voids, corresponding to regions of high dislocation density shown in the GND map. It is apparent that MC carbides cannot accommodate plastic deformation and thus voids initiate at the interface of MC with matrix (γ/γ') microstructure.

Similar behaviour of the MC carbides was not observed in the case of OP testing. In particular, for the OP-tests, it was not found that the MC carbides were cracked or the MC/matrix interfaces were damaged; such observations were very rare. However, for OP-testing, with 5 and 360 minutes dwell time, cracks were found to initiate primarily at regions where transgranular MC carbides were oxidised close to the surface. Figures 6.7(b) and 6.7(d) illustrate the crack initiation sites for the OP-tests with 5 and 360 minutes dwell time, respectively.

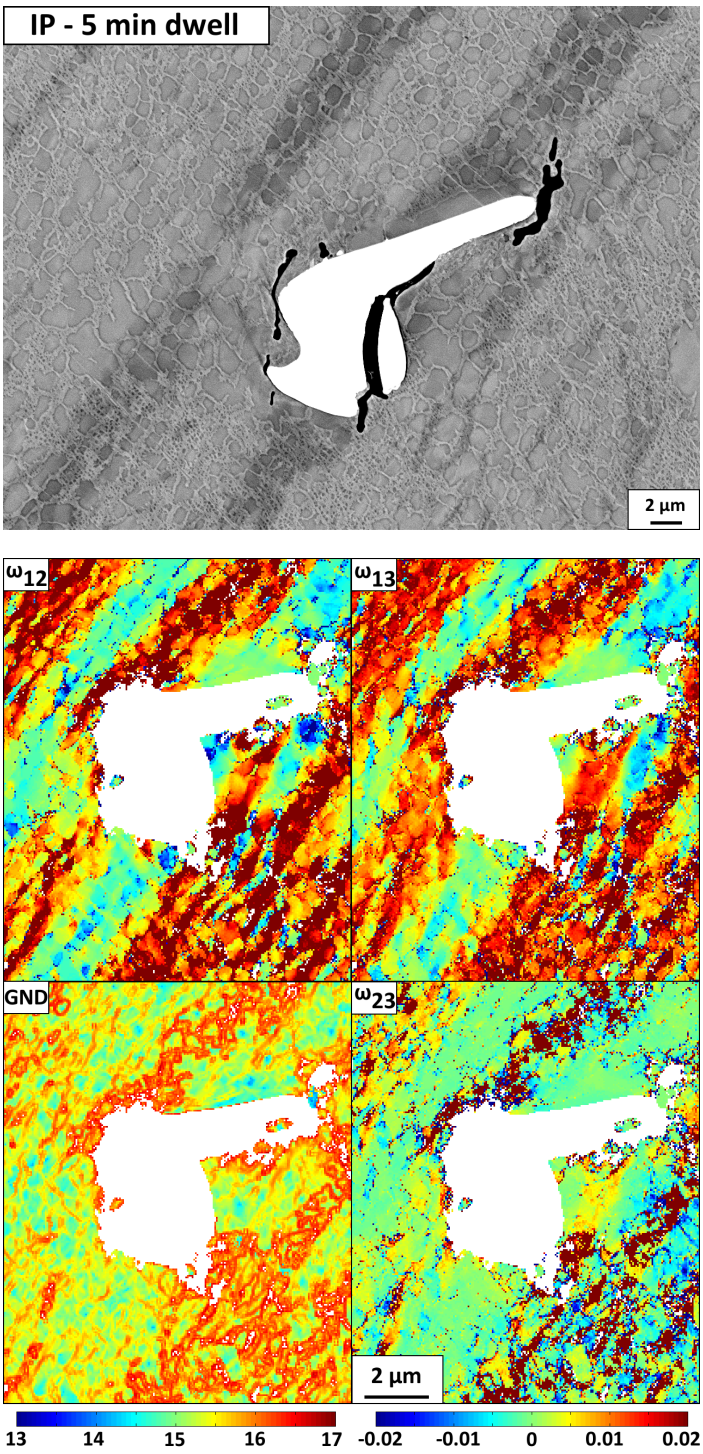


Figure 6.9: Backscattered SEM image of cracked MC carbide from the IP-test with 5 minutes dwell, with corresponding lattice rotation maps (rotations in radians) and geometrically necessary dislocations (GND) density map with the scale bar in $\log_{10}$ scale of dislocation lines m^{-2}. The in-plane rotation ω_{12} and the out-of-plane rotations ω_{13} and ω_{23}, rotating about the 2 and 1 axis respectively are shown.

Figure 6.10 illustrates EDX maps collected from the crack initiation site of the OP-test with 6 hours dwell (see Figure 6.7(d)). The oxidised Ta/Ti-rich MC carbide can be observed at the crack and it is denoted by the red arrow in the Ta map. At the C map, the position of the oxidised carbide is denoted by the white dashed line; note that the brightest red area is due to the surrounding mounting material.

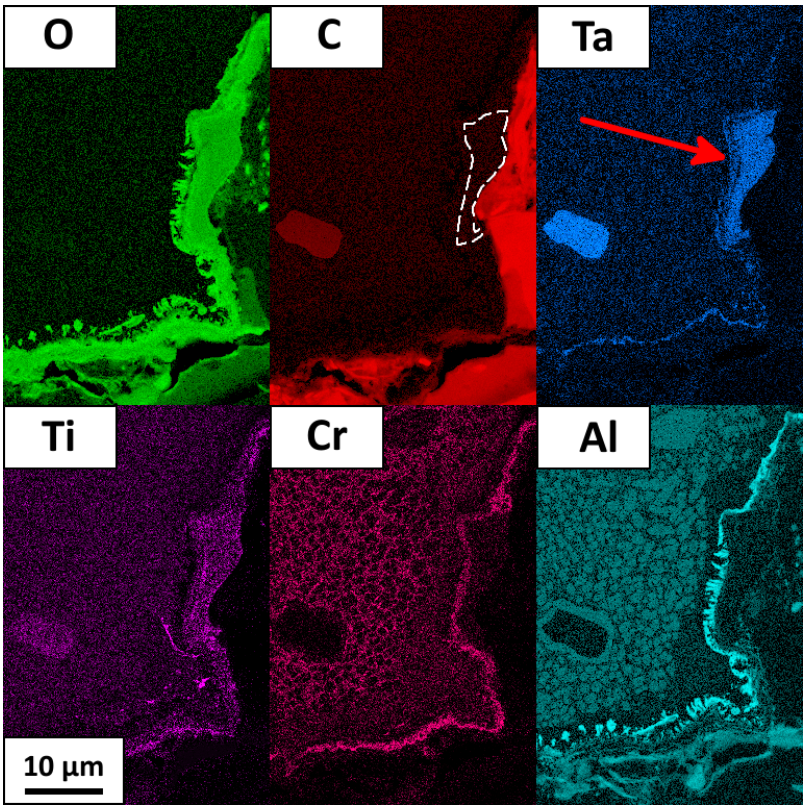


Figure 6.10: EDX chemical mapping of the crack initiation area as denoted by the red box in Figure 6.7(d). The crack propagates in the perpendicular direction and the red arrow indicates the oxidised (Ta,Ti)C carbide and the white dashed line shows the position of the carbide at the C map.

Based on the above microstructural observations, one would expect that the crack initiation life of IN792 would be shorter under IP conditions compared to OP. Table 6.3 summarises the cycles to crack initiation for all the investigated conditions. Crack initiation was defined as the number of cycles required to grow a crack

of 100 μm length. Indeed a shorter crack initiation life was obtained for specimens tested under IP conditions. Therefore, it can be suggested that the presence of MC carbides is relatively more detrimental under IP-TMF conditions, because accumulation of plasticity around the carbides leads to early fracture. But one can argue that further studies are needed to confirm this conjecture.

Table 6.3: Cycles to crack initiation for all the investigated conditions.

Cycle type	**Cycles to crack initiation**
IP - 5 min dwell	77
IP - 360 min dwell	82
OP - 5 min dwell	95
OP - 360 min dwell	102

6.4.3 Crack Propagation

Microstructural observations of the cracks for each investigated condition have shown that in the case of 5 minutes dwell time cracks, in both IP and OP conditions, propagate transgranularly as illustrated in Figure 6.11(a) and 6.11(b).

By contrast, 6 hours dwell time results in intergranular crack propagation in the case of the IP condition (Figure 6.11(c)); however crack propagation remains transgranularly in OP, as illustrated in Figure 6.11(d) and the corresponding EBSD inverse pole figure plot. Other studies on IN792 found similar behaviour for IP and OP tests between 100-750 °C [161]. All of the above observations have been confirmed by EBSD scans, as shown in Figure 6.11.

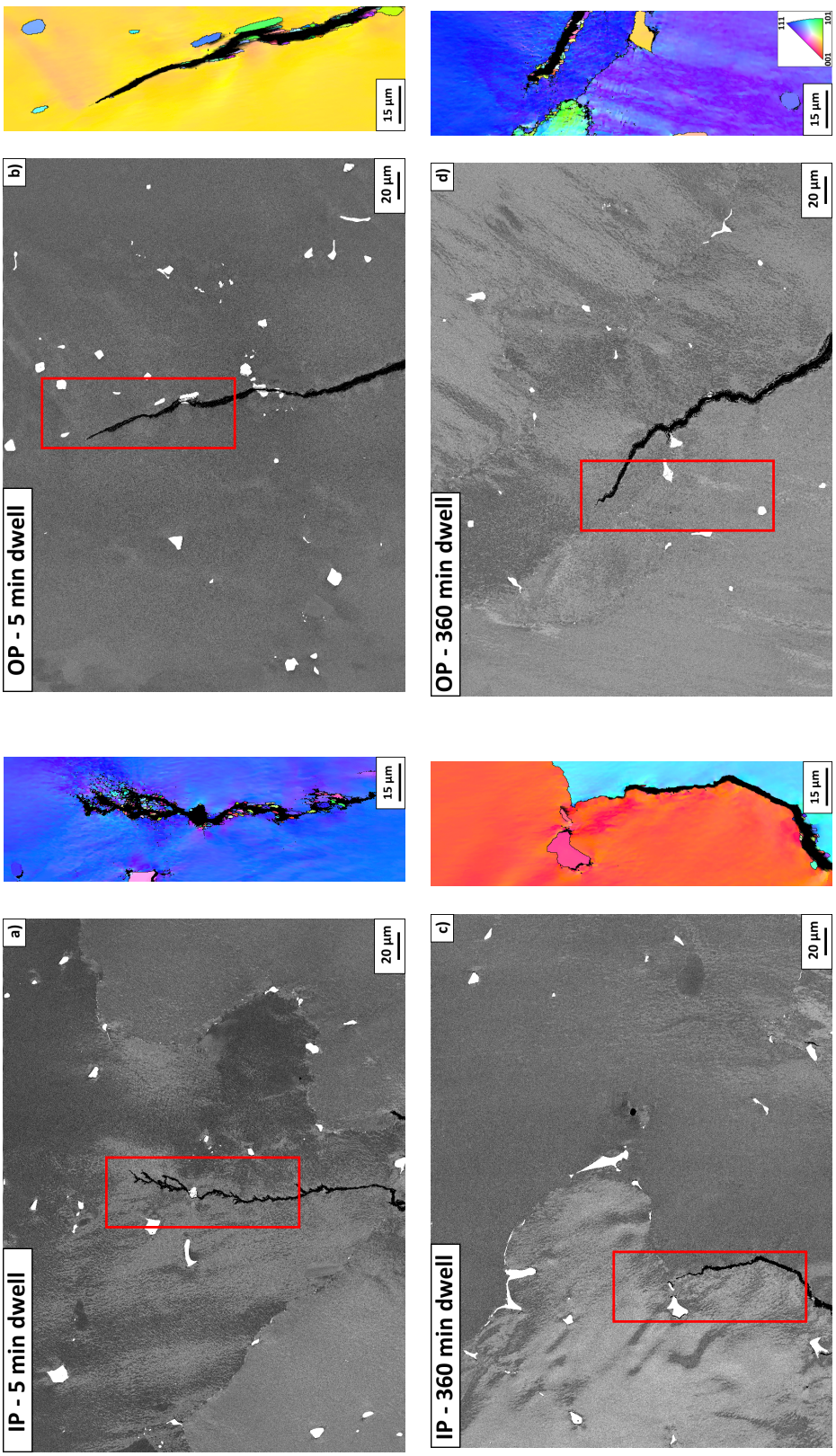


Figure 6.11: Backscattered SEM images showing the crack tips in: a) IP–5 minutes dwell, b) OP–5 minutes dwell, c) IP–360 minutes dwell and d) OP–360 minutes dwell specimens alongside corresponding EBSD inverse pole figures. Red boxes denote the scanned by EBSD areas and load axis is in horizontal direction.

6.5 Discussion

6.5.1 MC Carbides – Crack Initiation Sites

The main parameters influencing the crack initiation life of IN792 have been summarised in Table 6.2. These observations lead one to question the precise role of MC carbides and particularly carbon in polycrystalline superalloys, for high temperature applications. In addition to the post-mortem findings about the MC carbides, the EBSD strain mapping of the MC carbides in the fully heat treated microstructure raises further queries about the effect of MC carbides in these materials.

A backscattered SEM image of a grain boundary region after full heat treatment, prior to any deformation by fatigue, which contains two MC carbides are illustrated in Figure 6.12, alongside corresponding EBSD lattice strain maps. The red box indicates the particular area of the strain mapping analysis; two bright-contrast intergranular Ta/Ti rich MC-type carbides can be observed.

The strain mapping analysis revealed residual thermal strains around the MC carbides, after the full heat treatment and prior to any deformation. Residual strains can be seen at the top left-hand and bottom left-hand corner of the normal strain ϵ_{11} along the horizontal x axis map. Cooling from the ageing temperature combined with the differing thermal expansion coefficients between the MC carbides and the γ/γ' microstructure leads to the observed residual thermal strains. Similar behaviour has been observed previously in a directionally solidified superalloy containing MC carbides, in a polycrystalline nickel superalloy for disk applications containing non-metallic inclusions [139, 140] and in STAL15-CC in Chapter 5.

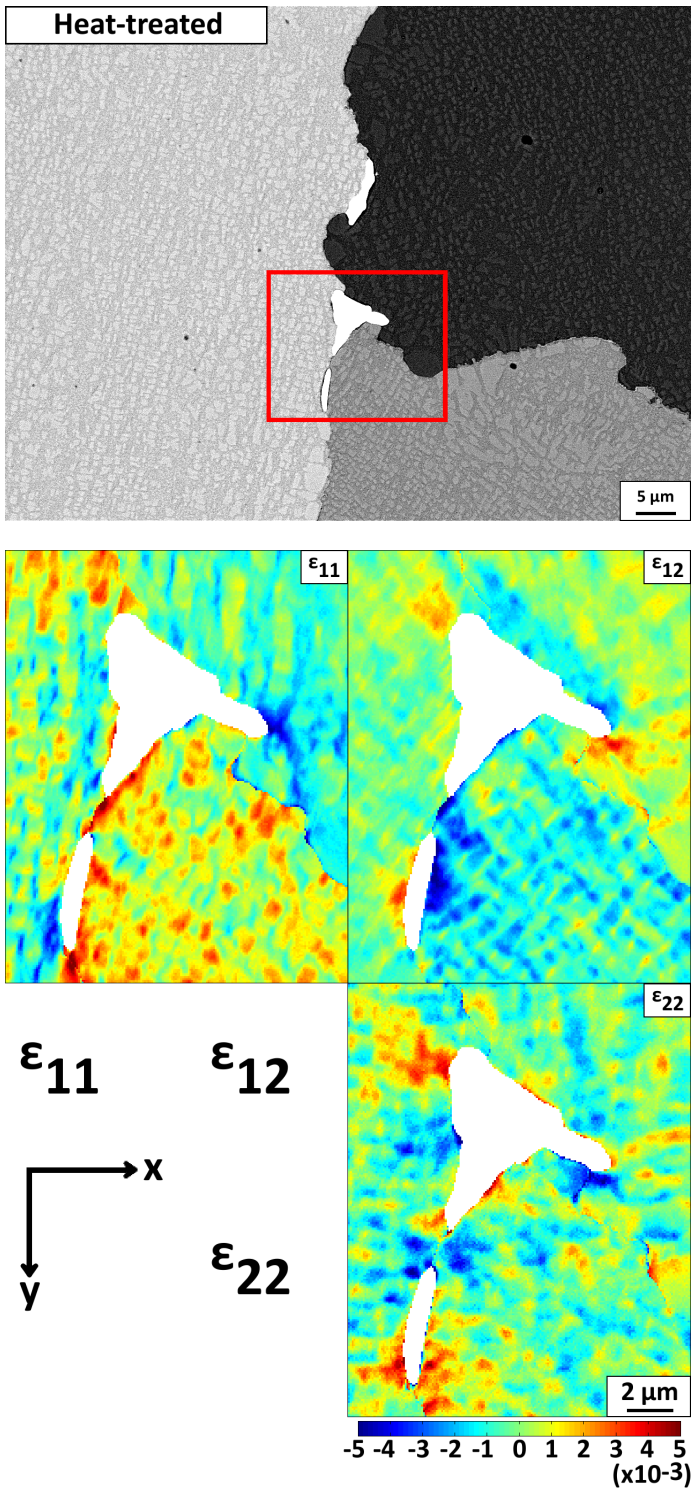


Figure 6.12: Backscattered SEM image of fully heat treated IN792 showing intergranular MC carbides and corresponding EBSD strain maps. The strain ϵ_{11} along the horizontal axis x, the in-plane shear strain ϵ_{12} and the strain ϵ_{22} along the vertical axis y are shown.

From all of the above observations, it would seem sensible to come to the conclusion that the optimal carbon content in polycrystalline superalloys must be important in determining fatigue performance [21]. For instance, the TMF crack initiation life might be potentially improved by decreasing the carbon content and subsequently lowering the volume fraction of MC carbides within the microstructure. Optimisation of the cooling process to minimise the residual thermal strains and the propensity for carbide cracking might also be important.

In the OP-tests, carbides were not observed to be cracked. However, cracks were found to initiate from oxidised MC carbides – see Figures 6.7(b) and 6.7(d). It is known that MC-type carbides oxidise faster than the γ/γ' microstructure [144]. Moreover, in a previous study the oxidation of MC carbides was found to result in surface eruptions in unstressed at polished specimens and that a substantial volume expansion occurs as a result of oxidation [145]. Similar observations were made for STAL15-CC alloy as shown in Chapter 5. Thus, localised plastic deformation around oxidising carbides occurs and thereby they serve as crack initiation sites. In the case of the OP-tests, the MC carbides oxidise during compression at the maximum temperature and subsequently crack in tension at the cold end of the cycle, when they exhibit low ductility.

Finally, one should acknowledge that the shape of the MC carbides may influence the crack initiation life. In particular, oxidising script-type MC carbides can serve as sharp oxide intrusions from which cracks can initiate. In the case of IN792, script-type MC carbides are not observed; blocky shaped MC carbides are dominant.

6.5.2 The Effect of Dwell Time on Crack Propagation

It was shown that the increase of dwell time dramatically increases the crack growth rate for both IP and OP conditions. Besides, a slightly higher crack growth rate was observed for the IP-test compared to the OP-test as is illustrated in Figure 6.4. The crack propagation character and the parameters influencing the crack propagation for each condition are summarised in Table 6.4 and can be used to rationalise the above observations.

Table 6.4: Summary of crack propagation mode and parameters controlling crack propagation for all the investigated conditions.

	IP-TMF	**OP-TMF**
5 min dwell	Transgranular propagation-Oxidation damage	Transgranular propagation-Oxidation damage
360 min dwell	Intergranular propagation-Grain boundary character	Transgranular propagation-Oxidation assisted recrystallisation

6.5.2.1 In-phase thermal-mechanical and grain boundary character

In the case of the IP tests, the increase of dwell time led to a change in crack propagation mode; a transition from transgranular to intergranular crack propagation was observed. Thus, the higher crack growth rate is attributed to the different crack propagation character.

The transition from transgranular to intergranular crack propagation for the IP-tests can be rationalised as follows. For short dwell times (5 minutes), diffusion phenomena such as oxidation and cavity formation at grain boundaries are not sufficient to impact the crack growth rate. However, the introduction of longer dwell

times, *i.e.* 360 minutes results in stress relaxation, oxidation and creep cavitation, consequently enhanced creep damage, particularly at grain boundaries. Thereby, creep damage forming at grain boundaries can interact with the main crack and lead to higher crack growth rates. It is apparent that the grain boundary character of the alloy will determine how catastrophic the increase of dwell time will be to the TMF performance.

One of the main factors influencing the grain boundary character of superalloys is the precipitation of phases such as different types of carbides. As it was shown, cavities were found to form at the MC carbides with γ/γ' interfaces at the grain boundaries. Voids or cracked MC carbides were observed even ahead of the crack tip as illustrated in Figure 6.8. Thereby the grain boundaries become more susceptible to failure and thus the crack growth rate can be increased.

Besides, it was mentioned earlier that MC carbides oxidise faster than the γ/γ' microstructure. In Chapter 4, Cr and Al segregation at the grain boundary interfaces MC/γ and MC/γ' of STAL15-CC were shown. Segregation of these elements, combined with higher diffusion rates along the grain boundaries, compared to those in the grain interior can result in higher oxidation rates at these particular interfaces; relatively fast crack propagation rates are facilitated. In addition, neither boron nor carbon were found to segregate at these interfaces. Their presence, particularly of boron, could potentially decrease grain boundary diffusivity and oxidation damage.

Figure 6.13(a) illustrates a backscattered image of the secondary intergranular crack tip where the intergranular oxidised MC carbide can be seen ahead of the crack tip; EDX elemental maps of the carbide are illustrated in Figure 6.13(b). The chemistry of the MC carbides and subsequently their thermal stability can influence crack propagation; less stable MC carbides will decompose and oxidise faster, leading to

grain boundaries more prone to failure.

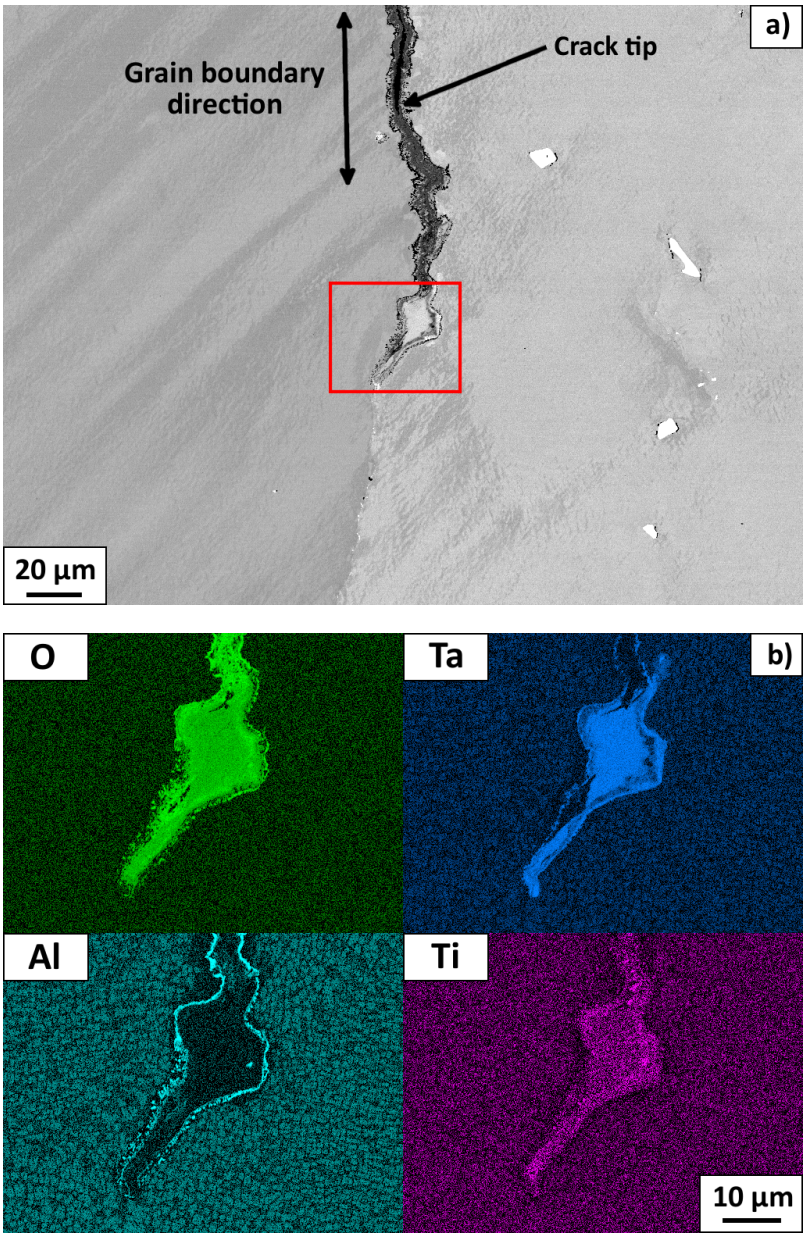


Figure 6.13: a) Backscattered SEM image of the secondary crack tip of the IP–360 minutes dwell time specimen and b) EDX analysis of the intergranular oxidised MC carbide. The red box denotes the analysed by EDX area.

6.5.2.2 Out-of-phase thermal-mechanical and oxidation performance

In the case of the OP-tests, although a transition from transgranular to intergranular crack propagation is not observed, a higher crack growth rate occurs as the dwell time increases to 6 hours. The increase of the crack growth rate in the OP-test is the result of the stress response of the material to the increased dwell time.

In particular, as the holding time under compression at the maximum temperature increases, stress relaxation occurs. As a consequence, greater tensile mean stress is developed. It is apparent that as the holding time increases, the higher the tensile mean stress at the cold end of the TMF cycle. Hence, the higher crack growth rate observed in the OP-test with a 6 hours dwell is ascribed to the higher developed tensile mean stress for the given investigated strain range. Figure 6.6 illustrates the minimum and maximum forces, N, as a function of crack length, respectively. It can be seen that the maximum force increases as dwell increases in the OP tests; similar behaviour is not observed for the IP tests.

However, a microstructural factor that can potentially influence the crack growth rate under OP conditions as dwell time increases is related to the oxidation performance of the alloy. At the OP-test with a 6 hours dwell time, extensive recrystallisation enhanced by oxidation is observed along the crack. A γ' denuded zone is present due to oxidation, where recrystallisation can occur without the retarding effect of γ' precipitates. Although recrystallisation at the γ' denuded zones is observed for all conditions, it is observed relatively far behind the crack tip. In the case of the OP-test with a 6 hours dwell, recrystallisation occurs in the vicinity of the crack tip as illustrated in Figure 6.14; confirmed by EBSD analysis. It is apparent that the oxidation resistance of the alloy and the formation rate of the γ' denuded zone can control the crack growth rate at the OP-TMF case with a dwell period.

Besides, as the maximum temperature increases, the effect of dwell on TMF performance, both IP and OP, will be enhanced and crack propagation rates will increase. In consideration of all of the observed facts, it is concluded that the increase of dwell time exerts a stronger effect under IP-TMF conditions than in OP conditions.

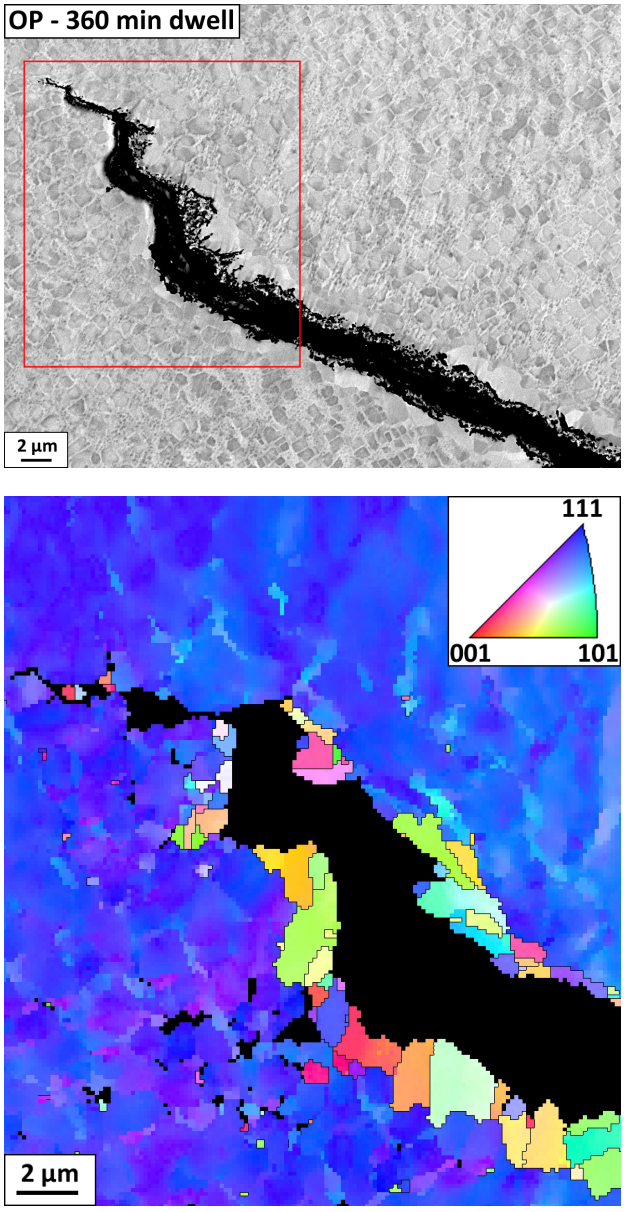


Figure 6.14: Crack tip from the OP with 360 minutes dwell time specimen, alongside corresponding inverse pole map (as denoted by the red box) showing the recrystallisation enhanced by oxidation.

6.6 Summary and Conclusions

In-phase (IP) and out-of-phase (OP) TMF tests were performed with 5 minutes and 6 hours dwell time at the maximum investigated temperature (750°C) on the conventionally cast superalloy IN792. The main conclusions are as follows:

- For a 5 minute dwell time, the crack growth rates for the IP and OP tests were broadly similar. A 6 hours dwell time increases dramatically the crack growth rate; IP test exhibits slightly higher crack growth rate than OP.
- A transition from transgranular to intergranular crack propagation was observed as dwell time increases under IP conditions. The transgranular crack propagation under OP conditions was not altered by the increase of dwell time.
- Residual thermal strains were observed by EBSD strain mapping around MC carbides in fully heat treated microstructure prior to deformation. It was shown that MC carbides can serve as crack initiation sites under IP and OP conditions.
- A substantial fraction of MC carbides were found cracked after both IP-tests; voids were also observed to form at the interface between MC and γ/γ' microstructure. Significant accumulation of plasticity around cracked MC carbides was confirmed by EBSD strain mapping.
- Oxidised MC carbides close to the surface were found to serve as crack initiation sites at the OP-tests.

Chapter 7

Conclusions and Future Work

7.1 Conclusions

The aim of this study was to gain a thorough understanding of the effect of grain boundary elements on superalloys used in industrial gas turbines. For that purpose, two polycrystalline nickel-based superalloys were studied; the new polycrystalline STAL15-CC and the conventionally cast IN792, both suitable for land-based turbines.

In Chapter 4 the role of boron in conferring the grain boundary character in the new polycrystalline superalloy STAL15-CC was discussed. One boron-free and three boron-containing variants were studied using a suite of high resolution characterisation techniques including atom probe tomography, high resolution secondary ion mass spectroscopy and transmission electron microscopy.

The primary effect of boron addition is the suppression of Cr-rich $M_{23}C_6$ carbide and the formation instead of the Cr-rich M_5B_3 boride along the grain boundaries of all the boron-containing alloys. The Ta-rich MC carbides were not affected by the addition of boron.

The NanoSIMS analysis indicated that the boride particles were distributed fairly uniformly along the grain boundaries. The substantial majority of the boron added resides in the form of M_5B_3 borides as confirmed by TEM and APT. Besides, a boron enrichment was found at the γ'/M_5B_3 interfaces, but interfaces of other forms, such as γ/M_5B_3, γ/MC and γ'/MC, show no significant segregation. It was suggested that boron retards carbon segregation towards the grain boundaries due to its higher mobility compared to carbon. The formation of nano-sized $M_{23}C_6$ carbides in the vicinity of grain boundaries supports this suggestion.

Moreover, creep testing at 750 °C and 455 MPa confirmed the beneficial effect of boron on creep performance. The optimum boron content in this alloy is 0.05 at.% (medium boron alloy). Higher additions of boron do not improve the creep performance further as shown in the case of the high boron alloy. A mixed mode of inter- and transgranular failure was observed in the case of the optimal boron content alloy; by contrast intergranular failure is dominant in the other alloys.

In Chapter 5 the improvement in ductility caused by the addition of boron in STAL15-CC was studied. The boron-free alloy and the optimal boron-containing variant were tested in tension at 750 °C and at varying strain rates, using a novel electro-thermal mechanical testing device. *In-situ* tensile tests in the SEM at 750 °C were used to clarify the physical effects by which boron influences the mechanical behaviour.

The secondary effect of boron is the formation of serrated grain boundaries;

planar grain boundaries occur in the boron-free alloy. Serrated grain boundaries occurred for random high-angle grain boundaries, exhibiting an average wavelength of 3.7 μm and amplitude of 1.3 μm; no correlation between the misorientation and the magnitude of serration was observed. The *in-situ* tests indicate the formation of voids at grain boundary segments perpendicular to the tensile axis. Interlinking of voids and formation of a continuous crack path is inhibited by the serrated grain boundaries. HR-EBSD strain mapping analysis revealed uniformly distributed lattice rotation across the grains in the boron-free alloy. Higher lattice rotation were found at the segments of the grain boundary being serrated compared to bulk in the boron-containing alloy.

Cracking of MC carbides was not observed during the *in-situ* tests at 750 °C. Rapid oxidation however of MC carbides at 750 °C after 50 hours was observed. Volume expansion and formation of pores were correlated with the oxidised MC carbides, suggesting that MC can serve as crack initiation sites.

In Chapter 6, the effect of MC carbides on the TMF performance of the nickel-based polycrystalline superalloy IN792 was studied. TMF crack growth measurements with 5 and 360 minutes dwell at the maximum temperature were performed in the temperature range 100-750 °C and for IP and OP-TMF cycles.

MC carbides were found to play an important role on crack initiation performance of IN792. First, HR-EBSD strain mapping revealed residual thermal strains around MC carbides after the full heat-treatment and prior to any deformation. In the case of IP tests, the majority of MC carbides were observed to have cracked. Voids also formed between the MC and the surrounding γ/γ' interfaces, due to the significant accumulation of plastic deformation as confirmed by HR-EBSD strain mapping. By contrast, during the OP tests oxidised MC carbides were found to

serve as crack initiation sites; voids at the MC γ/γ' interfaces or cracked MC carbides were not observed.

Finally, the impact of prolonged dwell times on crack propagation at the highest investigated temperature was studied. It was found that six hours dwell time at maximum temperature increases crack growth rate for both types of TMF; relatively higher rates were observed in the case of IP. A transition from transgranular to intergranular crack propagation was observed for the IP-test as dwell time increases; the trangranular character of the crack in the OP-tests was not affected by the dwell time. MC carbides were found to have cracked or oxidised ahead of the intergranular crack tip resulting in a higher crack growth rate under IP conditions with 360 minutes dwell. In the case of the OP test with dwell, the MC carbides were not found to influence the crack growth rate. The higher crack growth was ascribed to the stress response of the material and to its oxidation performance.

Overall, this study has shown that the grain boundary elements can have a great impact on the performance of polycrystalline nickel-based superalloys for industrial gas turbines. Their additions need to be carefully controlled during the design of new superalloys. It is believed that lower carbon content can further increase their mechanical performance and boron rather than carbon is the main grain boundary strengthener.

7.2 Future Work

The following suggested future work arising from this study is divided into three main areas:

- Evaluation of microstructural stability and oxidation performance over prolonged times of exposure at elevated temperatures.
- High-temperature mechanical testing.
- Grain boundary chemistry alterations.

7.2.1 Microstructural Stability of STAL15-CC

Superalloys need to operate over thousands of hours under extreme conditions without their mechanical integrity being compromised. Thus, the microstructural stability of superalloys over prolonged exposure times at elevated temperatures is of the utmost importance.

The oxidation performance, the precipitation of detrimental topologically close-packed (TCP) phases and the coarsening of γ' particles are some of the most common aspects concerning microstructural stability of superalloys. These factors can be deleterious to the mechanical properties and therefore they are thoroughly investigated.

More specifically, with regard to the oxidation performance, superalloys owe their superior oxidation resistance to the formation of continuous protective layers of Al_2O_3 and/or Cr_2O_3 [4]. Several studies were conducted aiming to rationalise the effect of elements such as Ta, W, Nb and Ti on the oxidation performance of superalloys [162, 163]. However, very little is known about the potential influence of grain boundary elements such as boron.

Boron was reported previously to decrease the susceptibility to oxygen damage, particularly when boron substitutes for carbon in a cast nickel-based superalloy [164, 165]. Other studies suggested that boron is detrimental to the cyclic oxidation by promoting the formation of less passivating NiO scale rather than Al_2O_3 [166]. It was recently shown that boron forms a stable oxide leading to boron depletion from the microstructure [167]. However, the literature around the participation of boron within the oxide scale in superalloys is limited. One possible reason for that could be detection challenges and unambiguous issues with identification of boron within the microstructure of superalloys. However, the improvements in analytical techniques have led to more accurate measurements and therefore some given facts could be re-evaluated in the future.

With all the above in mind an experimental plan that would provide microstructural stability and oxidation investigations is suggested and shown in Table 7.1. In particular, the future plan includes the exposure of fully heat-treated specimens of STAL15-CC isothermally in air at three different temperatures, 800, 850 and 900 °C, and holding times up to 9000 hours.

Table 7.1: Summary of suggested exposure temperatures and times for the microstructural evolution investigations for the three boron variants of STAL15-CC.

Alloys	STAL15-CC (LB, MB and HB)		
Temperature, °C	800, 850 and 900		
Holding time, hours	3000	6000	9000

Although performing such long exposures and conducting a complete characterisation analysis was not feasible within the time frame of the present study, preliminary investigations of the oxide scale in the case of the medium boron specimen exposed at 900 °C for 9000 hours have shown that boron participates in the oxide scale. Figure 7.1 illustrates a backscattered SEM micrograph of the oxide scale

where three different oxide layers can be seen. EDX spot analysis revealed the partitioning of boron at the intermediate layer, as illustrated in Figure 7.2. The chemical analysis has shown that the bottom layer is Al-rich, whereas at the intermediate layer the content of aluminium is relatively lower. Finally, at the outer layer significant enrichment in nickel is observed; the aluminium content is further reduced.

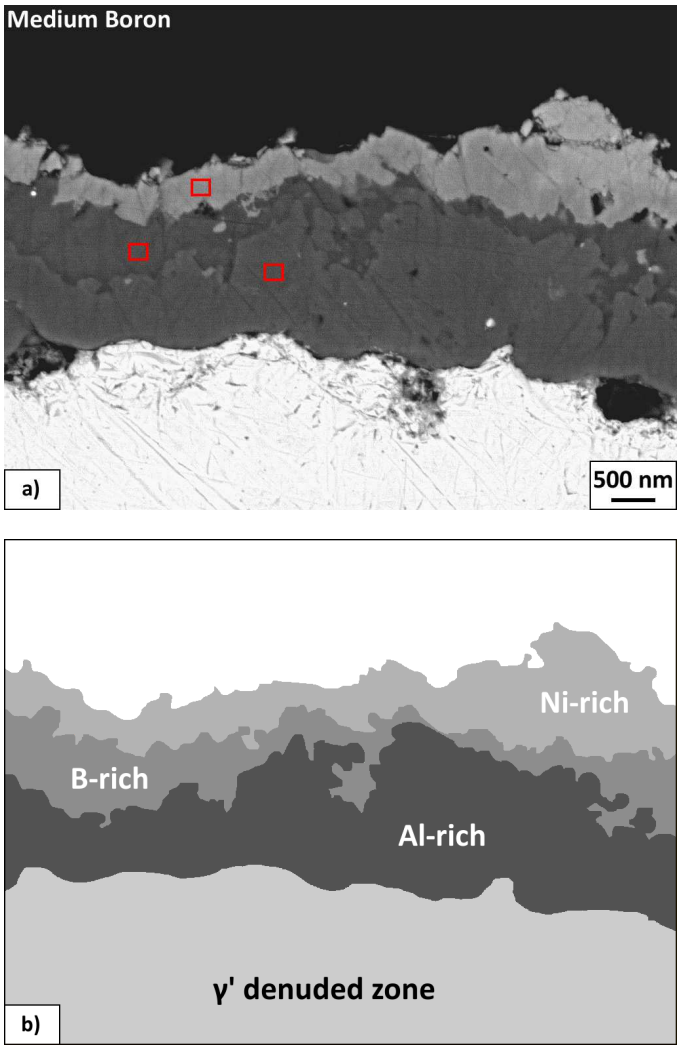


Figure 7.1: Medium boron STAL15-CC alloy exposed isothermally at 900 °C for 9000 hours: a) backscattered SEM micrograph of the oxide scale and b) corresponding schematic representation of the oxide scale. The red boxes denote the areas of point EDX analysis (see data in Figure 7.2)

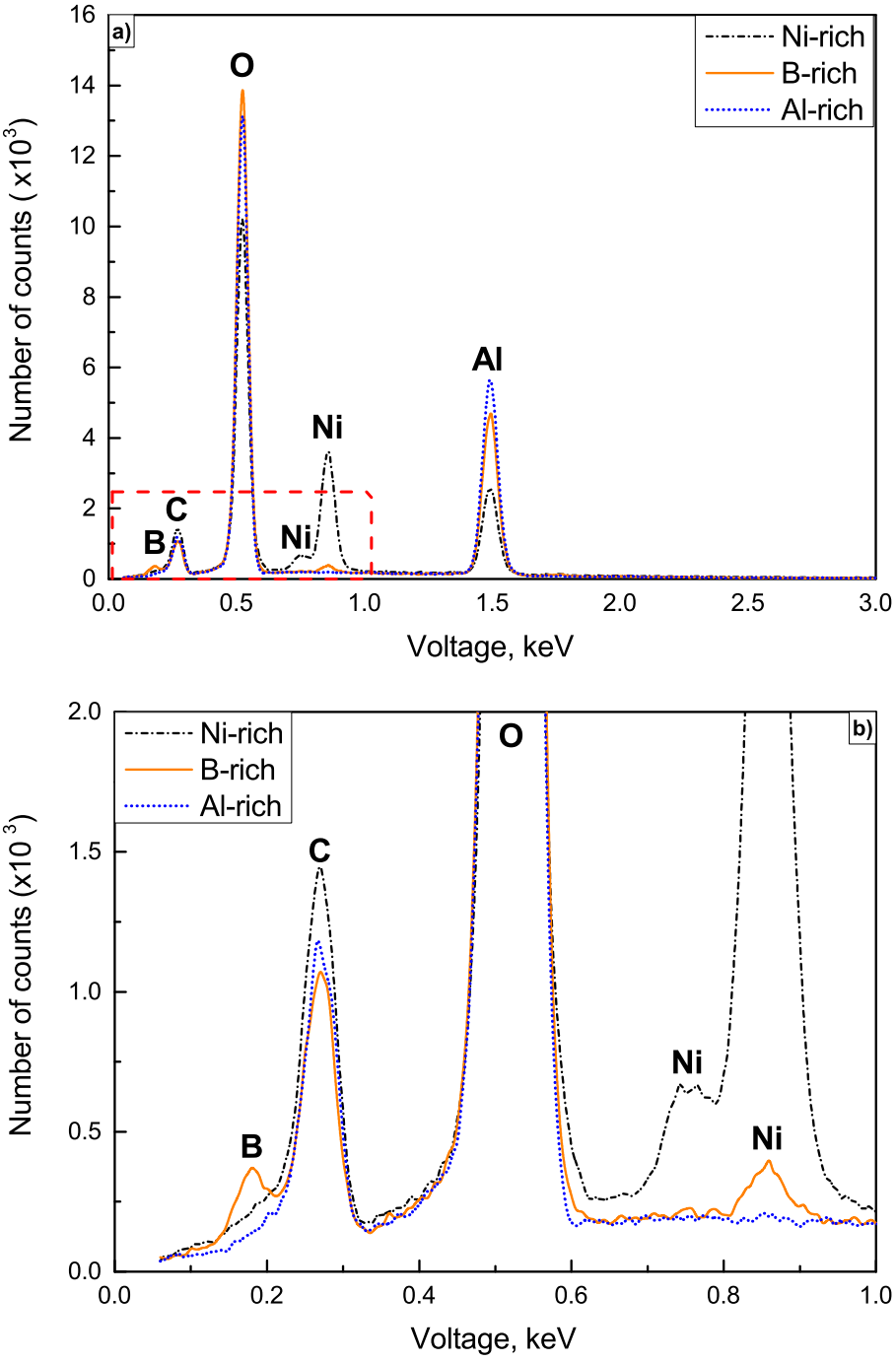


Figure 7.2: a) Point EDX analysis corresponding to the oxide areas denoted by the red boxes in Figure 7.1 and b) detail of the part of the EDX spectrum as denoted by the red dashed box.

Site specific lift-outs were prepared for atom probe tomography from the boron-rich oxide. An APT-3D reconstruction from the boron-rich oxide layer is illustrated in Figure 7.3. It was found that the stoichiometry of the B-rich oxide corresponds to $Al_4B_2O_3$ and segregation of Si was found at the grain boundaries. However, further investigations are required to fully study and interpret these preliminary observations.



Figure 7.3: Atom probe reconstruction from the boron-rich oxide of the medium boron STAL15-CC alloy exposed isothermally at 900 °C for 9000 hours. Grain boundaries are shown in Si.

It is apparent that boron depletion from the microstructure and diffusion towards the oxide scale will adversely affect the mechanical properties of superalloys. In the case of STAL15-CC, boron was found in the form of borides. However, in

many other superalloys boron is found in solid solution. In that case the diffusion of boron towards the oxide scale will be faster; boron depletion will occur sooner. Thus, the content of grain boundary elements required for the design of new superalloys needs to be carefully selected.

7.2.2 High-Temperature Mechanical Testing

Experimental future work consisting of mechanical tests to be performed at elevated temperatures is proposed below for both STAL15-CC and IN792 alloys, respectively.

7.2.2.1 STAL15-CC alloy

Creep tests: The effect of boron on creep performance of STAL15-CC was investigated at 750 °C and 455 MPa . However, its complete evaluation requires further tests at different stress levels and higher temperatures. This way, a complete overview of this beneficial effect on the mechanical properties of superalloys can be achieved. An experimental plan that can address both industrial and academic questions is shown in Table 7.2.

Table 7.2: Proposed testing conditions for the evaluation of the effect of boron on creep performance of STAL15-CC.

Temperature, °C	**Stress, MPa**	
750	455*	385
850	235	185

* Stress level studied.

It was shown that the grain boundary character plays a pivotal role on creep performance of STAL15-CC at 750 °C. A study at higher temperature such as the one proposed above, 850 °C, can reveal further information about the effect of boron

on superalloys. It is possible that the formation of borides along the grain boundaries exhibits a rather different effect on the mechanical properties compared to what has been already observed in this study. In addition, the variation in creep performance was related to the different amounts of boron. At 750 °C, the medium boron version of STAL15-CC performed best in terms of time to creep failure, whereas further increase in the boron content (high boron alloy) resulted in much shorter time to failure. Whether this correlation between creep performance and boron content is consistent at other temperatures needs to be investigated.

Thermal–Mechanical Fatigue Performance: In Chapter 6, it was shown that TMF performance grows in importance for superalloys. No study investigating the effect of boron on TMF properties of superalloys has been previously conducted; therefore scientifically important observations on this matter can be made.

TMF involves creep–fatigue phenomena and it was shown in this study that the amount of boron in STAL15-CC can influence its creep performance. Thus, a relationship between the boron content and TMF performance is expected; for instance on the number of cycles to failure. A correlation similar to what it was observed in the creep performance would be anticipated; particularly under IP conditions where the specimen is in tension at the maximum temperature.

***In-situ* Tensile Tests:** In Chapter 5, *in-situ* tensile tests and HR-EBSD strain mapping were performed at elevated temperatures. The work conducted for this study was focused on grain boundaries only perpendicular to tensile axis, due to their early fracture behaviour. Both planar and serrated grain boundaries were examined and observations about the void initiation sites and crack propagation character were made.

Based on the experience gained from this study, the future work will include investigations of grain boundaries parallel and/or at 45 ° normal to tensile axis under the same conditions and using the same experimental methods. That would provide a direct comparison for instance of the crack initiation sites between grain boundaries with different orientations relative to load axis. A better understanding of the role of the grain boundary particles during mechanical deformation can be achieved.

7.2.2.2 IN792 alloy

Thermal–Mechanical Fatigue and Dwell: In the case of IN792, the effect of dwell time at 750 °C under IP and OP TMF conditions on the crack growth rate was investigated. A substantial increase of the crack growth rate was observed as the dwell time increases from 5 minutes to 6 hours for both TMF conditions. In addition, the increase of dwell time resulted in a transition from transgranular to intergranular crack propagation in the IP tests; the trasgranular crack propagation character of the OP tests was not affected by longer dwell times.

With all the above findings in mind, the performance of the same set of crack growth measurements at higher temperatures is proposed; for instance TMF crack growth measurements at 850 °C. Various deformation mechanisms have been previously observed in the case of IN792 tested under TMF conditions, depending on the investigated temperature [161]. These mechanisms are expected to increase the overall crack growth rates; however it is not clear to what extend.

7.2.3 The Effect of Carbon on Grain Boundaries

Boron was shown to play a beneficial role on the mechanical properties of the recently developed STAL15-CC. However, the subsequent products from the addition

of carbon remain controversial. It was suggested that the mechanical properties of STAL15-CC can be further improved by lowering the carbon content.

In order to provide insights to resolve the issue identified above, it is proposed that alloys should be manufactured with different carbon levels; particularly lower than in the current chemistry specification. At the same time boron content will be kept constant, corresponding to the medium boron STAL15-CC variant (B - 0.05 at.%). Carbon is normally added in superalloys aiming to retard primarily grain boundary sliding by the formation of intergranular carbides. However, nickel-based superalloys used for industrial gas turbines exhibit large grain sizes ($> 700\,\mu$m) and therefore grain boundary sliding is not the dominant deformation mechanism. Thus, an alloy with no carbon additions is also proposed for fundamental investigations.

Grain boundary characterisation and creep tests will be performed in order to evaluate the effect of carbon. It is expected that lower volume fraction of MC carbides will improve the creep performance of STAL15-CC further. Another part of this study will include the effect of the casting process on the shape of MC carbides. It is known that needle-shaped carbides are detrimental for the mechanical properties and the cooling rate during solidification affect their shape; fast cooling rate facilitates the formation of script-type MC carbides. Therefore, a study in which the production process of superalloys controls the mechanical properties should also be conducted.

Bibliography

[1] F.R.N. Nabarro and H.L de Villiers. *The Physics of Creep*. Taylor and Francis, 1995.

[2] G.W. Meetham. In W. Betz, editor, *High temperature alloys for gas turbines and other applications*, volume I. Dordrecht: Reidel, 1986.

[3] R.F. Decker. In J.K. Tien *et al.*, editor, *Superalloys 1980*, pages 1–20. American Society of Metals, 1980.

[4] R.C. Reed. *The Superalloys: Fundamentals and Applications*. Cambridge University Press, 2006.

[5] G.W. Meetham, editor. *The Development of Gas Turbine Materials*. Applied science publishers, London, 1st edition, 1981.

[6] C.T. Sims, N.S. Stoloff, and W.C. Hagel. *Superalloys II: High-Temperature Materials for Aerospace and Industrial Power*. Wiley, 1987.

[7] R.F. Decker and J.W. Freeman. The mechanism of beneficial effects of boron and zirconium on creep-rupture properties of a complex heat-resistant alloy. *Trans. AIME*, 218, 1960.

[8] M.A. Burke, J.J. Greggi, and G.A. Whitlow. The effect of boron and carbon on the microstructural chemistries of two wrought nickel base superalloys. *Scripta metallurgica*, 18:91–94, 1984.

[9] C.K.L. Davies, P.W. Davies, and B. Wilshire. The effect of variations in stacking-fault energy on the creep of nickel-cobalt alloys. *Philosophical Magazine*, 12(118):827–839, 1965.

[10] F.A. Mohamed and T.G. Langdon. The transition from dislocation climb to viscous glide in creep of solid solution alloys. *Acta Metallurgica*, 22(6):779–788, 1974.

[11] S. Ochial, Y. Oya, and T. Suzuki. Alloying behaviour of Ni_3Al, Ni_3Ga, Ni_3Si and Ni_3Ge. *Acta Metallurgica*, 32(2):289–298, 1984.

[12] L. Vegard. Die Röntgenstrahlen im Dienste der Erforschung der Materie. *Zeitschrift für Kristallographie*, 67:239–259, 1928.

[13] R.A. Ricks, A.J. Porter, and R.C. Ecob. The growth of gamma prime precipitates in nickel-base superalloys. *Acta Metallurgica*, 31(1):43–53, 1983.

[14] T.M. Pollock and S. Tin. Nickel-based superalloys for advanced turbine engines: Chemistry, microstructure and properties. *Journal of Propulsion and Power*, 22:361–374, 2006.

[15] R.C. Reed, M. Jackson, and Y. Na. Characterization and modeling of the precipitation of the sigma phase in UDIMET 720 and UDIMET 720Li. *Metallurgical and Materials Transactions A*, 30:521–533, 1999.

[16] A. Volek, R.F. Singer, R. Buergel, J. Grossmann, and Y. Wang. Influence of topologically closed packed phase formation on creep rupture life of direction-

ally solidified nickel-base superalloys. *Metallurgical and Materials Transactions A*, 37(2):405–410.

[17] X.Z. Qin, J.T. Guo, C. Yuan, G.X. Yang, L.Z. Zhou, and H.Q. Ye. μ-phase behavior in a cast Ni-base superalloy. *Journal of Materials Science*, 44(18):4840–4847, 2009.

[18] R.J. Mitchell, C.M.F. Rae, and S. Tin. Grain boundary transformations during isothermal exposure of powder metallurgy nickel base superalloys for turbine disc applications. *Materials Science and Technology*, 21(1):125–132, 2005.

[19] F. Long, Y.S. Yoo, C.Y. Jo, S.M. Seo, Y.S. Song, T. Jin, and Z.Q. Hu. Formation of η and σ phase in three polycrystalline superalloys and their impact on tensile properties. *Materials Science and Engineering: A*, 527(1-2):361–369, 2009.

[20] Q.Z. Chen, N. Jones, and D.M. Knowles. The microstructures of base/modified RR2072 SX superalloys and their effects on creep properties at elevated temperatures. *Acta Materialia*, 50(5):1095–1112, 2002.

[21] J. Yang, Q. Zheng, M. Ji, X. Sun, and Z. Hu. Effects of different C contents on the microstructure, tensile properties and stress-rupture properties of IN792 alloy. *Materials Science and Engineering: A*, 528(3):1534–1539, 2011.

[22] R. Fernandez, J. LeComte, and T. Kattamis. Effect of solidification parameters on the growth geometry of MC carbide in IN-100 dendritic monocrystals. *Metallurgical and Materials Transactions A*, 9:1381–1386, 1978.

[23] J. Chen, J.H. Lee, C.Y. Jo, S.J. Choe, and Y.T. Lee. MC carbide formation in directionally solidified MAR-M247 LC superalloy. *Materials Science and Engineering: A*, 247(1-2):113–125, 1998.

[24] Q.Z. Chen, C.N. Jones, and D.M. Knowles. Effect of alloying chemistry on MC carbide morphology in modified RR2072 and RR2086 SX superalloys. *Scripta Materialia*, 47(10):669–675, 2002.

[25] P. Kotval, J. Venables, and R. Calder. The role of hafnium in modifying the microstructure of cast nickel-base superalloys. *Metallurgical and Materials Transactions B*, 3:457–462, 1972.

[26] J. Yang, Q. Zheng, X. Sun, H. Guan, and Z. Hu. Morphological evolution of MC carbide in K465 superalloy. *Journal of Materials Science*, 41:6476–6478, 2006.

[27] L.Z. He, Q. Zheng, X.F. Sun, H.R. Guan, Z.Q. Hu, A.K. Tieu, C. Lu, and H.T. Zhu. Effect of carbides on the creep properties of a Ni-base superalloy M963. *Materials Science and Engineering: A*, 397(1-2):297–304, 2005.

[28] L.Z. He, Q. Zheng, X.F. Sun, G. Hou, H.R. Guan, and Z.Q. Hu. $M_{23}C_6$ precipitation behavior in a Ni-base superalloy M963. *Journal of Materials Science*, 40:2959–2964, 2005.

[29] J. Yang, Z. Qi, X. Sun, H. Guan, and Z. Hu. Relative stability of carbides and their effects on the properties of K465 superalloy. *Materials Science and Engineering: A*, 429:341–347, 2006.

[30] L.R. Liu, T. Jin, N.R. Zhao, X.F. Sun, H.R. Guan, and Z.Q. Hu. Formation of carbides and their effects on stress rupture of a Ni-base single crystal superalloy. *Materials Science and Engineering: A*, 361(1-2):191–197, 2003.

[31] B.G. Choi, I.S. Kim, D.H. Kim, and C.Y. Jo. Temperature dependence of MC decomposition behavior in Ni-base superalloy GTD 111. *Materials Science and Engineering: A*, 478(1-2):329–335, 2008.

[32] G. Lvov, V. Levit, and M. Kaufman. Mechanism of primary MC carbide decomposition in Ni-base superalloys. *Metallurgical and Materials Transactions A*, 35:1669–1679, 2004.

[33] X.Z. Qin, J.T. Guo, C. Yuan, C.L. Chen, and H.Q. Ye. Effects of long-term thermal exposure on the microstructure and properties of a cast Ni-base superalloy. *Metallurgical and Materials Transactions A*, 38:3014–3022, 2007.

[34] X.Z. Qin, J.T. Guo, C. Yuan, C.L. Chen, J.S. Hou, and H.Q. Ye. Decomposition of primary MC carbide and its effects on the fracture behaviors of a cast Ni-base superalloy. *Materials Science and Engineering: A*, 485(1-2):74–79, 2008.

[35] J. Lecomte-Beckers. Study of microporosity formation in nickel-base superalloys. *Metallurgical and Materials Transactions A*, 19:2341–2348, 1988.

[36] T.S. Piwonka and M.C. Flemings. Pore formation in solidification. *Transactions of The Metallurgical Society of AIME*, 236:1157–1165, 1966.

[37] K.A. Al-Jarba and G.E. Fuchs. Effect of carbon additions on the as-cast microstructure and defect formation of a single crystal Ni-based superalloy. *Materials Science and Engineering: A*, 373(1-2):255–267, 2004.

[38] Q.Z. Chen, Y.H. Kong, C.N. Jones, and D.M. Knowles. Porosity reduction by minor additions in RR2086 superalloy. *Scripta Materialia*, 51(2):155–160, 2004.

[39] J.C. Stinville, K. Gallup, and T.M. Pollock. Transverse creep of nickel-base superalloy bicrystals. *Metallurgical and Materials Transactions A*, 46(6):2516–2529, 2015.

[40] R. Speiser, J.W. Spretnak, and W.J. Taylor. Effective diameter of solute atoms in interstitial solid solutions. *Trans. ASM*, 46:1168, 1954.

[41] P.J. Zhou, J.J. Yu, X.F. Sun, H.R. Guan, and Z.Q. Hu. The role of boron on a conventional nickel-based superalloy. *Materials Science and Engineering: A*, 491:159–163, 2008.

[42] S.M. Seo, I.S. Kim, J.H. Lee, C.Y. Jo, H. Miyahara, and K. Ogi. Eta phase and boride formation in directionally solidified Ni-base superalloy IN792+Hf. *Metallurgical and Materials Transactions A*, 38:883–893, 2007.

[43] O.A. Ojo and H.R. Zhang. Analytical electron microscopy study of boron-rich grain boundary microconstituent in directionally solidified RENE 80 superalloy. *Metallurgical and Materials Transactions A*, 39(12):2799–2803, 2008.

[44] R.T. Holt and W. Wallace. Impurities and trace elements in nickel base superalloys. *International Materials Reviews*, 21(1):1–24, 1976.

[45] L. Xiao, M.C. Chaturvedi, and D. Chen. Effect of boron and carbon on the fracture toughness of IN718 superalloy at room temperature and 650 °C. *Journal of Materials Engineering and Performance*, 14(4):528–538, 2005.

[46] B.C. Yan, J. Zhang, and L.H. Lou. Effect of boron additions on the microstructure and transverse properties of a directionally solidified superalloy. *Materials Science and Engineering: A*, 474(12):39–47, 2008.

[47] D. Tytko, P.-Pa Choi, J. Klöwer, A. Kostka, G. Inden, and D. Raabe. Microstructural evolution of a Ni-based superalloy (617B) at 700 °C studied by electron microscopy and atom probe tomography. *Acta Materialia*, 60(4):1731–1740, 2012.

[48] K.M. Delargy and G.D.W. Smith. Phase composition and phase stability of a high-chromium nickel-based superalloy, IN939. *Metallurgical Transactions A*, 14:1771–1783, 1983.

[49] M. McLean. *Directionally solidified materials for high temperature service.* London: Metals Society, 1983.

[50] P.R. Beeley and R.F. Smart. *Investment Casting.* London: Institute of Materials, 1995.

[51] M.J. Donachie and S.J. Donachie. *Superalloys: A technical guide, 2nd edition.* The Materials Information, 2002.

[52] M.G. Benz. *Impurities in Engineering Materials: Impact, Reliability, and Control.* New York: Marcel Dekker Inc., 1999, 31-47.

[53] M. Zielinksa, K. Kubiak, and J. Sieniawski. Surface modification, microstructure and mechanical properties of investment cast superalloy. *Journal of Achievements in Materials and Manufacturing Engineering*, 35:55–62, 2009.

[54] R.C. Feagin. Dipcoat nucleation. In *Proceedings of the 12th Conference of the European Investment Caster's Federation*, Eindhoven 1967.

[55] L. Liu, T. Huang, Y. Xiong, A. Yang, Z. Zhao, R. Zhang, and J. Li. Grain refinement of superalloy K4169 by addition of refiners: cast structure and refinement mechanisms. *Materials Science and Engineering: A*, 394(1-2):1–8, 2005.

[56] P. Zhijiang, J. Shuqin, Z. Zehai, and L. Yan. Complicated hollow turbine blades and surface grain refinement process. *Research & Development*, 7(2):121–126, 2010.

[57] H.Y. Bor, C. Hsu, and C.N. Wei. Influence of hot isostatic pressing on the fracture transitions in the fine grain MAR-M247 superalloys. *Materials Chemistry and Physics*, 84(2-3):284–290, 2004.

[58] P. Siereveld and J.F. Radavich. In S. Antolovich C. Lund D.N. Duhl, G. Maurer and S. Reichman, editors, *Proceedings of the 6th International Symposium on Superalloy, (TMS, Warrendale, PA, 1988)*, pages 535–544, 1988.

[59] H. Burt, J.P. Dennison, I.C. Elliott, and B. Wilshire. The effect of hot isostatic pressing on the creep and fracture behaviour of the cast superalloy Mar M002. *Materials Science and Engineering*, 53(2):245–250, 1982.

[60] M.H. Bocanegra-Bernal. Hot isostatic pressing (HIP) technology and its applications to metals and ceramics. *Journal of Materials Science*, 39:6399–6420, 2004.

[61] J.S. Waddington and K. Lofthouse. The effect of irradiation on the high temperature fracture of stainless steel. *Journal of Nuclear Materials*, 22:205–213, 1967.

[62] M.E. Kassner and M.T. Pérez-Prado. *Fundamentals of Creep in Metals and Alloys*. Elsevier Science, 2004.

[63] F.C. Monkman and N.J. Grant. *Proc. ASTM*, 56:593, 1956.

[64] F.R. Larson and J. Miller. *Transactions ASME*, 74:765–771, 1952.

[65] L.C. Lim and H.H. Lu. Effect of substructure on intergranular cavitation at high temperature. *Scripta Metallurgica et Materialia*, 31(6):723–728, 1994.

[66] R.T. Chen and J.R. Weertman. Grain boundary cavitation in internally oxidized copper. *Materials Science and Engineering*, 64(1):15–25, 1984.

[67] I-W. Chen and A.S. Argon. Creep cavitation in 304 stainless steel. *Acta Metallurgica*, 29(7):1321–1333, 1981.

[68] H. Hosokawa, H. Iwasaki, T. Mori, M. Mabuchi, T. Tagata, and K. Higashi. Effects of Si on deformation behavior and cavitation of coarse-grained Al4.5Mg alloys exhibiting large elongation. *Acta Materialia*, 47(6):1859–1867, 1999.

[69] R. Raj and M.F. Ashby. Intergranular fracture at elevated temperature. *Acta Metallurgica*, 23(6):653–666, 1975.

[70] N.S. Stoloff and R.M. Pelloux, editors. *Intergranular Cavitation in Creep: Theory and Experiments*, Warrendale, PA, 1980. Proc. Symp. Creep Fatigue-Enviroment Interactions.

[71] B.F. Dyson. Continuous cavity nucleation and creep fracture. *Scripta Metallurgica*, 17(1):31–37, 1983.

[72] M.H. Yoo and H. Trinkaus. Interaction of slip with grain boundary and its role in cavity nucleation. *Acta Metallurgica*, 34(12):2381–2390, 1986.

[73] H. Trinkaus and M.H. Yoo. Nucleation under time-dependent supersaturation. *Philosophical Magazine A*, 55(3):269–289, 1987.

[74] H. Riedel. Cavity nucleation at particles on sliding grain boundaries. A shear crack model for grain boundary sliding in creeping polycrystals. *Acta Metallurgica*, 32(3):313–321, 1984.

[75] T.G. Nieh and W.D. Nix. A comparison of the dimple spacing on intergranular creep fracture surfaces with the slip band spacing for copper. *Scripta Metallurgica*, 14(3):365–368, 1980.

[76] J.N. Greenwood, D.R. Miller, and J.W. Suiter. Intergranular cavitation in stressed metals. *Acta Metallurgica*, 2(2):250–258, 1954.

[77] M.E. Kassner, R.S. Rosen, and G.A. Henshall. Delayed mechanical failure of silver-interlayer diffusion bonds. *Metallurgical Transactions A*, 21A:3085–3100, 1990.

[78] R. Raj. Intergranular fracture in bicrystals. *Acta Metallurgica*, 26(2):341–349, 1978.

[79] D. Hull and D.E. Rimmer. The growth of grain-boundary voids under stress. *Philosophical Magazine*, 4(42):673–687, 1959.

[80] H. Riedel. *Fracture at high temperatures*. Springer-Verlag, Berlin, 1987.

[81] J. Weertman. Hull-Rimmer grain boundary void growth theory - a correction. *Scripta Metallurgica*, 7(10):1129–1130, 1973.

[82] T.-J. Chuang and J.R. Rice. The shape of intergranular creep cracks growing by surface diffusion. *Acta Metallurgica*, 21:1625–1628, 1973.

[83] A. Needleman and J.R. Rice. Plastic creep flow effects in the diffusive cavitation of grain boundaries. *Acta Metallurgica*, 28:1315–1332, 1980.

[84] A.C.F. Cocks and M.F. Ashby. On creep fracture by void growth. *Progress in Materials Science*, 27(34):189–244, 1982.

[85] W.D. Nix. Mechanisms and controlling factors in creep fracture. *Materials Science and Engineering: A*, 103:103–110, 1988.

[86] A. Sato, J.J. Moverare, M. Hasselqvist, and R.C. Reed. On the mechanical behavior of a new single-crystal superalloy for industrial gas turbine applications. *Metallurgical and Materials Transactions A*, 43(7):2302–2315, 2012.

[87] S. Lozano-Perez, M. Schröder, T. Yamada, T. Terachi, C.A. English, and C.R.M. Grovenor. Using NanoSIMS to map trace elements in stainless steels from nuclear reactors. *Applied Surface Science*, 255(4):1541–1543, 2008.

[88] S.S. Yardley, K.L. Moore, N. Ni, J.F. Wei, S. Lyon, M. Preuss, S. Lozano-Perez, and C.R.M. Grovenor. An investigation of the oxidation behaviour of zirconium alloys using isotopic tracers and high resolution SIMS. *Journal of Nuclear Materials*, 443(1-3):436–443, 2013.

[89] K. Thompson, D. Lawrence, D.J. Larson, J.D. Olson, T.F. Kelly, and B. Gorman. In situ site-specific specimen preparation for atom probe tomography. *Ultramicroscopy*, 107:131–139, 2007.

[90] G.B. Viswanathan, P.M. Sarosi, M.F. Henry, D.D. Whitis, W.W. Milligan, and M.J. Mills. Investigation of creep deformation mechanisms at intermediate temperatures in René 88 DT. *Acta Materialia*, 53(10):3041–3057, 2005.

[91] S. Sanyal, U.V. Waghmare, T. Hanlon, E.L. Hall, P.R. Subramanian, and M.F.X. Gigliotti. Interfaces in Ni-based superalloys and implications for mechanical behavior and environmental embrittlement: A first-principles study. In E.S. Huron, R.C. Reed, M.C. Hardy, M.J. Mills, R.E. Montero, P.D. Portella, and J. Telesman, editors, *Superalloys 2012*, pages 531–536. John Wiley & Sons, Inc., 2012.

[92] S. Sanyal, U.V. Waghmare, P.R. Subramanian, and M.F.X. Gigliotti. Effect of dopants on grain boundary decohesion of Ni: A first-principles study. *Applied Physics Letters*, 93(22):223113–1–223113–3, 2008.

[93] T.J. Garosshen, T.D. Tillman, and G.P. McCarthy. Effects of B, C, and Zr on the structure and properties of a P/M nickel base superalloy. *Metallurgical Transactions A*, 18:69–77, 1987.

[94] C.L. Briant and R.P. Messmer. An electronic model for the effect of alloying elements on the phosphorus induced grain boundary embrittlement of steel. *Acta Metallurgica*, 30(9):1811–1818, 1982.

[95] R.P. Messmer and C.L. Briant. The role of chemical bonding in grain boundary embrittlement. *Acta Metallurgica*, 30(2):457–467, 1982.

[96] C.L. White, J.H. Schneibel, and R.A. Padgett. High temperature embrittlement of Ni and Ni-Cr alloys by trace elements. *Metallurgical Transactions A*, 14(3):595–610, 1983.

[97] M. McLean and A. Strang. Effects of trace elements on mechanical properties of superalloys. *Metals Technology*, 11:454–464, 1984.

[98] H.C. Chang and J.N. Grant. Mechanism of intercrystalline fracture. *Journal of Metals*, 8:544–551, 1956.

[99] A.K. Jena and M.C. Chaturvedi. The role of alloying elements in the design of nickel-based superalloys. *Journal of Materials Science*, 19(10):3121–3139, 1984.

[100] L. Xiao, D.L. Chen, and M.C. Chaturvedi. Effect of boron on fatigue crack growth behavior in superalloy IN718 at RT and 650 °C. *Materials Science and Engineering: A*, 428:1–11, 2006.

[101] H.U. Hong, I.S. Kim, B.G. Choi, Y.S. Yoo, and C.Y. Jo. On the mechanism of serrated grain boundary formation in Ni-based superalloys with low γ' voulme

fraction. In E.S. Huron, R.C. Reed, M.C. Hardy, M.J. Mills, R.E. Montero, P.D. Portella, and J. Telesman, editors, *Superalloys 2012*, pages 53–61. John Wiley & Sons, Inc., 2012.

[102] T. Alam, P.J. Felfer, M. Chaturvedi, L.T. Stephenson, M.R. Kilburn, and J.M. Cairney. Segregation of B, P, and C in the Ni-based superalloy, Inconel 718. *Metallurgical and Materials Transactions A*, 43(7):2183–2191, 2012.

[103] H.R. Zhang and O.A. Ojo. TEM analysis of Cr-Mo-W-B phase in a DS nickel-based superalloy. *Journal of Materials Science*, 43(17):6024–6028, 2008.

[104] H.R. Zhang, O.A. Ojo, and M.C. Chaturvedi. Nanosize boride particles in heat-treated nickel base superalloys. *Scripta Materialia*, 58(3):167–170, 2008.

[105] D. Lemarchand, E. Cadel, S. Chambreland, and D. Blavette. Investigation of grain-boundary structure-segregation relationship in an N18 nickel-based superalloy. *Philosophical Magazine A*, 82(9):1651–1669, 2002.

[106] E. Cadel, D. Lemarchand, S. Chambreland, and D. Blavette. Atom probe tomography investigation of the microstructure of superalloy N18. *Acta Materialia*, 50(5):957–966, 2002.

[107] W. Chen, M.C. Chaturvedi, N.L. Richards, and G. McMahon. Grain boundary segregation of boron in INCONEL 718. *Metallurgical and Materials Transactions A*, 29(7):1947–1954, 1998.

[108] X. Huang, M.C. Chaturvedi, N.L. Richards, and J. Jackman. The effect of grain boundary segregation of boron in cast alloy 718 on HAZ microfissuring - a SIMS analysis. *Acta Materialia*, 45(8):3095–3107, 1997.

[109] D. Blavette, P. Duval, L. Letellier, and M. Guttmann. Atomic-scale APFIM and TEM investigation of grain boundary microchemistry in Astroloy nickel base superalloy. *Acta Materialia*, 44(12):4995–5005, 1996.

[110] L. Letellier, A. Bostel, and D. Blavette. Direct observation of boron segregation at grain boundaries in Astroloy by 3D atomic tomography. *Scripta Metallurgica et Materialia*, 30(12):1503–1508, 1994.

[111] L. Letellier, S. Chambreland, P. Duval, and D. Blavette. Grain boundary segregation in nickel base superalloy Astroloy: An atom-probe study. *Applied Surface Science*, 67:305–310, 1993.

[112] A. Buchon, A. Menand, and D. Blavette. Phase composition and grain boundary segregation in a nickel base superalloy: a preliminary TEM-APFIM investigation. *Surface Science*, 246(1-3):218–224, 1991.

[113] *Thermo-Calc Ni-Alloys Mobility Database, version 3.1 (MOBNI3), Thermo-Calc Software AB, Stockholm.* 2014.

[114] L.H. Rettberg and T.M. Pollock. Localized recrystallization during creep in nickel-based superalloys GTD444 and René N5. *Acta Materialia*, 73:287–297, 2014.

[115] J.L.W. Carter, M.W. Kuper, M.D. Uchic, and M.J. Mills. Characterization of localized deformation near grain boundaries of superalloy René-104 at elevated temperature. *Materials Science and Engineering: A*, 605:127–136, 2014.

[116] P. Kontis, H.A. Mohd Yusof, S. Pedrazzini, M. Danaie, K.L. Moore, P.A.J. Bagot, M.P. Moody, C.R.M. Grovenor, and R.C. Reed. On the effect of boron on grain boundary character in a new polycrystalline superalloy. *Acta Materialia*, 103:688–699, 2016.

[117] J. Coakley, R.C. Reed, J.L.W. Warwick, K.M. Rahman, and D. Dye. Lattice strain evolution during creep in single-crystal superalloys. *Acta Materialia*, 60(6-7):2729–2738, 2012.

[118] E.M. Francis, B.M.B. Grant, J. Quinta da Fonseca, P.J. Phillips, M.J. Mills, M.R. Daymond, and M. Preuss. High-temperature deformation mechanisms in a polycrystalline nickel-base superalloy studied by neutron diffraction and electron microscopy. *Acta Materialia*, 74:18–29, 2014.

[119] An-C. Yeh, Kang-W. Lu, Chen-M. Kuo, Hui-Y. Bor, and Chao-N. Wei. Effect of serrated grain boundaries on the creep property of Inconel 718 superalloy. *Materials Science and Engineering: A*, 530:525–529, 2011.

[120] H.U. Hong, I.S. Kim, B.G. Choi, M.Y. Kim, and C.Y. Jo. The effect of grain boundary serration on creep resistance in a wrought nickel-based superalloy. *Materials Science and Engineering: A*, 517(1-2):125–131, 2009.

[121] A. Wisniewski and J. Beddoes. Influence of grain-boundary morphology on creep of a wrought Ni-base superalloy. *Materials Science and Engineering: A*, 510-511:266–272, 2009.

[122] H.L. Danflou, M. Marty, and A. Walder. Formation of serrated grain boundaries and their effect on the mechanical properties in a P/M nickel base superalloy. *TMS Superalloys*, pages 63–72, 1992.

[123] J.M. Larson and S. Floreen. Metallurgical factors affecting the crack growth resistance of a superalloy. *Metallurgical Transactions A*, 8(1):51–55, 1977.

[124] A.K. Koul and G.H. Gessinger. On the mechanism of serrated grain boundary formation in Ni-based superalloys. *Acta Metallurgica*, 31(7):1061–1069, 1983.

[125] M.F. Henry, Y.S. Yoo, D.Y. Yoon, and J. Choi. The dendritic growth of precipitates and grain. *Metallurgical Transactions A*, 24(8):1733–1743, 1993.

[126] R.J. Mitchell, H.Y. Li, and Z.W. Huang. On the formation of serrated grain boundaries and fan type structures in an advanced polycrystalline nickel-base superalloy. *Journal of Materials Processing Technology*, 209(2):1011–1017, 2009.

[127] C.L. Qiu and P. Andrews. On the formation of irregular-shaped gamma prime and serrated grain boundaries in a nickel-based superalloy during continuous cooling. *Materials Characterization*, 76:28–34, 2013.

[128] H.L. Danflou, M. Macia, T.H. Sanders, and T. Khan. Mechanisms of formation of serrated grain boundaries in nickel base superalloys. In R.D. Kissinger, D.J. Deye, D.L. Anton, D. Cetel, M.V. Nathal, T.M. Pollock, and D.A. Woodford, editors, *Superalloys 1996*, pages 119–127. The Minerals, Metals and Materials Society, 1996.

[129] L. Jiang, R. Hu, H. Kou, J. Li, G. Bai, and H. Fu. The effect of $M_{23}C_6$ carbides on the formation of grain boundary serrations in a wrought Ni-based superalloy. *Materials Science and Engineering: A*, 536:37–44, 2012.

[130] Y.S. Lim, D.J. Kim, S.S. Hwang, H.P. Kim, and S.W. Kim. $M_{23}C_6$ precipitation behavior and grain boundary serration in Ni-based Alloy 690. *Materials Characterization*, 96:28–39, 2014.

[131] D. McLean. *Grain boundaries in metals*. Oxford University Press, London, 1957.

[132] F.H. Latief, H.U. Hong, T. Blanc, I.S. Kim, B.G. Choi, C.Y. Jo, and J.H. Lee. Influence of chromium content on microstructure and grain boundary

serration formation in a ternary Ni-xCr-0.1C model alloy. *Materials Chemistry and Physics*, 148(3):1194–1201, 2014.

[133] A.J. Wilkinson, G. Meaden, and D.J. Dingley. High-resolution elastic strain measurement from electron backscatter diffraction patterns: New levels of sensitivity. *Ultramicroscopy*, 106(4-5):307–313, 2006.

[134] J.F. Nye. Some geometrical relations in dislocated crystals. *Acta Metallurgica*, 1(2):153–162, 1953.

[135] P.D. Littlewood, T.B. Britton, and A.J. Wilkinson. Geometrically necessary dislocation density distributions in Ti6Al4V deformed in tension. *Acta Materialia*, 59(16):6489–6500, 2011.

[136] J. Jiang, T.B. Britton, and A.J. Wilkinson. Evolution of dislocation density distributions in copper during tensile deformation. *Acta Materialia*, 61(19):7227–7239, 2013.

[137] J. Jiang, T.B. Britton, and A.J. Wilkinson. Mapping type III intragranular residual stress distributions in deformed copper polycrystals. *Acta Materialia*, 61(15):5895–5904, 2013.

[138] G. Miyamoto, A. Shibata, T. Maki, and T. Furuhara. Precise measurement of strain accommodation in austenite matrix surrounding martensite in ferrous alloys by electron backscatter diffraction analysis. *Acta Materialia*, 57(4):1120–1131, 2009.

[139] P.S. Karamched and A.J. Wilkinson. High resolution electron back-scatter diffraction analysis of thermally and mechanically induced strains near carbide inclusions in a superalloy. *Acta Materialia*, 59(1):263–272, 2011.

[140] T. Zhang, D.M. Collins, F.P.E. Dunne, and B.A. Shollock. Crystal plasticity and high-resolution electron backscatter diffraction analysis of full-field polycrystal Ni superalloy strains and rotations under thermal loading. *Acta Materialia*, 80:25–38, 2014.

[141] M. Winning, G. Gottstein, and L.S. Shvindlerman. Migration of grain boundaries under the influence of an external shear stress. *Materials Science and Engineering: A*, 317(1-2):17–20, 2001.

[142] J.G. Yoon, H.W. Jeong, Y.S. Yoo, and H.U. Hong. Influence of initial microstructure on creep deformation behaviors and fracture characteristics of Haynes 230 superalloy at 900 °C. *Materials Characterization*, 101:49–57, 2015.

[143] J. Wang, L. Zhou, L. Sheng, and J. Guo. The microstructure evolution and its effect on the mechanical properties of a hot-corrosion resistant Ni-based superalloy during long-term thermal exposure. *Materials & Design*, 39:55–62, 2012.

[144] J. Litz, A. Rahmel, and M. Schorr. Selective carbide oxidation and internal nitridation of the Ni-base superalloys IN738LC and IN939 in air. *Oxidation of Metals*, 30(1-2):95–105, 1988.

[145] T. Connolley, P.A.S Reed, and M.J. Starink. Short crack initiation and growth at 600 °C in notched specimens of Inconel 718. *Materials Science and Engineering: A*, 340:139–154, 2003.

[146] A. Pineau, D.L. McDowell, E.P. Busso, and S.D. Antolovich. Failure of metals II: Fatigue. *Acta Materialia*, 107:484–507, 2016.

[147] S. Sanyal, U.V. Waghmare, T. Hanlon, and E.L. Hall. Ni/boride interfaces and environmental embrittlement in Ni-based superalloys: A first-principles study. *Materials Science and Engineering: A*, 530:373–377, 2011.

[148] J.J. Moverare, S. Johansson, and R.C. Reed. Deformation and damage mechanisms during thermal-mechanical fatigue of a single-crystal superalloy. *Acta Materialia*, 57:2266–2276, 2009.

[149] J.J. Moverare and D. Gustafsson. Hold-time effect on the thermo-mechanical fatigue crack growth behaviour of Inconel 718. *Materials Science and Engineering: A*, 528:8660–8670, 2011.

[150] H.U. Hong, J.G. Kang, B.G. Choi, I.S. Kim, Y.S. Yoo, and C.Y. Jo. A comparative study on thermomechanical and low cycle fatigue failures of a single crystal nickel-based superalloy. *International Journal of Fatigue*, 33(12):1592–1599, 2011.

[151] M.J. Starink and P.A.S. Reed. Thermal activation of fatigue crack growth: Analysing the mechanisms of fatigue crack propagation in superalloys. *Materials Science and Engineering: A*, 491(1-2):279–289, 2008.

[152] K. Prasad, R. Sarkar, and K. Gopinath. Role of shrinkage pores, carbides on cyclic deformation behaviour of conventionally cast nickel base superalloy CM247LC at 870 °C. *Materials Science and Engineering: A*, 654:381–389, 2016.

[153] M.M. Kirka, K.A. Brindley, R.W. Neu, S.D. Antolovich, S.R. Shinde, and P.W. Gravett. Parameters influencing thermomechanical fatigue of a directionally-solidified Ni-base superalloy. *International Journal of Fatigue*, 81:48–60, 2015.

[154] I.S. Kim, B.G. Choi, J.E. Jung, J. Do, and C.Y. Jo. Effect of microstructural characteristics on the low cycle fatigue behaviors of cast Ni-base superalloys. *Materials Characterization*, 106:375–381, 2015.

[155] S. Cruchley, H.Y. Li, H.E. Evans, P. Bowen, D.J. Child, and M.C. Hardy. The role of oxidation damage in fatigue crack initiation of an advanced Ni-based superalloy. *International Journal of Fatigue*, 81:265–274, 2015.

[156] J.J. Moverare, M. Segersall, A. Sato, S. Johansson, and R.C. Reed. Thermomechanical fatigue of single-crystal superalloys: influence of composition and microstructure. In E.S. Huron, R.C. Reed, M.C. Hardy, M.J. Mills, R.E. Montero, P.D. Portella, and J. Telesman, editors, *Superalloys 2012*, pages 369–377, 2012.

[157] J.J. Moverare, P. Kontis, S. Johansson, and R.C. Reed. Thermomechanical fatigue crack growth in a cast polycrystalline superalloy. *MATEC Web of Conferences*, 14:19004, 2014.

[158] S. Guth, R. Petráš, V. Škorík, T. Kruml, J. Man, K.-Heinz Lang, and J. Polák. Influence of dwell times on the thermomechanical fatigue behavior of a directionally solidified Ni-base superalloy. *International Journal of Fatigue*, 80:426–433, 2015.

[159] Z.W. Huang, Z.G. Wang, S.J. Zhu, F.H. Yuan, and F.G. Wang. Thermomechanical fatigue behavior and life prediction of a cast nickel-based superalloy. *Materials Science and Engineering: A*, 432:308–316, 2006.

[160] F. Liu, S.H. Ai, Y.C. Wang, H. Zhang, and Z.G. Wang. Thermal-mechanical fatigue behavior of a cast K417 nickel-based superalloy. *International Journal of Fatigue*, 24(8):841–846, 2002.

[161] J. Kanesund, J.J. Moverare, and S. Johansson. Deformation and damage mechanisms in IN792 during thermomechanical fatigue. *Materials Science and Engineering: A*, 528:4658–4668, 2011.

[162] L. Zheng, M. Zhang, and J. Dong. Oxidation behavior and mechanism of powder metallurgy Rene95 nickel based superalloy between 800 and 1000 °C. *Applied Surface Science*, 256(24):7510–7515, 2010.

[163] C. Rae. Alloys by Design: modelling next generation superalloys. *Materials Science and Technology*, 25(4):479–487, 2009.

[164] D.A. Woodford and R.H. Bricknell. Grain boundary penetration of oxygen in nickel and the effect of boron additions. *Metallurgical Transactions A*, 12(8):1467–1475, 1981.

[165] D.A. Woodford. Environmental damage of a cast nickel base superalloy. *Metallurgical Transactions A*, 12(2):299–308, 1981.

[166] C.A. Barrett, R.V. Miner, and D.R. Hull. The effects of Cr, Al, Ti, Mo, W, Ta, and Cb on the cyclic oxidation behavior of cast ni-base superalloys at 1100 and 1150 °C. *Oxidation of Metals*, 20(5-6):255–278, 1983.

[167] A. Jalowicka, W. Nowak, D.J. Young, V. Nischwitz, D. Naumenko, and W.J. Quadakkers. Boron depletion in a nickel base superalloy induced by high temperature oxidation. *Oxidation of Metals*, 83(3-4):393–413, 2015.